

AD-A268 458



1

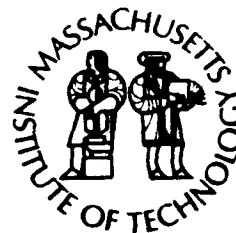
DTIC
ELECTE
AUG 20 1993
S A D

WHOI-92-30

Woods Hole Oceanographic Institution Massachusetts Institute of Technology



Joint Program
in Oceanography/
Applied Ocean Science
and Engineering



DOCTORAL DISSERTATION

Investigation of the Dynamics of Low-Tension Cables

This document has been approved
for public release and sale; its
distribution is unlimited.

by

Christopher Todd Howell

June 1992

93-19405



93 8 19 115

WHOI-92-30

Investigation of the Dynamics of Low-Tension Cables

by

Christopher Todd Howell

Woods Hole Oceanographic Institution
Woods Hole, Massachusetts 02543

and

The Massachusetts Institute of Technology
Cambridge, Massachusetts 02139

June 1992

DOCTORAL DISSERTATION

Funding was provided by the Office of Naval Research
through the Massachusetts Institute of Technology

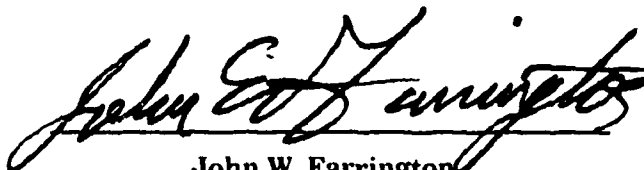
Reproduction in whole or in part is permitted for any purpose of the United States
Government. This thesis should be cited as: Christopher Todd Howell, 1992.
Investigation of the Dynamics of Low-Tension Cables. Ph.D. Thesis. MIT/WHOI,
WHOI-92-30.

Approved for publication; distribution unlimited.

Approved for Distribution:



George V. Frisk, Chairman
Department of Applied Ocean Physics and Engineering



John W. Farrington
Dean of Graduate Studies

Accession For	
NTIS CRA&I	<input checked="checked" type="checkbox"/>
DTIC TAB	<input type="checkbox"/>
Unannounced	<input type="checkbox"/>
Justification	
By	
Distribution /	
Availability Codes	
Dist	Avail and/or Special
A-1	

DTIC QUALITY INSPECTED 1

Investigation of the Dynamics of Low-Tension Cables

by

Christopher Todd Howell

S.M. Ocean Engineering (1990)
Massachusetts Institute of Technology
B.S. Ocean Engineering (1987)
Texas A & M University

Submitted in partial fulfillment
of the requirements for the degree of

Doctor of Philosophy

at the

MASSACHUSETTS INSTITUTE OF TECHNOLOGY

and the

WOODS HOLE OCEANOGRAPHIC INSTITUTION

June 1992

© Massachusetts Institute of Technology 1992. All rights reserved.

Author Christopher Todd Howell
.....
Certified by Micheal S. Triantafyllou Department of Ocean Engineering
.....
Professor Micheal S. Triantafyllou
Thesis Supervisor

Accepted by A. Douglas Carmichael
.....
A. Douglas Carmichael
Chairman, Departmental Committee on Graduate Students
Department of Ocean Engineering

Accepted by Arthur Baggeroer
.....
Arthur Baggeroer
Chairman, Joint Committee for Applied Ocean Science and Engineering

Dedication

To Karen Mary Welsch (Howell)

You have had to make great sacrifices for me.

You have understood that I had to do things my way.

I now plan on devoting the rest of my life to doing the same for you.

Acknowledgements

I express my sincere appreciation to Professor Michael Triantafyllou for his support throughout my graduate studies at MIT. Professor Triantafyllou combines a great intellect with a genuine concern for the people around him, a combination not often found. Regardless of his work load, he always found time to assist me and I feel privileged for having the opportunity to work with him.

I am also grateful to Professors Mark Grosenbaugh and Dick Yue for their insight and input into my research. In addition, Professor Spyros Mavrakos was very helpful, late in the final period. I would also like to thank Jim Burgess for his assistance in the area of numerical simulations.

To the members of the Design Laboratory, in particular Mike Drooker and Seamus Tuohy, I extend my hand in gratitude for their assistance in both my research and my search for employment.

I would also like to thank the real people who keep education moving forward (i.e. the staff members in both the MIT and WHOI education offices). Without their help, I may never have graduated.

The majority of my financial support was provided by the Office of Naval Research through the ONR Graduate Fellowship Program. This support allowed me to pursue my personal interests and was a principal factor in my decision to attend MIT.

I am also thankful for my friends, whom I will not list for fear of inadvertently offending anyone close to me by omitting their name. The friendships I have developed rank amongst my most cherished possessions and, as such, I will strive to retain them in the future, despite the great distances that develop.

Finally, and most importantly, I would like to acknowledge my family. My parents Barbara and Richard, have demonstrated through example the meaning of the words *love*, *commitment*, and *understanding*. And Johnny Hamilton, whose courage in the face of adversity has been a source of great inspiration.

Investigation of the Dynamics of Low-Tension Cables

by

Christopher Todd Howell

Submitted to the Department of Ocean Engineering
on May 27, 1992, in partial fulfillment of the
requirements for the degree of
Doctor of Philosophy

Abstract

Low-tension cable problems are particularly complex as linear solutions are unobtainable in most cases, due to the lack of a meaningful static configuration. By contrast, the dynamics of taut cables are only weakly nonlinear.

First, the three-dimensional nonlinear equations of motion and compatibility relations are formulated for a cable with bending stiffness. Forces in bending are included to provide the necessary physical mechanism for energy transfer across isolated points of zero tension and to ensure a smooth cable configuration.

The mechanisms for low-tension response to excitation are explored by considering the limiting case of a cable with zero initial tension, subject to an impulsive force at one end. The three-dimensional equations show the development of impulsive tension. The intensity of the tension and the velocity components depend exclusively on the initial curvature and are independent of the geometric torsion. In addition, singularities are found to develop at points of curvature discontinuity. Incorporating the cable's bending stiffness removes these singularities by ensuring smooth curvature. However, sustained boundary layers are found to develop, demonstrating the importance of the underlying physical mechanism.

The transition from taut to low-tension behavior is examined through an analysis of the dynamics of a hanging chain, driven by planar harmonic excitation at the top. For moderately large excitation amplitudes, asymptotic results demonstrate the existence of distinct regions of stable two-dimensional and stable three-dimensional response, as a function of frequency, as well as a distinct region in which all steady state solutions are found to be unstable. Numerical solutions of the fully nonlinear equations are in close agreement with the asymptotic results. Numerical results for even larger excitation amplitudes show that large impulse-like tension forces develop which cause the chain to lose tension over a region adjacent to its freely hanging end, and then collapse. The transition from low to high tension regions is clearly demonstrated, with low tension effects being confined to the lower portion of the chain.

Experimental studies were conducted using a chain, 3/8 inches in diameter and 5.8 feet in length, which confirm qualitatively and quantitatively the theoretical and numerical predictions.

Thesis Supervisor: Micheal S. Triantafyllou
Title: Professor of Ocean Engineering

Contents

1	Introduction	13
2	Three-Dimensional Nonlinear Cable Equations	17
2.1	Introduction	17
2.2	Kinematics in 3-D	18
2.3	Three-Dimensional Governing Equations	22
2.3.1	Derivation of governing equations	22
2.3.2	Simplification of governing equations	24
2.4	Applied Forces	29
2.4.1	Cable weight and buoyancy forces	29
2.4.2	Hydrodynamic forces	31
2.5	Compatibility Relations	33
2.6	Final Equations	34
2.7	Three-Dimensional Equations Without Bending Stiffness	35
2.8	Discussion of Equations of Motion	36
3	Numerical Methods	38
3.1	Introduction	38
3.2	Previous Numerical Techniques	38
3.3	Explicit Formulation	41
3.3.1	Equations of Motion	42
3.3.2	Finite-Difference Approximation	42
3.3.3	Explicit Scheme Results	46

3.4	Implicit Formulation with Bending Stiffness	49
3.4.1	Equations of Motion and Boundary Conditions	50
3.4.2	Finite-Difference Approximation	53
3.4.3	Implicit Scheme Results	54
4	Nonlinear Impulsive Motions	56
4.1	Introduction	56
4.2	Formulation of Impulsive Equations of Motion	57
4.3	Solution of Impulsive Dynamics	60
4.3.1	Cable in a straight line	60
4.3.2	Cable in the form of a circle	61
4.3.3	Cable in the form of a helix	62
4.3.4	Cable of reversing curvature	62
4.4	Impulsive Motion of a Cable with Bending Stiffness	65
4.5	Solution of the Cable Equations with Bending Stiffness	68
4.6	Comparison of Analytic and Numerical Results	70
5	Analysis of Response of Hanging Chain	74
5.1	Introduction	74
5.2	Formulation of the Problem	75
5.3	Analytic Analysis	77
5.3.1	Asymptotic Solution	78
5.3.2	Stability Analysis	84
5.3.3	Results	84
5.4	Numerical Solution	87
5.5	Experimental Study	93
5.5.1	Experimental setup	93
5.5.2	Experimental Data	95
5.6	Response to Large Amplitude Excitation	97
6	Analysis of Elastic Cable Behavior	108
6.1	Introduction	108

6.2	Elastic Motions of Shallow Sag Cables	110
6.2.1	Derivation of Linear Equations	110
6.2.2	Analytic Solution of Linear Equations	115
6.2.3	Numerical Results	118
6.3	Extensible Dynamics of Hanging Chain	118
6.3.1	Moderate Excitation Amplitudes	120
6.3.2	Large Amplitude Excitation	121
7	Applications	128
7.1	Introduction	128
7.2	Coupled Low-Tension Tether/Vehicle System	128
7.2.1	Equations of Motion	130
7.2.2	Numerical Results	135
8	Conclusions and Recommendations	141

List of Figures

2.1	Coordinate systems and Euler rotation sequence.	19
2.2	Incremental cable segment.	22
2.3	Superposition of forces to account for end effects.	30
2.4	Description of location vector $\vec{r}(t, p)$	33
3.1	Example of growth of instability in an undamped explicit formulation at times $t=0.0, 2.5$, and 3.0 seconds.	43
3.2	Comparison of calculated error associated with each case study.	48
3.3	Calculated cable shapes for hanging chain problem at times $t=0.0, 4.0$ and 6.5 seconds.	48
3.4	Calculated cable shape from explicit and implicit schemes for anchored cable subjected to a sinusoidal current, at times $t=0.0, 6.0$, and 15.5 seconds. . .	49
3.5	Effects of bending stiffness on anchored cable subjected to a sinusoidal current, at times $t=0.0, 6.0$ and 15.5 seconds.	55
4.1	Cable in a straight line.	60
4.2	Cable in the form of a circle.	61
4.3	Cable of reversing curvature.	63
4.4	Tension (solid line) and angular velocity (dotted line) developing along a cable of reversing curvature (figure 4.3).	70
4.5	Analytically and numerically predicted tension along a cable lying in a circle (figure 4.2) immediately after the application of impulsive loading.	71
4.6	Analytically and numerically predicted normal velocity along a cable lying in a circle (figure 4.2) immediately after the application of impulsive loading.	71

4.7	Analytically and numerically predicted tangential velocity along a cable lying in a circle (figure 4.2) immediately after the application of impulsive loading.	72
4.8	Transverse velocity along cable having initial configuration shown in figure 4.3. at three time intervals.	73
5.1	Cable configuration and coordinate system.	76
5.2	Effect of linear damping on eigenvalues near a saddle-node bifurcation. . .	85
5.3	Stability curves: In-plane velocity at lower end versus detuning for excitation amplitude $Y_0 = 0.0087L$, near the second natural frequency.	86
5.4	Stability curves: Out-of-plane velocity at lower end versus detuning for excitation amplitude $Y_0 = 0.0087L$, near the second natural frequency. . . .	86
5.5	Hamiltonian-Hopf bifurcation: Variation of eigenvalues along 3-D branch. .	87
5.6	Bifurcation diagram: Excitation amplitude versus frequency region in which all stationary solutions are predicted to be unstable.	88
5.7	Numerical results (circles) compared with perturbation results (lines): In-plane velocity at lower end for excitation amplitude $Y_0 = 0.0087L$	89
5.8	Numerical results: Time series record for in-plane and out-of-plane velocities at free end, with excitation amplitude $Y_0 = 0.0087L$ and detuning $\sigma = -0.06$	90
5.9	Power spectrum of in-plane velocity shown in 5.8.	90
5.10	Poincare plot of in-plane velocity shown in 5.8.	91
5.11	Numerical results: Time series record for in-plane and out-of-plane velocities at free end, with excitation amplitude $Y_0 = 0.0087L$ and detuning $\sigma = -0.05$	91
5.12	Power spectrum of in-plane velocity shown in 5.11.	92
5.13	Poincare plot of in-plane velocity shown in 5.11.	92
5.14	Experimental setup.	94
5.15	Experimental results (circles) compared with perturbation results (lines): In-plane velocity at lower end for excitation amplitude $Y_0 = 0.0087L$	95
5.16	Experimental results: Time series record for in-plane and out-of-plane velocities at free end, with excitation amplitude $Y_0 = 0.0087L$ and detuning $\sigma = -0.028$	96

5.17	Experimental results: Time series record for in-plane and out-of-plane velocities at free end, with excitation amplitude $Y_0 = 0.0087L$ and detuning $\sigma = -0.047$	96
5.18	Power spectrum of in-plane velocity shown in 5.16.	97
5.19	Power spectrum of in-plane velocity shown in 5.17.	98
5.20	Numerical results: Chain configuration at several times prior to the collapse of the lower region. Segment in box enlarged on the right.	100
5.21	Numerical results: Predicted chain configuration as free-end intersects the chain.	101
5.22	Comparison of simulation results for two values of EI^*	102
5.23	Numerical results: Total tension at four locations along the chain, for case under study.	103
5.24	Numerical results: Tangential velocity at four locations along the chain, for case under study.	103
5.25	Numerical results: Normal velocity at four locations along the chain, for case under study.	104
5.26	Numerical results: Angle (radians) at four locations along the chain, for case under study.	104
5.27	Numerical results: Normal velocity along chain at four different times, for case under study.	105
5.28	Numerical results: Dynamic tension along chain at four different times, for case under study.	105
5.29	Comparison of experimental and numerical results for collapsing chain: lower half of chain.	106
5.30	Comparison of experimental and numerical results for collapsing chain: lower one-eighth of chain.	107
5.31	Experimental results: Chain configuration at several times prior to the collapse of the lower region.	107
6.1	Cable suspended between two endpoints.	111
6.2	Dependence of fundamental natural frequency on λ	117

6.3	Transverse symmetric mode shape for $\lambda = \pi$; numerical and analytic results shown.	119
6.4	Transverse symmetric mode shape for $\lambda = 2\pi$ (cross-over point); numerical and analytic results shown.	119
6.5	Transverse symmetric mode shape for $\lambda = 3\pi$; numerical and analytic results shown.	120
6.6	Comparison between tension time history at four locations along chain for inextensible chain and elastic chain ($EA^* = 4 \times 10^3$).	122
6.7	Comparison between tension time history at four locations along chain for inextensible chain and elastic chain ($EA^* = 200$).	122
6.8	Comparison between tension time history at four locations along chain for inextensible chain and elastic chain ($EA^* = 4.0 \times 10^4$).	123
6.9	Comparison between tension time history at four locations along chain for inextensible chain and elastic chain, $EA^* = 4.0 \times 10^3$	124
3.10	Mode shape for tension variation due to elastic waves, using $EA^* = 4.0 \times 10^3$.125	
6.11	Contour plot of elastic tension variation in time and space for $EA^* = 4.0 \times 10^3$.125	
6.12	Comparison between tension time history at four locations along chain for inextensible chain and elastic chain, $EA^* = 4.0 \times 10^2$	126
6.13	Mode shape for tension variation due to elastic waves, using $EA^* = 4.0 \times 10^2$.127	
6.14	Contour plot of elastic tension variation in time and space for $EA^* = 4.0 \times 10^2$.127	
7.1	Two component remotely operated underwater vehicle system. (Courtesy of the Woods Hole Oceanographic Institution).	129
7.2	Tether and vehicle coordinate systems.	130
7.3	Applied thruster forces for simulation involving bluff-shaped body.	136
7.4	Numerical results: Displacement of vehicle and tether for applied loads given in figure 7.3.	137
7.5	Numerical results: Tension at three locations along tether for applied loads given in figure 7.3.	138
7.6	Applied thruster forces for simulation involving streamlined body.	139

7.7	Numerical results: Displacement of vehicle and tether for applied loads given in figure 7.6.	139
7.8	Numerical results: Tension at three locations along tether for applied loads given in figure 7.6.	140

Chapter 1

Introduction

Cables are used extensively as structural members for many applications, ranging from suspension bridge hangers to kite string. As such, the study of cable dynamics has a long history, dating back to the study of musical strings by Pythagoras. Nonetheless, as new applications for cable use arise so do questions about their dynamics.

The use of cables is prevalent throughout the offshore industry. Offshore mooring systems, towed acoustic arrays, and remotely operated vehicles are just a few of the offshore systems that strongly depend on cables. In addition, as the exploration and recovery of oil reserves continues to be extended to greater water depths, the mooring and production systems of the required deepwater structures, either for semi-submersibles or tension-leg-platforms (TLP), are almost exclusively comprised of slender tubular members, including: mooring cables; production risers; steel catenary pipelines; and TLP tendons. Due to the length of these members, often times in excess of 3000 feet, the nominal bending stiffness is small and, therefore, their dynamics more closely resemble those of a cable than a beam.

Understanding the dynamics of these cable systems is crucial for operational and safety concerns. However, often the physics involved in these problems are very complicated and difficult to solve. These complications exist for many reasons. First, the structural dynamics problem, in itself, is often nonlinear. Second, complications arise due to hydrodynamic loads, i.e. modelling added mass and nonlinear drag forces, as well as complex fluid problems such as vortex shedding and interference effects. Therefore, the complete nonlinear fluid-structure interaction problem becomes extremely involved.

Cable problems can be separated into a wide range of categories, but, for the purposes of this study we make the primary distinction between highly tensioned (taut) cables and low-tension cables. Herein we focus our attention on the latter class of problems and use the term *low-tension* to refer to problems in which the dynamic tension equals or exceeds the static tension. Another suitable definition is that for low-tension cables the ratio of the end forces to the sum of distributed forces is of order one. This phenomena can be restricted to finite regions, for example near the free end of a cable hanging freely under its own weight, or may span the entire cable length.

Most applications call for taut cables and a substantial amount of research has been conducted in this area (for a review see [25], [68]). Low-tension cables, however, have recently seen increased use largely due to the advent of synthetic cables for which the weight is much less than that of steel cables of equivalent strength, and thus are close to neutrally buoyant in water. Typical applications for low-tension cables include neutrally buoyant marine cables supporting hydrophones and space tethers supporting instrument packages from satellites [33]. In addition, the use of remotely operated vehicle tethers and other cables which involve fiber optic lines for transporting communication signals and power has created systems in which, by necessity, the tension must be kept low.

A different class of problems can be described as low tension applications as well. These include, for example, long towed arrays which, during sharp maneuvers, may lose tension entirely, operating as a low-tension cable for periods of time even though the initial tension may be high.

Low tension problems are particularly complex because, by definition, the dynamic tension is of the same order as the static tension. Therefore, these problems cannot be simplified by linearizing the tension. In addition, the dynamic tension may act to cancel the static tension over a portion of the loading cycle, subsequently giving rise to impulse-like tension forces.

Due to the relatively small restoring force, large amplitude displacements may occur, thus giving preeminence to the effects of geometric nonlinearities. The onset of large displacements also prevents developing solutions which are based on linearizing the equations of motion about some static configuration as a meaningful static configuration does not

exist. The nonlinear dynamics of taut cables, on the other hand, are only weakly nonlinear [20].

Aside from these difficulties, the dynamics of low-tension cables are further complicated by the fact that near isolated points of zero tension, for example near the free end of a towed array, energy travels at very small speed because the speed of propagation is proportional to the square-root of the tension [56]. As such, obtaining solutions in these regions is often very difficult, or even impossible. Dowling [17] and then Triantafyllou and Triantafyllou [74] have shown that it is essential to introduce the bending stiffness of the cable near zero tension points. The resulting solutions were found to contain boundary layers, demonstrating the importance of the underlying physical mechanism.

There are very few references in the literature on the subject of low-tension cables. Leonard [36] considered the dynamics of low-tension cables by formulating the problem for a slack cable. By letting the ratio of the cable weight to the static tension become moderately large, he investigated the nonlinear response caused by the presence of a moderately large dynamic tension. More recently, Triantafyllou and Howell have published several papers in this area dealing with many of the topics addressed herein (see [71], [72], [73]).

In chapter 2 we begin our analysis of low tension cables by deriving the fully nonlinear three-dimensional cable governing equations and compatibility relations. These equations form the mathematical basis of this investigation. The results mentioned previously suggest that bending stiffness plays an important role in low-tension dynamics, especially near isolated points of zero tension. As such, we seek to incorporate the effects of bending stiffness, and torsion, in the equations of motion. Therefore, the equations derived herein can be viewed as a more general formulation than typically found in the past.

As we shall show, the equations of motion for a cable are nonlinear and strongly coupled. Analytic solutions, therefore, are difficult to obtain, except in simplified cases and numerical approximation techniques are often necessary. In chapter 3 previously developed cable simulation algorithms are discussed and two novel numerical techniques, specifically developed with low-tension applications in mind, are detailed.

In chapter 4 we consider cables under zero initial tension, subject to impulsive loads, to gain a better understanding of certain fundamental mechanisms of cable response intrinsic

to low-tension behavior. The equations of cable motion under impulsive loading are derived and solutions are presented for a variety of initial configurations. Both analytic and numerical results are shown.

The transition between high tension and low tension behavior is considered in chapter 5. Toward this end, the dynamics of a chain hanging freely under its own weight, driven harmonically at the top, are studied. The hanging chain exhibits both high tension behavior (near the top boundary) and low-tension behavior (near the free end) and therefore can be seen as a system ideally suited for the analysis of both tension regions, as well as the transition between regions. Asymptotic, numerical, and experimental techniques were implemented to obtain solutions and results are presented and discussed for each of these methods.

In chapters 4 and 5 solutions are found under the assumption that the cable, or chain, is inextensible. In chapter 6, the effects of elasticity are incorporated and the transition between inelastic behavior and elastic behavior is considered.

Applications of the methodology are addressed in chapter 7. In particular, we look at the coupled dynamics of a remotely operated vehicle and tether system. The tether is assumed to be neutrally buoyant and the cable simulation algorithm discussed in chapter 3 is used to model its dynamics. To study the vehicle-tether problem, the cable algorithm was coupled with a vehicle simulation routine and results are presented for several operational maneuvers.

Finally, in chapter 8 we summarize the results and form some conclusions about the dynamics of low-tension cables. Recommendations for future areas of research are also given.

Chapter 2

Three-Dimensional Nonlinear Cable Equations

2.1 Introduction

In this chapter the dynamic equations which form the basis of the mathematical model of the cable are derived. The three-dimensional cable equations of motion were derived in cartesian coordinates by Routh [59] in 1860. Derivations of these equations in so-called natural or lagrangian coordinates, fixed on the cable, have also been done by many authors, including Blik [6]. The equations derived here extend from those presented by other authors who address cable dynamics in that forces in bending are retained. As a result, the equations presented herein constitute a more accurate model for problems in which the cable tension is small, and therefore are applicable for a wider range of tension magnitudes than previous derivations. It should be noted that Love [40], and then Landau and Lifshitz [35], formulated, in cartesian coordinates, fundamentally similar equations by considering the dynamics of thin rods.

Several coordinate systems can be used to study cable dynamics. A lagrangian coordinate system has two primary advantages over a fixed cartesian reference frame. First, it is more straight-forward to describe the hydrodynamic forces in body-fixed coordinates and secondly, results are more easily interpreted. Therefore, we adopt a lagrangian approach herein and, as such, the coordinate system is moving in space and time.

2.2 Kinematics in 3-D

We consider the cable as a single curvilinear line. Let s denote the unstretched lagrangian coordinate along the cable, measured from the origin of the coordinate system to a material point on the cable. The origin is chosen to coincide with a boundary, such as the free end of a towed array, and is denoted as $s = 0$. The other endpoint is denoted as $s = L$, where L is the unstretched cable length.

The cable is considered to be extensible and as such we define $p(t, s)$ as the stretched distance to the same material point s , at a time t . The change in length due to elasticity is given by the strain e . We define the longitudinal strain as

$$e = \lim_{\delta s \rightarrow 0} \frac{\delta p - \delta s}{\delta s} = \frac{dp}{ds} - 1$$

where δs is the unstretched length of an incremental segment and δp is the stretched length. The cable cross-sectional area is also altered due to elongation. Following Goodman and Breslin [19] we make the assumption that the cable has Poisson's ratio $\frac{1}{2}$, i.e. the volume of the cable is preserved after stretching [66]. This value is correct for synthetic materials. Metallic cables have a Poisson ratio closer to $\frac{1}{3}$, so this constitutes an approximation. Also, many wire and synthetic cables have a far more complex structure, and their response involves relative motion between filaments as well as extension. Therefore the chosen value is meant in an average, equivalent sense. As such, if we assume that the cable is of circular cross-section we can express the change in the cable diameter d due to stretching as

$$d = d_s(1 + e)^{\frac{1}{2}} \quad (2.1)$$

Note that here we have used the subscript s to denote a parameter in a stretched condition. This notation will be used throughout this chapter.

The coordinate system is resolved into the tangent, normal, and binormal directions, given by the unit vectors \hat{i} , \hat{n} , and \hat{b} , respectively. The tangential direction is defined as tangent to the cable axis, pointing in the direction of increasing s . The normal direction is perpendicular to \hat{i} and the binormal direction is defined such that the system of vectors

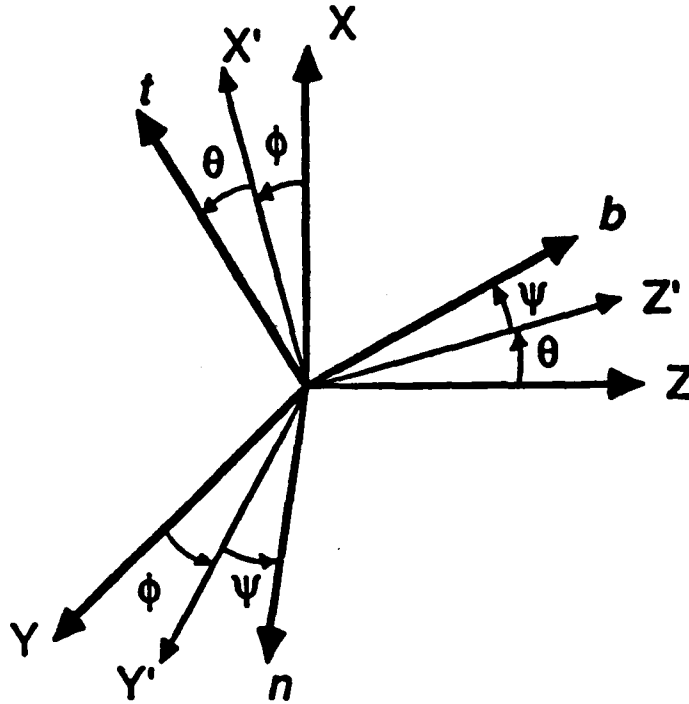


Figure 2.1: Coordinate systems and Euler rotation sequence.

$(\hat{t}, \hat{n}, \hat{b})$ is orthogonal and right-handed.

The transformation between the lagrangian coordinates x , y , and z and the fixed coordinates X , Y , and Z is accomplished through a set of rotations known as Euler angles. The particular choice of Euler angles is arbitrary in the sense that any rotation sequence that provides a unique one-to-one transformation between points in the fixed and moving coordinate systems is valid. For the sake of generality, when possible equations will be expressed in a form which is independent of the Euler rotations chosen.

The following rotation sequence has been chosen for this analysis. First, a rotation about the Z axis by the angle ϕ is performed. Next, a rotation about the resulting Y' axis by the angle θ is made to bring the X' axis in line with the tangent direction. Finally, a rotation about the Z' axis by the angle ψ is conducted to fix the orientation of the normal and binormal directions. This rotation sequence is shown in figure 2.1.

These rotations can be expressed in matrix form as follows:

$$\begin{bmatrix} x \\ y \\ z \end{bmatrix} = \Gamma \begin{bmatrix} X \\ Y \\ Z \end{bmatrix}$$

where

$$\Gamma = \begin{bmatrix} \cos \phi \cos \theta & \sin \phi \cos \theta & -\sin \theta \\ \cos \phi \sin \theta \sin \psi - \sin \phi \cos \psi & \sin \phi \sin \theta \sin \psi + \cos \phi \cos \psi & \cos \theta \sin \psi \\ \cos \phi \sin \theta \cos \psi + \sin \phi \sin \psi & \sin \phi \sin \theta \cos \psi - \cos \phi \sin \psi & \cos \theta \cos \psi \end{bmatrix}$$

It should be noted that it is possible to more formally define the normal direction using the so-called principal directions [21], as done by Blik [6]. The formulation presented here was selected because it is more general when material torsion is involved, and provides greater flexibility in deriving and expressing forces in bending. However, because Frenet's formulas are not applicable to this coordinate system, an additional constraint must be imposed to formally define the orientation of the normal and binormal directions. This constraint will be addressed in the discussion of torsional effects.

Expressions for the time and spatial derivatives are complicated to some degree by the selection of a lagrangian coordinate system. This is due to the fact that in addition to the evolution of the vector quantity of interest, the coordinate system itself also varies in time and space. This can be shown for the arbitrary vector $\vec{G}(t, s)$. Herein we employ the subscript notation (1, 2, 3) to denote the variables in the ($\hat{i}, \hat{n}, \hat{b}$) directions, respectively and express \vec{G} as follows:

$$\vec{G} = G_1 \hat{i} + G_2 \hat{n} + G_3 \hat{b}. \quad (2.2)$$

First consider the time variation of \vec{G} . Expanding the expression for the time derivative gives

$$\frac{D\vec{G}}{Dt} = \frac{\partial \vec{G}}{\partial t} + G_1 \frac{\partial \hat{i}}{\partial t} + G_2 \frac{\partial \hat{n}}{\partial t} + G_3 \frac{\partial \hat{b}}{\partial t}. \quad (2.3)$$

This expression for the so-called substantial or material derivative can be expressed as

$$\frac{D\vec{G}}{Dt} = \frac{\partial\vec{G}}{\partial t} + \vec{\omega} \times \vec{G}, \quad (2.4)$$

where $\vec{\omega}$ is the angular velocity vector. Physically, this vector represents the time rate change of the local coordinate system about the x , y , and z axes. The angular velocity vector is expressed as follows:

$$\vec{\omega} = \omega_1 \hat{i} + \omega_2 \hat{n} + \omega_3 \hat{b} \quad (2.5)$$

where, in terms of the selected Euler angles

$$\begin{aligned} \omega_1 &= \frac{\partial\psi}{\partial t} - \frac{\partial\phi}{\partial t} \sin \theta \\ \omega_2 &= \frac{\partial\theta}{\partial t} \cos \psi + \frac{\partial\phi}{\partial t} \cos \theta \sin \psi \\ \omega_3 &= \frac{\partial\phi}{\partial t} \cos \theta \cos \psi - \frac{\partial\theta}{\partial t} \sin \psi. \end{aligned}$$

The evaluation of changes in space follows along similar lines and is given by

$$\frac{D\vec{G}}{Ds} = \frac{\partial\vec{G}}{\partial s} + \vec{\Omega} \times \vec{G} \quad (2.6)$$

where

$$\vec{\Omega} = \Omega_1 \hat{i} + \Omega_2 \hat{n} + \Omega_3 \hat{b}. \quad (2.7)$$

The vector $\vec{\Omega}$ represents the local curvature of the cable, at the point s , about the local coordinate system and is expressed in component form using the Euler angles as

$$\begin{aligned} \Omega_1 &= \frac{\partial\psi}{\partial s} - \frac{\partial\phi}{\partial s} \sin \theta \\ \Omega_2 &= \frac{\partial\theta}{\partial s} \cos \psi + \frac{\partial\phi}{\partial s} \cos \theta \sin \psi \\ \Omega_3 &= \frac{\partial\phi}{\partial s} \cos \theta \cos \psi - \frac{\partial\theta}{\partial s} \sin \psi. \end{aligned}$$

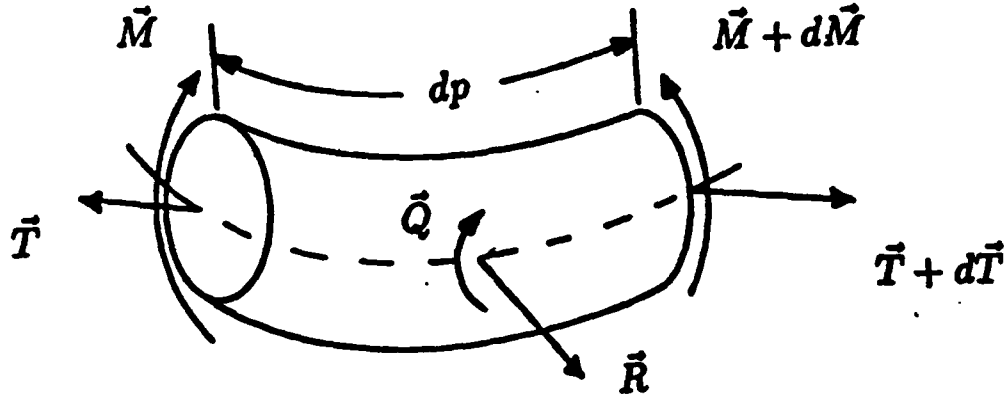


Figure 2.2: Incremental cable segment.

2.3 Three-Dimensional Governing Equations

2.3.1 Derivation of governing equations

We begin the derivation of the governing equations by considering a small cable segment of unstretched length ds and stretched length of dp , as shown in figure 2.2. The velocity and internal force vectors, \vec{V} and \vec{T} , respectively are defined as follows:

$$\vec{V} = v_1 \hat{i} + v_2 \hat{n} + v_3 \hat{b} \quad (2.8)$$

$$\vec{T} = T_1 \hat{i} + T_2 \hat{n} + T_3 \hat{b}.$$

Here T_1 denotes the tension force while T_2 and T_3 represent shear forces. We define \vec{R} as the distributed forces per unit length and m as the unstretched mass per unit length. Conservation of mass dictates that

$$m_s dp = m ds. \quad (2.9)$$

Applying Newton's law to the cable segment, along with the conservation of mass yields

$$m \frac{D\vec{V}}{Dt} = \frac{D\vec{T}}{Ds} + \sum \vec{R}(1 + e). \quad (2.10)$$

We expand the material derivatives in local coordinates to yield

$$m \left(\frac{\partial \vec{V}}{\partial t} + \vec{\omega} \times \vec{V} \right) = \frac{\partial \vec{T}}{\partial s} + \vec{\Omega} \times \vec{T} + \sum \vec{R}(1 + e). \quad (2.11)$$

As mentioned, we seek to incorporate internal forces due to bending and torsional stiffness in the cable. As such we must balance the moments imposed on the incremental cable segment in figure 2.2. Here we define \vec{M} and \vec{Q} as the internal and distributed moment vectors. We define the following unstretched quantities: Young's modulus E ; shear modulus G ; cable density ρ_c ; sectional second moment I ; and polar moment I_p .

The unstretched internal moment vector is expressed as

$$\vec{M} = M_1 \hat{i} + M_2 \hat{n} + M_3 \hat{b} \quad (2.12)$$

where, assuming the cable is a circular, homogeneous cylinder,

$$M_1 = GI_p \Omega_1 \quad (2.13)$$

$$M_2 = EI \Omega_2$$

$$M_3 = EI \Omega_3.$$

It should be noted that in (2.13) Ω_1 represents the material torsion which, in general, is different than the geometric torsion. In addition, the mass moment of inertia per unit length matrix $\rho_c \mathbf{I}$, for a homogeneous cylinder of circular cross-section, is defined as

$$\rho_c \mathbf{I} = \begin{bmatrix} I_p & 0 & 0 \\ 0 & I & 0 \\ 0 & 0 & I \end{bmatrix}$$

Using equation 2.1, the following relations are found between stretched and unstretched

quantities:

$$\begin{aligned}\bar{M} &= \bar{M}_s(1+e)^2 \\ \rho_c \bar{I} &= \rho_c I_s(1+e)^2.\end{aligned}$$

Taking moments about the left-hand side of the cable segment and expressing the results in terms of unstretched quantities yields:

$$\frac{D}{Dt} \left[\frac{\rho_c I \bar{\omega}}{(1+e)} \right] = \frac{D}{Ds} \left[\frac{\bar{M}}{(1+e)^2} \right] + \bar{Q}(1+e) + \bar{d}\bar{r} \times \bar{R}(1+e) + \frac{d\bar{r}}{ds} \times \bar{T}. \quad (2.14)$$

In the limit that $d\bar{r} \rightarrow 0$ we find the following:

$$\begin{aligned}\bar{d}\bar{r} \times \bar{R} &\rightarrow 0 \\ \frac{1}{(1+e)} \frac{d\bar{r}}{ds} &\rightarrow \hat{i}.\end{aligned}$$

It is unlikely that distributed moment forces will arise in the types of problems addressed in this study. As such, this term will not be retained. Applying these simplifications to equation 2.14 provides the set of moment balance equations given below.

$$\frac{D}{Dt} \left[\frac{\rho_c I \bar{\omega}}{(1+e)} \right] = \frac{D}{Ds} \left[\frac{\bar{M}}{(1+e)^2} \right] + \hat{i} \times \bar{T}(1+e) \quad (2.15)$$

The applied forces acting on the cable are located on the right-hand side of equation 2.10. These forces include the internal forces due to tension and shear, as well as external loads. The external loads will be considered in detail in section 2.4.

2.3.2 Simplification of governing equations

Before expressing the governing equations in final form, we attempt to simplify the equations by identifying terms which can be neglected. This will be accomplished by conducting a nondimensional analysis of equations 2.10 and 2.15. Nondimensional terms will be denoted throughout this subsection with a subscript n .

We begin by defining the following nondimensional quantities:

$$\begin{aligned} t_n &= t\sqrt{\frac{g}{L}} \\ \bar{\omega}_n &= \bar{\omega}\sqrt{\frac{L}{g}} \\ s_n &= \frac{s}{L} \\ \bar{\Omega}_n &= \bar{\Omega}L \\ \bar{V}_n &= \frac{\bar{V}}{\sqrt{gL}} \end{aligned}$$

Substitution of these nondimensional quantities into equation 2.10 yields

$$m \frac{D\bar{V}_n}{Dt_n} = \frac{1}{mgL} \frac{D\bar{T}}{Ds_n} + \frac{1}{mg} \sum \bar{R}(1+e) \quad (2.16)$$

Based on this we define the nondimensional force vectors \bar{T}_n and \bar{R}_n as

$$\begin{aligned} \bar{T}_n &= \frac{\bar{T}}{mgL} \\ \bar{R}_n &= \frac{\bar{R}}{mg} \end{aligned}$$

Introducing the previously defined nondimensional quantities into equation 2.15 and neglecting the strain terms associated with the inertial forces yields:

$$(1+e)^2 \frac{\rho_c I g}{L} \frac{D\bar{\omega}_n}{Dt_n} \simeq \frac{EI}{L^2} \left(\frac{D\bar{\Omega}_n}{Ds_n} - \frac{2}{(1+e)} \frac{\partial e}{\partial s_n} \right) + \bar{i} \times \bar{T}_n mgL(1+e)^3 \quad (2.17)$$

Here we have assumed that GI_p is on the order of EI . Rearranging terms, we write the nondimensional equations in bending.

$$\bar{i} \times \bar{T}_n(1+e)^3 \simeq -\beta_1 \frac{D\bar{\Omega}_n}{Ds_n} + \beta_2 \frac{D\bar{\omega}_n}{Dt_n}(1+e)^2 + 2\beta_1 \frac{\partial e}{\partial s_n} \quad (2.18)$$

where

$$\begin{aligned}\beta_1 &= \frac{EI}{mgL^3} \\ \beta_2 &= \frac{\rho_c I}{mL^2}.\end{aligned}$$

In order to determine the relative importance of the variations in strain, we further investigate the last term on the right-hand side. Assuming a linear stress-strain relation is applicable, we write

$$e = \frac{T}{EA}. \quad (2.19)$$

Using this relation we find

$$\frac{EI}{mgL^3} \frac{\partial e}{\partial s_n} = \frac{I}{AL^2} \frac{\partial T_n}{\partial s_n} \simeq \frac{d^2}{L^2} \frac{\partial T_n}{\partial s_n}. \quad (2.20)$$

The diameter to length ratio is typically very small. Therefore, based on (2.20) we will neglect this term.

To compare the relative significance of the bending stiffness term β_1 and the rotational inertia term β_2 we examine their ratio,

$$\frac{\beta_2}{\beta_1} = \frac{g\rho_c L}{E}. \quad (2.21)$$

For steel cables, this ratio is on the order of $10^{-6}L$ meters. For synthetic cables this ratio may be slightly larger. We should still be justified, however, to neglect the rotational inertia terms. As such, rotational inertia terms will not be retained.

Next we consider forces in torsion. Neglecting the rotational inertia term in the moment balance equation about the tangential direction yields

$$GI_T \frac{\partial \Omega_1}{\partial s} = 0 \quad (2.22)$$

Equation 2.22 simply states that the torsional rigidity remains constant throughout the cable span. In the absence of applied end moments, as is typically the case for torque balanced cables, therefore, the effect of torsion is zero. If end moments are present, i.e. a

torque unbalanced cable is considered, the material torsion Ω_1 is constant along the cable span and, therefore, a constant torque is applied over the entire cable length.

Equation 2.22 can be satisfied in one of two ways. First, torsion effects can be neglected either on the basis that $\beta_1 \ll 1$ or because end moments in torsion are not present. The second approach is to calculate Ω_1 from the boundary conditions, and then impose $\Omega_1 = C(t)$ along the span, where $C(t)$ is a time varying constant.

Herein we adopt the first approach and assume that the torsional stiffness is negligible. As a result, a new equation must be chosen to replace equation 2.22. The purpose of the new equation is to fix the orientation of the local coordinate system about the tangential direction. This is an arbitrary selection because the governing equations apply regardless of the orientation of the normal and binormal directions.

For simplicity we specify the orientation of the local coordinate system by setting $\psi = 0$. This simplifies the analysis by removing one variable from the equations.

With this simplification the angular velocity and rotation vectors reduce to the following:

$$\begin{aligned}\omega_1 &= -\frac{\partial \phi}{\partial t} \sin \theta \\ \omega_2 &= \frac{\partial \theta}{\partial t} \\ \omega_3 &= \frac{\partial \phi}{\partial t} \cos \theta\end{aligned}$$

and

$$\begin{aligned}\Omega_1 &= -\frac{\partial \phi}{\partial s} \sin \theta \\ \Omega_2 &= \frac{\partial \theta}{\partial s} \\ \Omega_3 &= \frac{\partial \phi}{\partial s} \cos \theta.\end{aligned}$$

Proceeding further, we examine the significance of the shear forces T_2 and T_3 . Using the simplifications discussed earlier, we find the following nondimensional relations for the shear forces:

$$\begin{aligned}
T_{2n} &= \beta_1(\Omega_{1n}\Omega_{2n} - \frac{\partial\Omega_{3n}}{\partial s_n}) \\
T_{3n} &= -\beta_1(\Omega_{1n}\Omega_{3n} + \frac{\partial\Omega_{2n}}{\partial s_n}).
\end{aligned}$$

Therefore, the shear forces are of order $O(\beta_1)$. This is an important result that provides information as to when shear forces are negligible. In particular, we find that shear stresses are inversely proportional to L^3 , provided the radius of curvature is of order $O(L)$. For moderate to large tension magnitudes, tensile forces prevent the cable from developing substantial variations in curvature. Therefore, if the cable tension T_{1n} is of order $O(1)$ and the cable is very long, it is valid to neglect bending stiffness. However, if the tension is small, the cable can develop substantial curvature and shear forces must be retained.

An alternative means for investigating the significance of bending forces is to consider the induced strains. For simplicity we consider a two-dimensional configuration. Let e_T denote the strain induced by tension, i.e. $T_1 = EAe_T$, and e_c the strain induced by curvature. For a radius of curvature a , the maximum strain due to curvature is given by $e_{cm} = r/a$, where r is the radius of the cable cross-section. If we consider the case where e_{cm} is of the order of e_T , then the binormal bending moment, M_b , is given by $M_b = EI/a \simeq T_1 I/(Ar)$. For cables of circular cross-section, $I = (\pi r^4)/4$. Therefore, we find

$$M \simeq \frac{T_1 r}{4} \quad (2.23)$$

Neglecting rotational inertia effects, the binormal shear force S_b is obtained as

$$S_b = \frac{dM_b}{ds} \simeq \frac{T_1 r}{4l_c} \quad (2.24)$$

where l_c is the characteristic length of change of the bending moment. Therefore, only if l_c is of order r , a situation which is not physically realistic, will the shear forces be of the same order of magnitude as that of T_1 , in this case.

As a result, we can conclude that forces in bending are significant only if the strains they induce are greater than those induced by tension, a situation which can occur in applications

involving low tension.

2.4 Applied Forces

The external forces acting on the cable include the cable weight, buoyancy, and the hydrodynamic forces of drag and added mass. Each of these forces will be addressed separately within this section. Note that all forces discussed in this section are per unit stretched length.

2.4.1 Cable weight and buoyancy forces

Despite the seeming simplicity of static weight and buoyancy forces, a large number of papers have been written on the proper way to express these forces mathematically (see reference list by Sparks [65]). To understand why this has occurred we must first return to basic principles. Archimede's principle states that the net buoyancy force on a body *completely enclosed* in a fluid is equal to the weight of the fluid displaced by the body. The cable segment shown in figure 2.2 is attached to adjoining cable on both ends and is therefore not completely enclosed in fluid.

To account for this condition at the end points, we superimpose forces as shown in figure 2.3. Because segment A is completely enclosed, we can write the buoyancy force F_B as

$$F_B = g\rho_w A, \quad (2.25)$$

where g is the gravitational constant. According to equation 2.1, this expression can be rewritten as

$$F_B(1 + e) = g\rho_w A. \quad (2.26)$$

Subtracting the buoyancy force from the cable self weight we find an expression for w , the submerged cable weight/unit length, given as

$$w_o = (m - \rho_w A)g. \quad (2.27)$$

This force acts in the direction of the gravity vector ($-\hat{i}$) and as such we write the final

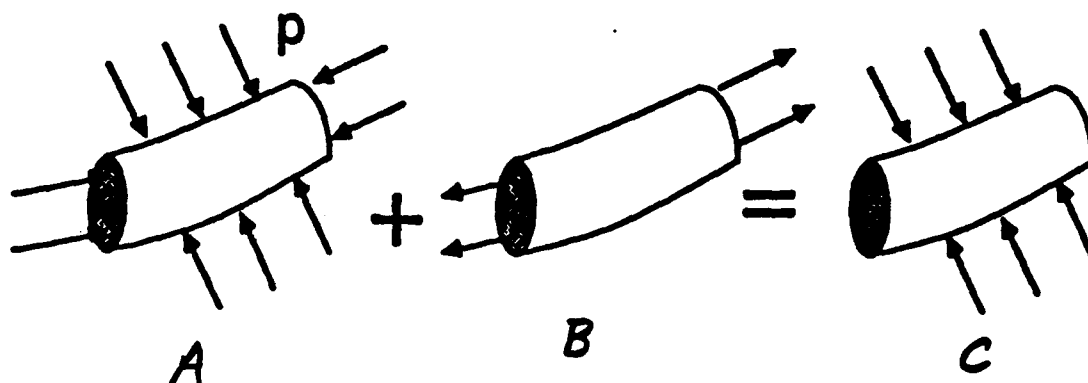


Figure 2.3: Superposition of forces to account for end effects.

expression for the forces due to the submerged cable weight

$$\vec{R}_w(1 + e) = -w_o \hat{i} = w_o(n_1 \hat{i} + n_2 \hat{n} + n_3 \hat{b}) \quad (2.28)$$

where, in terms of the selected Euler angles

$$n_1 = -\cos \phi \cos \theta$$

$$n_2 = \sin \phi$$

$$n_3 = -\cos \phi \sin \theta.$$

Now we must consider the end point forces in segment B. These forces act in the axial direction only and therefore can be lumped together with the internal tension. Following Goodman and Breslin [19], we define the "effective tension", in terms the internal tension and the hydrostatic pressure P , as

$$T_{1e} = T_1 + \frac{PA}{(1 + e)}. \quad (2.29)$$

In this manner, the form of the governing equations remains unchanged in water or air.

Henceforth, to simplify the expressions, T_1 is defined as the effective tension and the subscript e will be dropped.

2.4.2 Hydrodynamic forces

Determining mathematical expressions that accurately model the fluid-structure interaction forces acting on the cable is extremely complex, especially if the effects of vortex shedding are incorporated. Therefore, it is not surprising that a large portion of hydrodynamic research is focussed in this area.

In addition to the hydrodynamic forces that arise from the cable motion itself, we seek to incorporate fluid loads due to current. To this end we define J_j as the current velocity in the j^{th} direction. Transformation between known current magnitudes in a fixed coordinate system to local coordinates is accomplished through the transformation matrix Γ .

Herein we adopt the semi-empirical Morison type approach for modeling hydrodynamic loads [61]. In this manner the fluid loads are decomposed into one component in phase with the fluid velocity (drag) and one component in phase with the fluid acceleration (added mass).

To calculate the hydrodynamic drag force, the fluid velocity field is first decomposed into tangent, normal, and binormal components. Denoting the relative velocities with a subscript r , we can write

$$\begin{aligned}v_{1r} &= v_1 - J_1 \\v_{2r} &= v_2 - J_2 \\v_{3r} &= v_3 - J_3\end{aligned}$$

Using Morison's approximation and denoting C_{d_j} as the drag coefficient in the j^{th} direction, the drag forces are expressed as follows:

$$\vec{R}_d(1 + e) = R_{d1}\hat{i} + R_{d2}\hat{n} + R_{d3}\hat{b} \quad (2.30)$$

where

$$R_{d1} = -\frac{1}{2}\rho_w d \pi C_{d1} v_{1r} |v_{1r}| (1 + e)^{\frac{1}{2}} \quad (2.31)$$

$$R_{d2} = -\frac{1}{2}\rho_w d C_{d2} v_{2r} |v_{2r}^2 + v_{3r}^2|^{\frac{1}{2}} (1 + e)^{\frac{1}{2}} \quad (2.32)$$

$$R_{d3} = -\frac{1}{2}\rho_w d C_{d3} v_{3r} |v_{2r}^2 + v_{3r}^2|^{\frac{1}{2}} (1 + e)^{\frac{1}{2}}. \quad (2.33)$$

Needless to say, accurate values for the drag coefficients are required for accurate solutions. This is not a simple matter with complications arising, for example, from changes in surface roughness and the onset of vortex shedding. As a result, determining drag coefficients has been and continues to be an active area of research. For additional information on drag coefficients consult [61].

Hydrodynamic forces in phase with the fluid acceleration are often called the added mass forces. Added mass forces are one of the most frequently misunderstood concepts in hydrodynamics, especially for investigators who study cable problems. In basic terms, when a body immersed in a fluid is accelerated, the surrounding fluid must be displaced and therefore is also accelerated to some degree. The additional inertia force required to displace the fluid is known as the added mass force [48]. According to this definition, the added mass force can only act in a direction normal to the cable and is independent of viscosity. Lighthill [39] has shown that strip theory is an acceptable means of calculating added mass forces for cables.

We express the added mass force in terms of the relative accelerations of the fluid, normal to the cable, and an added mass coefficient m_a .

$$\vec{R}_a(1 + e) = -m_a \frac{\partial v_{2r}}{\partial t} \hat{n} - m_a \frac{\partial v_{3r}}{\partial t} \hat{b} \quad (2.34)$$

As with the drag coefficients, the evaluation of m_a is difficult. Generally, for cable problems, the following expression is used

$$m_a = \frac{\pi}{4} \rho_w d^2 \quad (2.35)$$

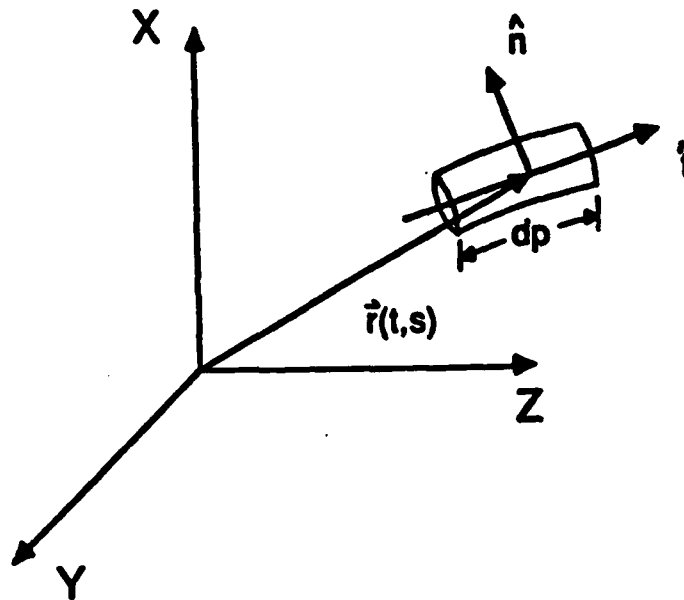


Figure 2.4: Description of location vector $\vec{r}(t, p)$.

2.5 Compatibility Relations

The governing equations as derived are valid for an incremental cable segment. As such, compatibility relations which relate the cable velocities, orientation, and strain are required to ensure compatibility between adjoining cable segments. In the absence of strain, a simple physical interpretation of these relations is that they preserve the cable length.

We define $\vec{r}(t, p)$ as the vector from the origin of a fixed coordinate system to a point on the cable, as shown in figure 2.4. In deriving the compatibility relations we assume that the cable shape is sufficiently smooth. For this to be valid, $\vec{r}(t, p)$ and its derivatives must be continuous functions of p (or s) and t . This assumption was implicitly assumed in the derivation of the governing equations as well. This is an important requirement which may not hold for the particular case of a chain under zero tension. When tension is lost in the chain, a restoring force which prevents the chain from forming discontinuous slope does not exist because chains, unlike cables have no bending stiffness. This topic is addressed further

in chapter 5.

In the absence of discontinuities in the cable shape, we can use the property of continuous functions of two variables [21] and write

$$\frac{D}{Dt} \left[\frac{D\vec{r}}{Ds} \right] = \frac{D}{Ds} \left[\frac{D\vec{r}}{Dt} \right]. \quad (2.36)$$

According to the definitions of the tangent and velocity vectors [21]

$$\begin{aligned} \vec{V} &= \frac{D\vec{r}}{Dt} \\ \hat{i} &= \frac{D\vec{r}}{Ds} = \frac{1}{(1+e)} \frac{D\vec{r}}{Ds} \end{aligned} \quad (2.37)$$

Substitution of 2.37 into 2.36 provides the compatibility relations in vector form

$$\frac{D}{Dt} [(1+e)\hat{i}] = \frac{D\vec{V}}{Ds}. \quad (2.38)$$

This can be expanded to give

$$\frac{\partial e}{\partial t} \hat{i} + (1+e) \vec{\omega} \times \hat{i} = \frac{\partial \vec{V}}{\partial s} + \vec{\Omega} \times \vec{V}. \quad (2.39)$$

2.6 Final Equations

In order to clarify the expressions used in subsequent chapters, we eliminate the subscript notation used previously. Here we redefine the velocities (v_1, v_2, v_3) as (u, v, w) and the internal forces (T_1, T_2, T_3) as (T, S_n, S_b) , where T denotes the effective tension and S_n and S_b are the normal and binormal shear forces, respectively. In addition we assume a linear stress-strain relation is applicable and write

$$e = \frac{T}{EA} \quad (2.40)$$

where T denotes the effective tension, as defined in (2.29).

In terms of the new variables and the expression for the strain, we can express the

equations of motions in their final form.

$$\begin{aligned}
m\left(\frac{\partial u}{\partial t} + w\frac{\partial \theta}{\partial t} - v\frac{\partial \phi}{\partial t} \cos \theta\right) &= \frac{\partial T}{\partial s} + S_b \Omega_2 - S_n \Omega_3 + w_o n_1 + R_{d1} \quad (2.41) \\
m\left(\frac{\partial v}{\partial t} + \frac{\partial \phi}{\partial t}(u \cos \theta + w \sin \theta)\right) + m_a \frac{\partial v_{2r}}{\partial t} &= \frac{\partial S_n}{\partial s} + \Omega_3(T + S_b \tan \theta) + w_o n_2 + R_{d2} \\
m\left(\frac{\partial w}{\partial t} - v\frac{\partial \phi}{\partial t} \sin \theta - u\frac{\partial \theta}{\partial t}\right) + m_a \frac{\partial v_{3r}}{\partial t} &= \frac{\partial S_b}{\partial s} - S_n \Omega_3 \tan \theta - T \Omega_2 + w_o n_3 + R_{d3} \\
EI \frac{\partial \Omega_2}{\partial s} &= EI \Omega_3^2 \tan \theta + S_b \left(1 + \frac{T}{EA}\right)^3 \\
EI \frac{\partial \Omega_3}{\partial s} &= EI \Omega_2 \Omega_3 \tan \theta - S_n \left(1 + \frac{T}{EA}\right)^3 \\
\frac{\partial u}{\partial s} + \Omega_2 w - \Omega_3 v &= \frac{1}{EA} \frac{\partial T}{\partial t} \\
\frac{\partial v}{\partial s} + \Omega_3(u + w \tan \theta) &= \left(1 + \frac{T}{EA}\right) \frac{\partial \phi}{\partial t} \cos \theta \\
\frac{\partial w}{\partial s} - \Omega_3 v \tan \theta - \Omega_2 u &= -\left(1 + \frac{T}{EA}\right) \frac{\partial \theta}{\partial t} \\
\Omega_2 &= \frac{\partial \theta}{\partial s} \\
\Omega_3 &= \frac{\partial \phi}{\partial s} \cos \theta
\end{aligned}$$

2.7 Three-Dimensional Equations Without Bending Stiffness

For completeness we consider the three-dimensional equations of motion in the absence of forces in bending. The assumptions under which these equations are applicable are detailed in section 2.3.2.

Neglecting bending stiffness, (2.41) reduces to six equations in six unknowns, as given by

$$\begin{aligned}
m\left(\frac{\partial u}{\partial t} + w\frac{\partial \theta}{\partial t} - v\frac{\partial \phi}{\partial t} \cos \theta\right) &= \frac{\partial T}{\partial s} + w_o n_1 + R_{d1} \quad (2.42) \\
m\left(\frac{\partial v}{\partial t} + \frac{\partial \phi}{\partial t}(u \cos \theta + w \sin \theta)\right) + m_a \frac{\partial v_{2r}}{\partial t} &= T \frac{\partial \phi}{\partial s} \cos \theta + w_o n_2 + R_{d2} \\
m\left(\frac{\partial w}{\partial t} - v\frac{\partial \phi}{\partial t} \sin \theta - u\frac{\partial \theta}{\partial t}\right) + m_a \frac{\partial v_{3r}}{\partial t} &= -T \frac{\partial \theta}{\partial s} + w_o n_3 + R_{d3}
\end{aligned}$$

$$\begin{aligned}
\frac{\partial u}{\partial s} + w \frac{\partial \theta}{\partial s} - v \frac{\partial \phi}{\partial s} \cos \theta &= \frac{1}{EA} \frac{\partial T}{\partial t} \\
\frac{\partial v}{\partial s} + \frac{\partial \phi}{\partial s} (u \cos \theta + w \sin \theta) &= \left(1 + \frac{T}{EA}\right) \frac{\partial \phi}{\partial t} \cos \theta \\
\frac{\partial w}{\partial s} - v \frac{\partial \phi}{\partial s} \sin \theta - u \frac{\partial \theta}{\partial s} &= -\left(1 + \frac{T}{EA}\right) \frac{\partial \theta}{\partial t}.
\end{aligned}$$

2.8 Discussion of Equations of Motion

Of fundamental significance to the study of low tension cables is that the cable governing equations are singular for zero tension if forces in bending are neglected. Dowling [17] has shown using analytic techniques that when the cable tension is balanced by a fluid loading term, a critical point develops. She found that in order to obtain solutions beyond the critical point, bending stiffness must be incorporated in the boundary layer region near this singularity. In addition, Dowling found that solutions beyond the critical point are influenced by bending stiffness.

The singularity identified by Dowling is the same as that associated with (2.42) because here we have neglected a virtual mass term by considering cables which are transverse to the flow rather than in-line as treated by Dowling. The more general formulation, given by (2.41), is stable for zero tension.

A physical interpretation of the zero tension singularity is most readily understood by considering the mechanisms by which energy is propagated along the cable. For a perfectly flexible cable, transverse disturbances are propagated at a speed proportional to the \sqrt{T} , where T is the instantaneous cable tension [6]. As such, the speed of energy propagation slows considerably in regions of low tension, and energy cannot be transmitted past a critical point of zero tension. As such, energy builds rapidly near the critical point, and the equations become singular. If the point of zero tension coincides with a boundary, i.e. the free end of a hanging chain, energy can be transferred by reflection. For this reason, a zero tension point is permissible at a boundary, provided the boundary is free to reflect energy. Triantafyllou and Triantafyllou [74] have shown that if the free end of a hanging chain is constrained, the governing equations for a perfectly flexible chain are uncolvable.

An alternative energy mechanism which gains importance as the tension approaches zero is bending stiffness. In this later case, energy is transferred by flexural waves at a speed

proportional to \sqrt{EI} . In reality, cables do exhibit a finite degree of flexural rigidity, which can serve as the necessary physical mechanism for energy transfer. By contrast chains have no flexural stiffness. They are, however, able to transfer energy by developing rotational inertia in the individual links.

Chapter 3

Numerical Methods

3.1 Introduction

The cable governing equations derived in chapter 2 are nonlinear and strongly coupled. As a result, analytic solutions are unavailable except in simplified cases. Some analytic results are obtainable using asymptotic techniques, as discussed in chapter 5, however, in order to obtain solutions for more general problems, numerical methods must be employed and a number of algorithms have been developed for this purpose.

In this chapter we first discuss the previously developed numerical techniques in the area of cable dynamics. In particular we address the limitations of these techniques as they apply to the study of low-tension problems. Also addressed in this chapter are two recently developed algorithms which were designed to overcome the drawbacks of existing methods. These two algorithms were used extensively to obtain the numerical results discussed in the subsequent chapters.

3.2 Previous Numerical Techniques

Several papers have been published which survey existing analytic and numerical techniques used to study cable dynamics. Casarella and Parsons [11], and then Choo and Casarella [13], provide comprehensive summaries of the developed methods. However, these papers were written in the early 1970's and recent developments have left these papers somewhat

out-dated. Triantafyllou [68] has recently published a review paper which summarizes many of the advancements that have occurred over the last twenty years.

As mentioned in the introduction, solving the cable governing equations is extremely difficult. These difficulties are principally due to geometric and hydrodynamic nonlinearities. In addition, material nonlinearities may also be present if a linear stress-strain model is not applicable.

To eliminate the nonlinearities, many methods linearize the problem by assuming small deformations from some static configuration. This greatly simplifies the analysis. However, for low-tension problems, large displacements can develop due to the small restoring force, thereby rendering any static configuration meaningless. Also, because the dynamic tension may be equal or greater than the static tension, low-tension problems cannot be simplified by linearizing the tension.

Other assumptions typically made include neglecting inertial forces, bending stiffness, and elasticity. The validity of these assumptions is dependent on the particular analysis in question and the methods therefore are often restricted to a limited class of problems.

In recent years a wide range of numerical techniques have been applied to the study of cable dynamics. The most prevalent methods of approach are finite-difference, finite-element, spectral-method and lumped-parameter models (for separate discussions of these methods see [1],[15],[77],[7], and [29]). A detailed comparison between finite element and lumped parameter methods has been published by Leonard and Nath [37]. The method of characteristics has also been used successfully. In particular, Schram and Reyle [62] used the method to show coupling occurs between transverse and longitudinal disturbances if the shape of the cable is not straight.

In the author's opinion a finite-difference approach is most suitable for the low-tension problem. Lumped-parameter and finite-element models require an excessive amount of computer storage and often obscure the underlying physics of the problem. Other authors have determined that finite-element models are not well suited for inherently nonlinear problems, involving large displacements [16]. Spectral-methods suffer from the limitation that derivative boundary conditions, such as those encountered when incorporating bending stiffness, are often difficult to evaluate.

The finite difference method has been used extensively in the past to model cable problems. Sanders [60] developed a three-dimensional algorithm in which finite-differences are used to discretize the cable and simulations are advanced in time using a Runge-Kutta recurrence scheme [55]. This algorithm suffers from the limitation that inertial forces are neglected. This assumption is not valid for low-tension problems in that inertial forces can be on the same order of magnitude as tensile forces.

In 1983, Ablow and Schechter [1] developed a three-dimensional algorithm which includes inertial forces and discretizes the problem in both space and time using finite-differences. The method uses a second-order accurate implicit approximation scheme, commonly known as the box-method [45], which is centered in space and time. Milinazzo, Wilkie, and Latchman [44] improved on the methodology of Ablow and Schechter by developing a better method for treating the zero tension boundary condition at the free end. Burgess [8] corrected earlier mistakes in these publications by properly accounting for the hydrostatic and added mass forces. In addition, he has incorporated the ability to pay cable out from a ship, as required for cable deployment simulations. However, as with the previous authors, he incorrectly applied the principle of conservation of mass and derived erroneous strain terms in his equations.

An important point to note about these previous formulations is that the algorithms all become unstable if the tension approaches zero anywhere along the interior of the cable, a situation which is likely to occur in low-tension studies. This is a significant drawback of the methods and prevents altogether the study of cables under zero initial tension.

Ablow and Schechter [1] determined that if the tension vanishes anywhere along the cable, the determinant of their stiffness matrix becomes zero. Because this matrix is inverted within their numerical approximation scheme, the method fails. As noted by Dowling [17], the singularity encountered by Ablow and Schechter is not an artifact of their numerical scheme; instead it stems from the omission of flexural stiffness in the dynamic equations. The previously noted finite difference schemes all neglect the effects of bending stiffness and therefore are limited in their application to low-tension problems based on both numerical and physical considerations.

An sidenote to Dowling's work is that her solution is based on the correct form of the

linearized transverse momentum equation, first derived by Paidoussis [52]. In two earlier papers by Paidoussis ([50],[51]) a term was incorrectly omitted in this equation, leading several authors ([49],[30],[31]) to publish erroneous solutions of the towed array problem.

The limitations of existing algorithms created a need for novel approaches to the low-tension problem. Two alternative numerical methods were developed for this purpose. The first method was primarily developed to treat problems under zero tension initially, such as impulsively loaded cables as discussed in chapter 4. Prior to excitation of the cable, zero tension is permissible, therefore, the failure of previous algorithms in this case stems from the numerical formulation. Within the method, which is detailed in the next section, an explicit time integration scheme is used in which the cable tensions are cast as the only unknowns in a matrix problem. Therefore, the onset of zero tension along the cable does not present a problem computationally. This allows a wider class of initial value problems to be studied.

The second method developed incorporates the effects of bending stiffness in an implicit finite difference formulation, similar to that of Ablow and Schechter. An implicit scheme was selected because the characteristics of the governing equations are altered by including bending stiffness [76]. In section 3.4 we show that incorporating bending stiffness eliminates the zero tension singularity. This finding has been shown previously for the two-dimensional case by Howell [22].

3.3 Explicit Formulation

Explicit time-domain integration schemes are generally used in conjunction with finite-element and lumped-parameter methods [12]. However, existing finite-difference algorithms use implicit time integrators. The reason is that implicit schemes can be unconditionally stable while explicit schemes are conditionally stable [37]. In addition, explicit schemes are not well suited for predominantly parabolic equations [45]. This has led some researchers [60] to question the applicability of explicit schemes in general. However, it is possible to formulate the difference equations so as to retain the hyperbolic characteristics of the governing equations. In addition, by choosing the inextensible form of the cable equations, we can eliminate longitudinal waves. This reduces the stiffness of the equations because longi-

tudinal wave speeds are generally much higher than those for transverse waves. Therefore, an explicit solution scheme is feasible, provided it remains stable. Such a scheme could offer significant advantages over implicit schemes because no iterations are required.

3.3.1 Equations of Motion

In this section we restrict our attention to two-dimensional problems only. The two-dimensional inextensible form of the governing equations and compatibility relations is given by

$$\begin{aligned}
 m\left(\frac{\partial u}{\partial t} - \frac{\partial \phi}{\partial t}v\right) &= \frac{\partial T}{\partial s} - w_o \cos \phi - \frac{1}{2}\rho_w D\pi C_{dt}u_r|u_r| & (3.1) \\
 m\left(\frac{\partial v}{\partial t} + \frac{\partial \phi}{\partial t}u\right) + m_a \frac{\partial v_r}{\partial t} &= T \frac{\partial \phi}{\partial s} + w_o \sin \phi - \frac{1}{2}\rho_w DC_{dn}v_r|v_r| \\
 \frac{\partial u}{\partial s} - \frac{\partial \phi}{\partial s}v &= 0 \\
 \frac{\partial v}{\partial s} + \frac{\partial \phi}{\partial s}u &= \frac{\partial \phi}{\partial t}.
 \end{aligned}$$

These equations describe the mathematical formulation of the problem and form the basis of the numerical approximation scheme. With regard to boundary conditions, we consider the cable to be pinned at one end ($s = L$), with the tangential and normal velocities prescribed. The other end ($s = 0$) is considered to be a free boundary and zero tension is imposed at this end. The fourth boundary condition, zero moment at the free end, is automatically satisfied by neglecting bending stiffness.

3.3.2 Finite-Difference Approximation

The basic premise of the explicit formulation is to write all spatial derivatives in terms of the previous time step and to then solve for the new time values directly. The formulation begins by first discretizing the cable into n nodes. The governing equations are then applied directly at each node. First-order and second-order approximations are used for the time and spatial derivatives, respectively. Second-order forward and backward differences are used for spatial derivatives at nodes 1 and n , respectively.

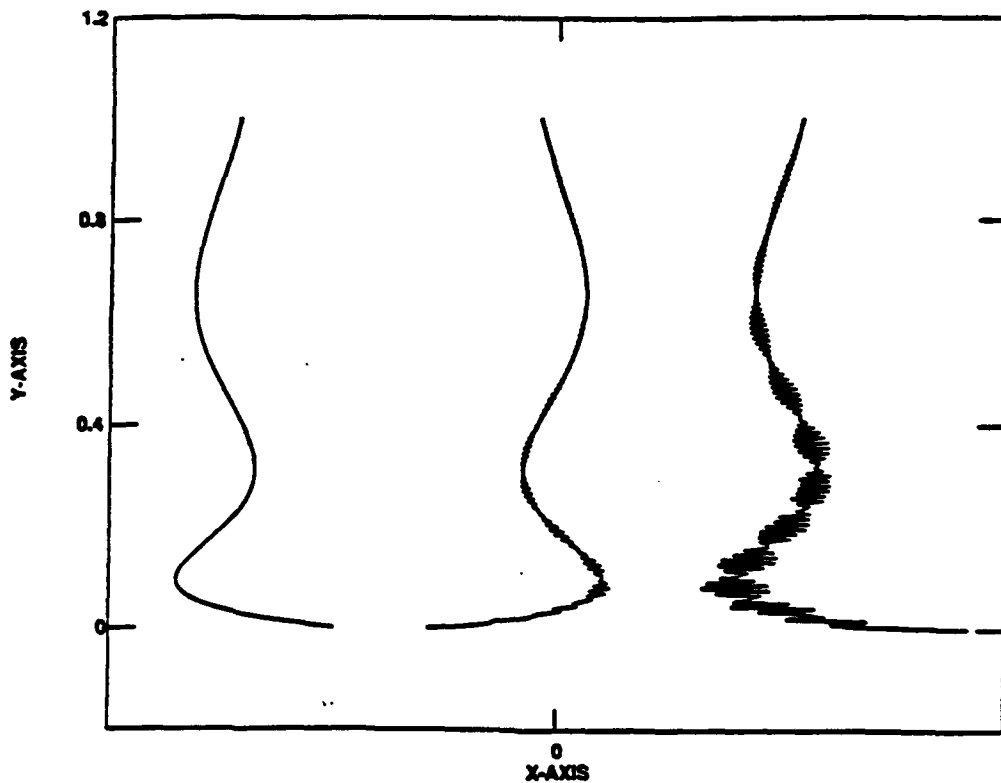


Figure 3.1: Example of growth of instability in an undamped explicit formulation at times $t=0.0$, 2.5 , and 3.0 seconds.

As with any numerical scheme, stability is a major concern. It has been determined that in the formulation described above some degree of *numerical viscosity* is required for stability. This finding is demonstrated in figure 3.1. The problem studied was a hanging chain in air, subject to a sinusoidal displacement at the top. The cable was initially in a Bessel function shape, as given by the third natural mode of the linear system. The instability encountered was due to undamped high frequency parasitic waves generated at the lower boundary. It can be shown that these waves grow exponentially in time [45]. The goal is to construct a numerical scheme which is accurate for the long wavelengths (which are the main interest) while at the same time dissipates the energy at the short wavelengths (which tend to corrupt the solution). Such a method is no less accurate than a nondissipative model, as the latter is already inaccurate for high-spatial wave numbers. For this reason an artificial dissipative term is added to each approximation of the time derivatives and the degree of dissipation is controlled by the leading coefficient α , where

$\alpha \ll 1$. Mathematically, the procedure is represented by the approximation below.

$$\frac{\partial u}{\partial t} \approx \frac{\partial u}{\partial t} - \alpha \frac{\partial^2 u}{\partial x^2} \quad (3.2)$$

This procedure is similar to the Lax-Fredrichs and Lax-Wendroff [45] formulations of the first-order wave equation. Within these two methods, the leading coefficient α is dependent upon the spatial and time stepping increments, Δs and Δt , respectively, and is given by the following:

$$\begin{aligned} \alpha &= \frac{\Delta s^2}{2\Delta t} & \text{Lax - Fredrichs} \\ \alpha &= \frac{\Delta t}{2} & \text{Lax - Wendroff.} \end{aligned}$$

Within the present explicit scheme, the α coefficient is independent of the stepping factors and can be varied along the cable and between the independent variables (ϕ, u, v). This allows the user greater flexibility during the investigation. The basic idea is to choose α of sufficient magnitude to provide stability while being small enough to have a negligible effect on accuracy.

Combining the approximations described above yields the following system of equations:

Node 1 (forward-differences)

$$\phi_1^{i+1} = \bar{\phi}_1^i - \lambda_r [v_3^i - 4v_2^i + 3v_1^i + u_1^i(\phi_3^i - 4\phi_2^i + 3\phi_1^i)] \quad (3.3)$$

$$\begin{aligned} u_1^{i+1} &= \bar{u}_1^i + v_1^i(\phi_1^{i+1} - \bar{\phi}_1^i) + \frac{\lambda_r}{m}(-T_3^i + 4T_2^i - 3T_1^i) - \\ &\quad \frac{w_o \Delta t}{m} \cos(\phi_1^i) - \frac{\Delta t}{m} \frac{1}{2} \rho_w D \pi C d_t u_{r1}^i |u_{r1}^i| \end{aligned} \quad (3.4)$$

$$\begin{aligned} v_1^{i+1} &= \bar{v}_1^i - \frac{m}{m_1} u_1^i(\phi_1^{i+1} - \bar{\phi}_1^i) - \frac{m_o}{m_1} [J_Y^{i+1} \cos(\phi_1^{i+1}) - J_Y^i \cos(\phi_1^i)] + \frac{w_o \Delta t}{m_1} \sin(\phi_1^i) - \\ &\quad \frac{\lambda_r}{m_1} T_1^i(\phi_3^i - 4\phi_2^i + 3\phi_1^i) - \frac{\Delta t}{m_1} \frac{1}{2} \rho_w D C d_n v_{r1}^i |v_{r1}^i| \end{aligned} \quad (3.5)$$

$$T_1^i = 0.0 \quad (3.6)$$

Internal Nodes (central-differences)

$$\phi_j^{i+1} = \bar{\phi}_j^i - \lambda_r [v_{j+1}^i - v_{j-1}^i + u_j^i (\phi_{j+1}^i - \phi_{j-1}^i)] \quad (3.7)$$

$$u_j^{i+1} = \bar{u}_j^i + v_j^i (\phi_j^{i+1} - \bar{\phi}_j^i) + \frac{\lambda_r}{m} (T_{j+1}^i - T_{j-1}^i) - \frac{w_o \Delta t}{m} \cos(\phi_j^i) - \frac{\Delta t}{m} \frac{1}{2} \rho_w D \pi C d_t u_{rj}^i |u_{rj}^i| \quad (3.8)$$

$$v_j^{i+1} = \bar{v}_j^i - \frac{m}{m_1} u_j^i (\phi_j^{i+1} - \bar{\phi}_j^i) - \frac{m_a}{m_1} [J_Y^{i+1} \cos(\phi_j^{i+1}) - J_Y^i \cos(\phi_j^i)] + \frac{w_o \Delta t}{m_1} \sin(\phi_j^i) - \frac{\lambda_r}{m_1} T_j^i (\phi_{j+1}^i - \phi_{j-1}^i) - \frac{\Delta t}{m_1} \frac{1}{2} \rho_w D C d_n v_{rj}^i |v_{rj}^i| \quad (3.9)$$

$$u_{j+1}^{i+1} - u_{j-1}^{i+1} = v_j^{i+1} (\phi_{j+1}^{i+1} - \phi_{j-1}^{i+1}) \quad (3.10)$$

Node N (backward-differences)

$$\phi_n^{i+1} = \bar{\phi}_n^i + \lambda_r [v_{n-2}^i - 4v_{n-1}^i + 3v_n^i] + u_n^i (\phi_{n-2}^i - 4\phi_{n-1}^i + 3\phi_n^i) \quad (3.11)$$

$$u_n^{i+1} = \text{prescribed} \quad (3.12)$$

$$v_n^{i+1} = \text{prescribed} \quad (3.13)$$

$$u_{n-2}^{i+1} - 4u_{n-1}^{i+1} + 3u_n^{i+1} = v_n^{i+1} (\phi_{n-2}^{i+1} - 4\phi_{n-1}^{i+1} + 3\phi_n^{i+1}) \quad (3.14)$$

Here the subscript j is used to denote the node number while the superscript i denotes the time step. The spacing ratio λ_r is given by $\lambda_r = \frac{\Delta t}{2\Delta s}$ and $m_1 = m + m_a$. The overbar is used to denote a term which has been modified to include the necessary artificial dissipation. If additional dissipation was not required, the overbar would simply be removed. In terms of the general variable q , \bar{q} is given by

$$\begin{aligned} \bar{q}_1^i &= q_1^i + \frac{2\lambda\alpha}{\Delta s} (q_1^i - 2q_2^i + q_3^i) \\ \bar{q}_j^i &= q_j^i + \frac{2\lambda\alpha}{\Delta s} (q_{j-1}^i - 2q_j^i + q_{j+1}^i) \\ \bar{q}_n^i &= q_n^i + \frac{2\lambda\alpha}{\Delta s} (q_n^i - 2q_{n-1}^i + q_{n-2}^i). \end{aligned} \quad (3.15)$$

It should be noted at this point that (3.10) and (3.14) are written as implicit statements.

This is a necessary modification for the solution procedure. Briefly, the algorithm proceeds in the following manner. First the unknown angles are solved for directly using (3.3), (3.7) and (3.11). Next, (3.4), (3.5), (3.8), (3.9), (3.12), and (3.13) are introduced into (3.10) and (3.14). By including (3.6), a $n \times n$ matrix is formed with which to solve for the unknown tension values. These values are then used to solve directly for the velocities. This procedure is then repeated through the desired number of time steps. Within the algorithm, the banded structure of the matrix is exploited. Therefore, the matrix solution takes roughly n operations and is only performed once per time-step.

3.3.3 Explicit Scheme Results

At the present time, the most widely used finite-difference solver for the cable equations without bending stiffness is the implicit routine first developed by Ablow and Schechter [1]. Therefore results obtained with the explicit scheme will be directly compared with this method. The implicit method will be discussed in greater detail in the next section.

The three main concerns associated with the development of any numerical algorithm are accuracy, stability and computational efficiency. These topics are all closely related. On the basis of accuracy, the implicit scheme is superior in that second-order approximations are used for evaluating the time derivatives while the explicit scheme is only first-order in time (use of second-order differences in the explicit scheme proved highly unstable and was therefore abandoned). In addition, some error is introduced within the explicit scheme by the addition of numerical viscosity. Both methods prove stable provided sufficient numerical dissipation is added to the explicit scheme. Excessive amounts of dissipation will inhibit accuracy, however, therefore the explicit scheme is limited to some degree in choice of stepping parameters. With regard to efficiency, the explicit scheme appears to hold an advantage in that no iterations are required and the matrix problem is four times smaller. Therefore, for comparable stepping increments, the implicit scheme requires at least eight times more operations, assuming only two iterations per time step and that solution of an $n \times n$ banded matrix problem is on the order of n operations.

A direct comparison between the methods was obtained by studying the motions of a hanging chain in air. For small motions, an analytic solution for the displacement $q(t,s)$

Finite-Difference Method	# of Nodes	Time-step
Explicit	80	0.002
Implicit	80	0.016

Table 3.1: Case studies for hanging chain problem

may be obtained in terms of Bessel functions, and is given by [74]

$$q_n(t, s) = J_0(2\omega_n \sqrt{s}) \sin(\omega_n t). \quad (3.16)$$

The third mode was used in the analysis ($\omega_3 L = 4.327$) and the velocities were initialized within the algorithms according to (3.16). Several cases, involving a wide range of stepping increments were studied and two indicative cases are listed in 3.1. For the explicit method, the instability was generated near the top boundary, therefore additional dissipation was incorporated near this point. The stepping increments were chosen so as to keep the relative error in the explicit solution below 0.5 percent. The two cases are roughly comparable in computation effort.

The results obtained are shown in figures 3.2 and 3.3. The error measure is based on the rms difference between the analytic and numerical solutions, expressed as a percentage of the maximum displacement. As figure 3.2 shows, it is possible to obtain comparable results with the explicit scheme, in some cases, provided the dissipation is added correctly. Figure 3.3 depicts the cable shape at various times and shows the error incurred by both methods. For reduced stepping increments, both methods converge to the analytic result.

The two methods were applied to a second problem involving a positively buoyant cable, pinned at the bottom, subject to a sinusoidal current with a period of 1.0 seconds. The results are shown in figure 3.4. Computational time was roughly equivalent. As readily seen, both methods converge to the same result. Therefore, the explicit scheme provides a means with which to compare the results of the implicit scheme. In addition, unlike the implicit scheme, the explicit scheme does not become singular for zero initial tension. This is due to the fact that the tensions are deliberately cast as the unknowns in the matrix

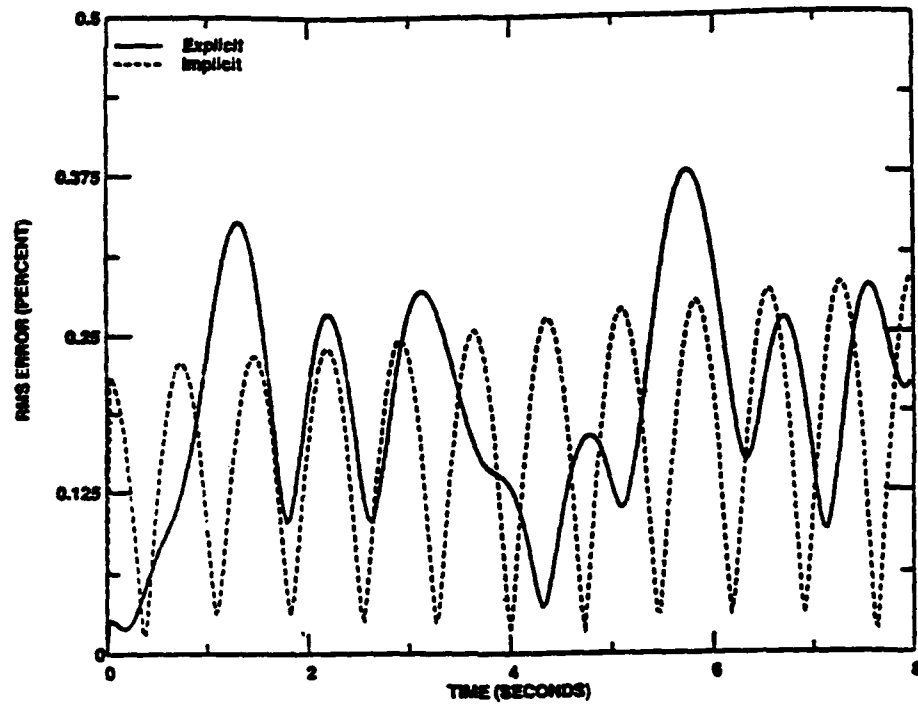


Figure 3.2: Comparison of calculated error associated with each case study.

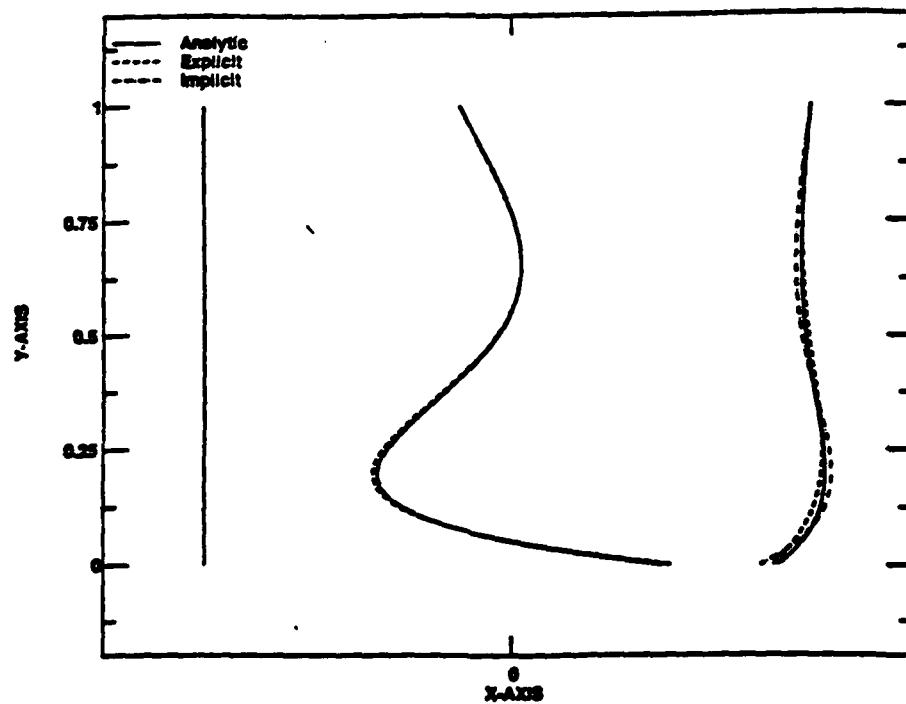


Figure 3.3: Calculated cable shapes for hanging chain problem at times $t=0.0$, 4.0 and 6.5 seconds.

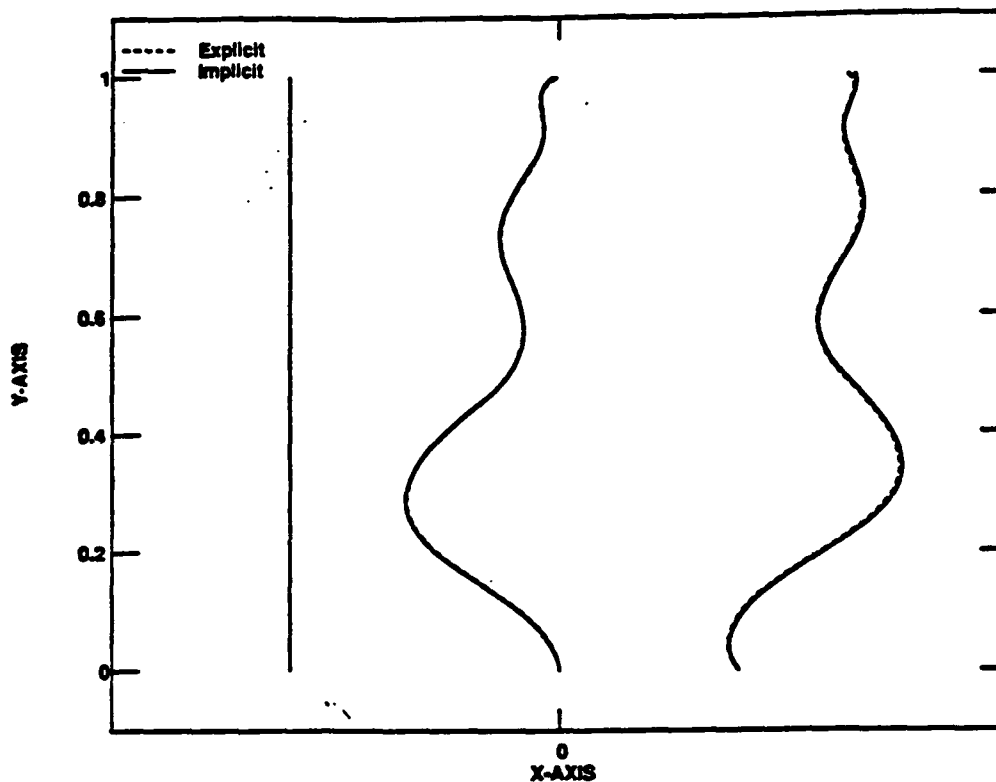


Figure 3.4: Calculated cable shape from explicit and implicit schemes for anchored cable subjected to a sinusoidal current, at times $t=0.0$, 6.0 , and 15.5 seconds.

problem. The explicit scheme may therefore be used to study a wider range of initial value problems.

In general, for simulations with longer time spans, the artificial dissipation term may begin to affect the solution accuracy. Therefore, the explicit scheme is better suited for transient problems and can be used in conjunction with an implicit scheme to step-through computationally difficult periods. In submerged cable problems, however, the fluid drag provides additional damping, thereby helping to stabilize the explicit scheme. For such problems the explicit method retains its accuracy over long time spans.

3.4 Implicit Formulation with Bending Stiffness

Little research has been conducted, in the past, on the effects of bending stiffness. This is attributable to the fact that for long taut cables, as typically studied, bending forces are

often negligible. Sanders [60] developed two criteria for analyzing the importance of bending stiffness. First the internal shear force must be significantly lower than the cable tension. Secondly, for a cable of constant curvature, in which the shear force vanishes, the tension in the fibers due to pure bending must be less than the cable tension. The nondimensional analysis conducted in chapter 2 also provides guidance as to when bending effects can be neglected. For low-tension cables, large deformations can occur which give rise to shear forces that can be of equal magnitude as the cable tension. Therefore, bending stiffness must be included for such cases.

McCoy [41] found that significant stress differences arise in the neighborhood of concentrating loadings if bending stiffness is retained. He found the magnitude of these differences was independent of the amount of bending stiffness, however the extent over which these differences occur diminishes with decreased bending stiffness.

Ketchman and Lou [32] developed a two-dimensional finite-element model with bending stiffness. They applied their method to towed cables and determined that the effects of bending stiffness were confined to a region near the free end of the cable, where the tension was lowest. Their approach, however, is limited in its applications as inertial forces were neglected.

3.4.1 Equations of Motion and Boundary Conditions

The three-dimensional nonlinear equations of motion, as given by (2.41), can be expressed in matrix form as follows:

$$M \frac{\partial \vec{Y}}{\partial s} = N \frac{\partial \vec{Y}}{\partial t} + \vec{Q} \quad (3.17)$$

where

$$\vec{Y} = (T, S_n, S_b, u, v, w, \phi, \theta, \Omega_2, \Omega_3)^T \quad (3.18)$$

$$M = \begin{bmatrix} 1 & 0 & 0 & 0 & 0 & 0 & 0 & 0 & 0 & 0 \\ 0 & 1 & 0 & 0 & 0 & 0 & 0 & 0 & 0 & 0 \\ 0 & 0 & 1 & 0 & 0 & 0 & 0 & 0 & 0 & 0 \\ 0 & 0 & 0 & 1 & 0 & 0 & 0 & 0 & 0 & 0 \\ 0 & 0 & 0 & 0 & 1 & 0 & 0 & 0 & 0 & 0 \\ 0 & 0 & 0 & 0 & 0 & 1 & 0 & 0 & 0 & 0 \\ 0 & 0 & 0 & 0 & 0 & 0 & \cos \theta & 0 & 0 & 0 \\ 0 & 0 & 0 & 0 & 0 & 0 & 0 & 1 & 0 & 0 \\ 0 & 0 & 0 & 0 & 0 & 0 & 0 & 0 & EI & 0 \\ 0 & 0 & 0 & 0 & 0 & 0 & 0 & 0 & 0 & EI \end{bmatrix}$$

$$N = \begin{bmatrix} 0 & 0 & 0 & m & 0 & 0 & -mv \cos \theta & mw & 0 & 0 \\ 0 & 0 & 0 & 0 & m + m_a & 0 & mu \cos \theta + mw \sin \theta & 0 & 0 & 0 \\ 0 & 0 & 0 & 0 & 0 & m + m_a & -mv \sin \theta & -mu & 0 & 0 \\ \frac{1}{EA} & 0 & 0 & 0 & 0 & 0 & 0 & 0 & 0 & 0 \\ 0 & 0 & 0 & 0 & 0 & 0 & (1 + \frac{T}{EA}) \cos \theta & 0 & 0 & 0 \\ 0 & 0 & 0 & 0 & 0 & 0 & 0 & -(1 + \frac{T}{EA}) & 0 & 0 \\ 0 & 0 & 0 & 0 & 0 & 0 & 0 & 0 & 0 & 0 \\ 0 & 0 & 0 & 0 & 0 & 0 & 0 & 0 & 0 & 0 \\ 0 & 0 & 0 & 0 & 0 & 0 & 0 & 0 & 0 & 0 \\ 0 & 0 & 0 & 0 & 0 & 0 & 0 & 0 & 0 & 0 \end{bmatrix}$$

$$\bar{Q} = \begin{bmatrix} S_n \Omega_3 - S_b \Omega_2 + w_o \cos \phi \cos \theta - R_{d1} \\ -\Omega_3(T + S_b \tan \theta) - w_o \sin \phi - R_{d2} + m_a \frac{\partial J_2}{\partial t} \\ S_n \Omega_3 \tan \theta + T \Omega_2 + w_o \cos \phi \sin \theta - R_{d3} + m_a \frac{\partial J_3}{\partial t} \\ \Omega_3 v - \Omega_2 w \\ -\Omega_3(v + w \tan \theta) \\ \Omega_3 v \tan \theta + \Omega_2 u \\ \Omega_3 \\ \Omega_2 \\ EI \Omega_3^2 \tan \theta + S_b(1 + \frac{T}{EA}) \\ EI \Omega_2 \Omega_3 \tan \theta - S_n(1 + \frac{T}{EA}) \end{bmatrix}$$

To complete the mathematical formulation we must consider boundary conditions. One end of the cable ($s = 0$) is considered as a free boundary while the other end ($s = L$) is pinned to an anchor or ship. At the free boundary, the tension, moment, and shear forces are all zero. At the pinned end, the three velocities are prescribed and the moments are set equal to zero. Mathematically, these boundary conditions are expressed as follows:

$$T(t, 0) = 0 \quad (3.19)$$

$$EI \Omega_2(t, 0) = 0$$

$$EI \Omega_3(t, 0) = 0$$

$$EI \frac{\partial \Omega_2(t, 0)}{\partial s} = 0$$

$$EI \frac{\partial \Omega_3(t, 0)}{\partial s} = 0$$

$$u(t, L) = U(t)$$

$$v(t, L) = V(t)$$

$$w(t, L) = W(t)$$

$$EI \Omega_2(t, L) = 0$$

$$EI \Omega_3(t, L) = 0$$

where $U(t)$, $V(t)$, and $W(t)$ are some known velocities. In this fashion, the required ten boundary conditions are imposed and an equal number are applied at each boundary.

3.4.2 Finite-Difference Approximation

As with any finite difference formulation the cable is first discretized into n nodes, separated by Δs , and time is divided into a series of steps of length Δt . The set of equations given by (3.18) are solved at the midpoint between nodes j and $j + 1$, denoted by $j + \frac{1}{2}$, and at the time $i + \frac{1}{2}$. The partial derivatives in (3.18) are expressed using centered finite differences as follows:

$$\begin{aligned}\frac{\partial Y}{\partial t} &= \frac{Y_j^{i+1} - Y_j^i}{\Delta t} \\ \frac{\partial Y}{\partial s} &= \frac{Y_{j+1}^i - Y_j^i}{\Delta s}\end{aligned}\quad (3.20)$$

Introducing (3.20) into (3.18) and evaluating the equations at $j + \frac{1}{2}$ and $i + \frac{1}{2}$ yields

$$\begin{aligned}&[M_{j+1}^{i+1} + M_j^{i+1}] \frac{Y_{j+1}^{i+1} - Y_j^{i+1}}{\Delta s} + [M_{j+1}^i + M_j^i] \frac{Y_{j+1}^i - Y_j^i}{\Delta s} = \\&[N_{j+1}^{i+1} + N_{j+1}^i] \frac{Y_{j+1}^{i+1} - Y_{j+1}^i}{\Delta t} + [N_j^{i+1} + N_j^i] \frac{Y_j^{i+1} - Y_j^i}{\Delta t} + \\&Q_{j+1}^{i+1} + Q_j^{i+1} + Q_{j+1}^i + Q_j^i.\end{aligned}\quad (3.21)$$

This provides $10(n - 1)$ equations with which to solve for the $10n$ unknowns. The remaining equations are provided by the 10 boundary conditions.

The set of difference equations given by (3.21), along with the boundary conditions, provide a coupled set of nonlinear equations with which to solve for the new time values. A Newton-Raphson [14] iteration scheme is used to solve for the unknown variables. Several iterations per time-step may be required for convergence. However, the banded structure of the resulting matrix can be exploited, reducing the computations to roughly n operations per iteration.

Ablow and Schechter [1] base the stability of their numerical scheme on the determinant

of the M matrix. This is because this matrix is inverted within their algorithm. If bending stiffness is neglected, we find that

$$\det M = -T^2 \cos \theta. \quad (3.22)$$

Therefore, if the cable loses tension during the computations, or if the tension is zero initially, their method becomes unstable. In the numerical scheme outlined here, the M is never actually inverted, however method still fails due the zero tension singularity in the equations of motion. The method will also become unstable if the cable becomes horizontal in the out-of-plane direction (i.e. $\theta = \frac{\pi}{2}$ or $\frac{3\pi}{2}$). This singularity stems from an ambiguity in the reference system and can be controlled, but not removed entirely, by selecting an alternative Euler rotation sequence.

A markedly different result is obtained if bending stiffness is retained. The determinant of the M matrix shown here is easily obtained by taking the product of the trace yielding

$$\det M = (EI)^2 \cos \theta. \quad (3.23)$$

Therefore, provided the bending stiffness is finite, the matrix can be inverted, regardless of the cable tension magnitude. Howell [22] has previously demonstrated that incorporating bending stiffness eliminates the zero tension singularity for the two-dimensional case.

3.4.3 Implicit Scheme Results

The implicit scheme has been verified within the linear regime, and the effect of bending stiffness on the dynamics has been studied by Howell [22]. Figure 3.5 compares two-dimensional results for a cable, subjected to a sinusoidal current of period 1.0 seconds, with and without bending stiffness. A relatively large nondimensional bending stiffness term of $EI/mgL^3 = 10^{-3}$ was implemented for the analysis. As readily seen, the cable shape is significantly altered with the curvature being greatly reduced by bending stiffness. In particular, bending-stiffness effects were greatest over the top half of the cable. This is due to the lower cable tension in this region and demonstrates the physical importance of bending stiffness in regions of low tension.

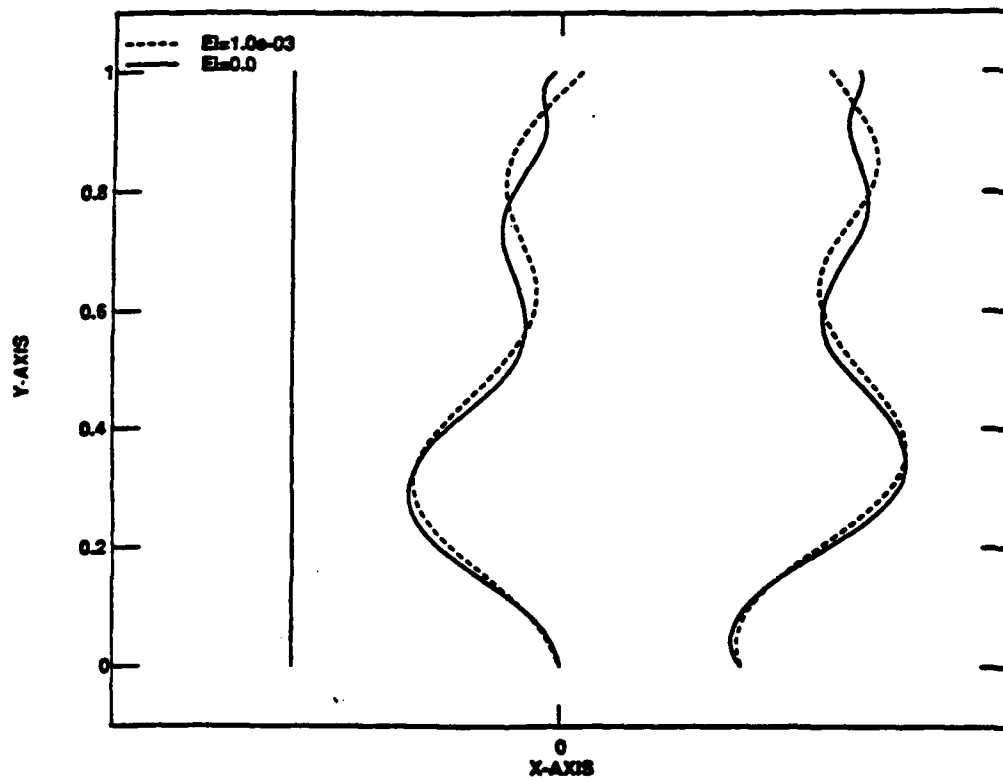


Figure 3.5: Effects of bending stiffness on anchored cable subjected to a sinusoidal current, at times $t=0.0$, 6.0 and 15.5 seconds.

Chapter 4

Nonlinear Impulsive Motions

4.1 Introduction

In this chapter we explore certain fundamental mechanisms of cable response intrinsic to low tension behavior by considering a cable under zero initial tension. Excitation of the cable is accomplished by the application of an impulsive load at one end and the resulting tension and velocity distribution along the cable is studied for a variety of initial configurations.

Understanding the dynamics of impulsively loaded cables is of importance as low tension cables are often more susceptible to this form of excitation than are taut cables. To understand why this occurs, consider that for low-tension cables, by definition the dynamic tension component is of equal or greater magnitude than the static tension. Therefore, it is very likely that the dynamic tension will act to cancel the static tension over a portion of the loading cycle, a phenomenon often referred to as tension clipping [64]. This can occur even though the initial tension is high. Following the periods of zero tension, tensile forces initially build-up over a short time span and can therefore be considered impulsive. These forces, in turn, can lead to large cable accelerations and maximum cable forces nine times the static payload weight have been found to occur [18].

Needless to say, this can become a highly dangerous situation in many marine operations such as towing. Several authors, including Shin [63], Milgram et al. [43], and Papazoglou et al. [53], have described such dynamics, concentrating primarily on the snap condition, at which the tension is maximum.

Herein we concentrate on the tension distribution and resulting velocities immediately after the application of the impulsive load. The results presented here are summarized in a recent paper by Triantafyllou and Howell [71].

4.2 Formulation of Impulsive Equations of Motion

The equations of motion for a cable under impulsive loading have been derived previously, first by Routh [59] and then Lamb [34], and more recently by Triantafyllou and Howell [71]. As with these previous authors, we consider the cable to be inextensible. This condition of inextensibility is based on the following assumptions: 1) the static tension is of the order of the total weight of the cable; 2) the velocities applied impulsively on the cable are small compared to the speed of elastic waves; and 3) one end of the cable is free or the cable has large sag. The first assumption defines a low tension cable, the primary focus of this research. The second condition ensures that elastic waves will not be excited, while the third condition, combined with the second, ensures that the cable does not stretch considerably. In fact, if one cable end is free, the tension is zero at that point at all times. Therefore, for moderately long cables with high Young's modulus (such as metallic cables), the tension never builds to sufficiently large values to cause substantial stretching. If one end of the cable is not free, however the cable sag is large, elastic effects remain small, even for taut cables. This has been shown by Irvine and Caughey [26]. They determined that the relative parameter which quantifies the effects of elasticity is λ , where

$$\lambda^2 = \frac{EA}{H} \left(\frac{w_0 L}{H} \right)^2. \quad (4.1)$$

Here H denotes the horizontal static force applied at the cable end points. The parameter λ^2 is proportional to the ratio of the elastic to catenary stiffness of the cable. This ratio is typically very large for large sag to span ratios, i.e. large values of $w_0 L/H$. When the elastic stiffness is very large, the cable employs its catenary stiffness, thereby preserving the cable length. In chapter 6 we formally derive the expression for λ .

As in chapter 2, we derive the equations of motion using a lagrangian reference frame, fixed on the cable, and we adopt the same nomenclature defined previously. In this section

we neglect the effects of bending stiffness, however, forces in bending are treated in section 4.4.

The inextensible cable governing equations are given by

$$m \frac{D\vec{V}}{Dt} = \frac{D(T\hat{t})}{Ds} + \vec{R}. \quad (4.2)$$

The impulsive equations of motion are determined by integrating (4.2). We denote $T_i(s)$ as the amplitude of the impulsive tension, developed at time $t = 0^+$, and define the cable's velocity immediately before and after the application of the impulsive tension as \vec{V}^- and \vec{V}^+ , respectively. Integrating (4.2) yields:

$$m(\vec{V}^+ - \vec{V}^-) = \frac{D(T_i\hat{t})}{Ds}. \quad (4.3)$$

We can express (4.3) in component form using the vector $\vec{\Omega}$ to represent the local curvature of the cable. At this point we define $\vec{\Omega} = (\Omega_1, \Omega_2, \Omega_3)$ as the Darboux vector of rotation [21], which is given by the following:

$$\begin{aligned} \Omega_1 &= \frac{1}{\tau} \\ \Omega_2 &= 0 \\ \Omega_3 &= \frac{1}{\rho} \end{aligned} \quad (4.4)$$

where ρ denotes the local radius of curvature and τ the local radius of torsion. Note that we have chosen to adopt the so-called principal directions [21] for the unit vectors $(\hat{t}, \hat{n}, \hat{b})$. This is in contrast to the definitions used in chapter 2, where the orientation of the normal and binormal directions about the tangent direction was chosen arbitrarily. This change has been made here because the use of principal coordinates greatly simplifies the impulsive equations.

Using (4.4), we can express (4.3) in component form yielding

$$\begin{aligned}
m(u^+ - u^-) &= \frac{dT_i}{ds} \\
m(v^+ - v^-) &= T_i \Omega_3 \\
m(w^+ - w^-) &= 0
\end{aligned} \tag{4.5}$$

The compatibility relations are derived on the same basis as in chapter 2, i.e.

$$\frac{D\vec{V}^\pm}{Ds} = \frac{D\hat{i}}{Dt}. \tag{4.6}$$

From (4.6), we find the following relations which are valid for both $t = 0^-$ and $t = 0^+$,

$$\begin{aligned}
\frac{du}{ds} - \Omega_3 v &= 0 \\
\frac{dv}{ds} + \Omega_3 u - \Omega_1 w &= \omega_3 \\
\frac{dw}{ds} + \Omega_1 v &= -\omega_2.
\end{aligned} \tag{4.7}$$

Eliminating the velocities from (4.5) and (4.7) provides a single equation in terms of the impulsive tension.

$$\frac{d^2 T_i}{ds^2} - \Omega_3^2 T_i = 0 \tag{4.8}$$

Equation (4.8) is an important result which shows that the impulsive tension is independent of the geometric torsion, Ω_1 , and depends entirely on the local curvature of the cable given by Ω_3 . From (4.5) we find that the binormal velocity remains constant, while the tangential and normal velocities depend exclusively on the curvature and magnitude of the impulsive tension.



Figure 4.1: Cable in a straight line.

4.3 Solution of Impulsive Dynamics

In this section we use (4.8) to derive closed form analytic results for several initial configurations. These results are used to identify the impulsive tension distribution along the cable, as well as the velocities that develop due to the impulsive loading.

4.3.1 Cable in a straight line

Perhaps the most simple example to consider is a cable of length L , sitting at rest in a straight line configuration on a horizontal frictionless table (figure 4.1). For this case $\Omega_3 = 0$ because the radius of curvature is infinite. One end of the cable is suddenly pulled at an amplitude $T_i(L) = T_0$ while the other end is free, i.e. $T_i(0) = 0$. Using these boundary conditions and (4.8), the solution is obtained as

$$\begin{aligned} T_i(s) &= \frac{T_0 s}{L} \\ u^+(s) &= \frac{T_0}{mL}. \end{aligned} \tag{4.9}$$

All other quantities are zero. From these results we find that if the cable is initially straight, the impulsive tension distribution varies linearly along the cable and the entire cable begins to move in the tangential direction at the same velocity.

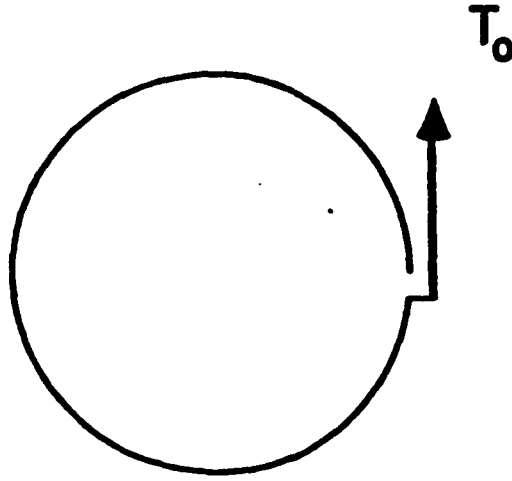


Figure 4.2: Cable in the form of a circle.

4.3.2 Cable in the form of a circle

Another simple example which can be solved exactly is the case of a cable of length L sitting, at rest along a full arc of a circle of radius a , on a horizontal frictionless table (figure 4.2). One end of the cable is suddenly pulled at an amplitude T_0 and the boundary conditions are given by $T_i(0) = 0$ and $T_i(L) = T_0$. The solution of (4.8) is given by

$$\begin{aligned} T_i(s) &= T_0 \frac{\sinh(s/a)}{\sinh(L/a)} \\ u^+(s) &= \frac{T_0 \cosh(s/a)}{ma \sinh(L/a)} \\ v^+(s) &= \frac{T_0 \sinh(s/a)}{ma \sinh(L/a)} \end{aligned} \tag{4.10}$$

The second compatibility relation in (4.7) provides the angular velocity

$$\omega_3(s) = \frac{2T_0 \cosh(s/a)}{ma^2 \sinh(L/a)}. \tag{4.11}$$

4.3.3 Cable in the form of a helix

To show that the initial development of tension is independent from torsion, we consider a cable with a three-dimensional initial configuration resting in the form of a helix, i.e. $\rho = a$ and $\tau = b$, where a and b are constants. Again one end of the cable is suddenly pulled and we impose the same boundary conditions as in the previous example. The exact solution is obtained as follows:

$$\begin{aligned}
 T_i(s) &= T_o \frac{\sinh(s/a)}{\sinh(L/a)} \\
 u^+(s) &= \frac{T_o \cosh(s/a)}{ma \sinh(L/a)} \\
 v^+(s) &= \frac{T_o \sinh(s/a)}{ma \sinh(L/a)} \\
 w^+(s) &= 0 \\
 \omega_3(s) &= \frac{2T_o \cosh(s/a)}{ma^2 \sinh(L/a)} \\
 \omega_2(s) &= -\frac{T_o \sinh(s/a)}{mab \sinh(L/a)}
 \end{aligned} \tag{4.12}$$

As readily seen, the same tension and velocity distribution develops as with the two-dimensional case of a chain in a circle, the only exception being that ω_2 is nonzero. This shows the independence of initially developing tension from torsion.

4.3.4 Cable of reversing curvature

We next consider a cable of length $2L$ at rest on a frictionless horizontal table. The cable configuration is comprised of two circular arcs of radius a and opposite curvature, as shown in 4.3. The curvature Ω_3 is discontinuous at the origin, which is fixed at the midpoint of the cable, jumping from the value $-\frac{1}{a}$ to the value $\frac{1}{a}$. When one end of the cable is suddenly pulled with the impulsive force T_o , the solution can be obtained as done previously, and we find

$$T_i(s) = T_o \frac{\sinh([s+L]/a)}{\sinh(2L/a)} \tag{4.13}$$

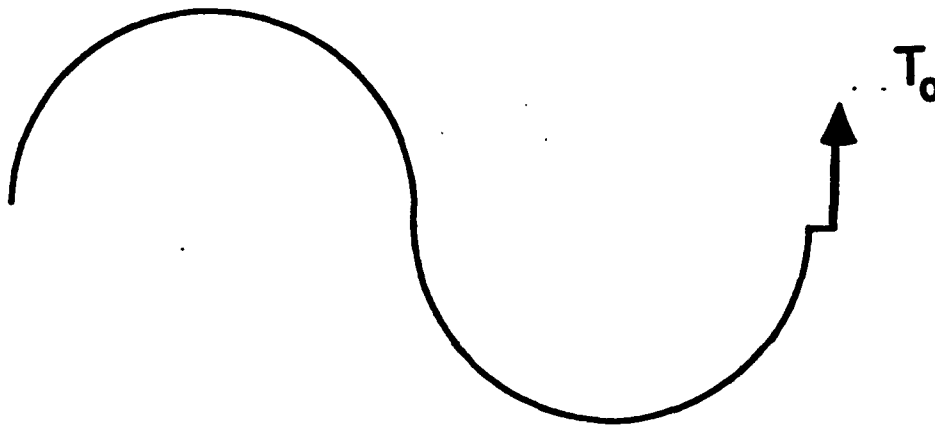


Figure 4.3: Cable of reversing curvature.

This is the same result obtained in the two previous examples, with the exception that here the origin has been shifted and the length of the cable doubled. The tangential velocity is also easily obtained. However, when we proceed to derive the normal velocity, a physically impossible discontinuity appears in the velocity $v^+(s)$ at the point where the curvature is discontinuous. This can be shown by examining the governing equation in the normal direction given by

$$v^+(s) = \frac{1}{m} \Omega_3(s) T_i(s). \quad (4.14)$$

Furthermore, the angular velocity ω_3 develops a singularity, as evidenced in (4.7), when $v(s)$ is discontinuous.

A discontinuity in the curvature is possible only for a perfectly flexible cable. This discontinuity can be removed by introducing the bending stiffness of the cable, which ensures a smooth initial configuration. However, if the singularity identified in the case of reversing curvature is related to a basic cable mechanism, then the manner of smoothing of the solution is of importance.

To determine if in fact this is the case, we consider the same example of a cable with

reversing curvature at rest on a horizontal frictionless table, but we make the curvature reversal smooth. The initial curvature is chosen as

$$\Omega_3(s) = \begin{array}{ll} -1/a & -L \leq s \leq -\epsilon \\ s/a\epsilon & -\epsilon \leq s \leq \epsilon \\ 1/a & \epsilon \leq s \leq L \end{array}$$

where a, ϵ are constants and $\epsilon \ll L$. The solution when one end is impulsively loaded can be obtained separately in the three regions defined above. In the first and third regions the solution for the tension can be obtained explicitly as before, with two unknown constants in each region. In the middle region the equation for the tension becomes:

$$\frac{d^2 T_i}{ds^2} - \frac{s^2}{a^2 \epsilon^2} T_i = 0. \quad (4.15)$$

Using the substitution $s = x\delta$, with $\delta = \sqrt{a\epsilon/2}$, (4.15) can be brought into the standard form of the parabolic cylinder functions:

$$\frac{d^2 T_i}{dx^2} - \frac{x^2}{4} T_i = 0. \quad (4.16)$$

The solution of (4.16) can be expressed as the sum of two independent solutions of the parabolic cylinder equation, scaled with two unknown constants. Since $|x| \leq \sqrt{2\epsilon/a}$, we use the small argument power series expression of the parabolic cylinder functions [2] and match asymptotically the two outer regions with the inner (middle) region. This provides four matching conditions which combined with the two boundary conditions, the same conditions imposed in the previous examples, allows for the solution of all six unknown constants. As ϵ tends to zero, we obtain the following asymptotically valid results:

$$\begin{aligned} T_i(s) &= T_o \frac{\sinh([s+L]/a)}{\sinh(2L/a)} \\ u^+(s) &= \frac{T_o}{ma} \frac{\cosh([s+L]/a)}{\sinh(2L/a)} \\ v^+(s) &= \Omega_3(s) \frac{T_o}{m} \frac{\sinh([s+L]/a)}{\sinh(2L/a)} \end{aligned} \quad (4.17)$$

The rotational velocity suffers from a discontinuity at the edges of the middle region. The expression for ω_3 in the middle region is, asymptotically

$$\omega_3(s) = \frac{T_o}{ma\epsilon} \frac{\sinh(L/a)}{\sinh(2L/a)}. \quad (4.18)$$

The discontinuity at the edges can be removed by requiring that the first derivative of the curvature is everywhere continuous. The importance of (4.18), however, lies in identifying a mechanism for building large rotational velocities. We have found here that at the point of curvature reversal, ω_3 is inversely proportional to the width of the transition region.

4.4 Impulsive Motion of a Cable with Bending Stiffness

In the previous section we have shown the importance of the manner in which the cable curvature is made continuous. For cables, the physical mechanism by which the curvature is made continuous, prior to the application of any load, is bending stiffness. After the cable is loaded, tension also acts to smooth the cable shape. Therefore, because the bending stiffness magnitude affects how the cable is initially made smooth, it is natural to extend the analysis by incorporating bending stiffness. Although the value of the bending stiffness only indirectly affects the dynamic response, for completeness we include bending forces in the dynamic equations as well, to study the direct effects of bending on the impulsive response.

As derived in chapter 2, the governing equations incorporating bending stiffness, are given as

$$m \frac{D\vec{V}}{Dt} = \frac{D\vec{T}}{Ds} + \vec{R}. \quad (4.19)$$

$$\rho_c I \frac{D\vec{\omega}}{Dt} = \frac{D\vec{M}}{Ds} + \vec{i} \times \vec{T} + \vec{Q}. \quad (4.20)$$

Due to the selection of principal coordinates, the moment vector \vec{M} differs slightly from previously presented and is given by

$$M_1 = GI_p \Omega_1 \quad (4.21)$$

$$M_2 = 0$$

$$M_3 = EI \Omega_3.$$

Note that Ω_1 in (4.21) is the material torsion, which is, in general, different from the geometric torsion.

A nondimensional analysis of (4.20) was conducted in section 2.3.2, based on which it was concluded that the inertial forces are negligible. In the context of impulsive forces, however, the relevant time scale is very short and large angular accelerations may develop, depending on the initial configuration. Therefore, we choose to retain these terms here.

If equation (4.20) is integrated in time from $t = 0^-$ to 0^+ , we find that the contribution of the term involving M vanishes, assuming the length of integration is such that insufficient time has elapsed for the cable to alter its initial configuration. As a result, the shear forces may become impulsive as they must balance a step change in the rotational velocity. Otherwise, (4.20) will not be satisfied. One may explain the mechanism generating an impulsive shear force as a limiting process of infinitesimal shear deformation and large shear modulus, in complete analogy with the development of impulsive tension which involves infinitesimal extension and large Young's modulus.

Based on these considerations, we find that when the cable is subject to a forced motion, both the tension and shear forces become impulsive. Therefore, integrating (4.19) and (4.20) over the time period in which the impulsive load is applied yields the following equations of impulsive motion:

$$\begin{aligned} m(\vec{V}^+ - \vec{V}^-) &= \frac{D\vec{T}_i}{Ds} \\ \rho_c I(\vec{\omega}^+ - \vec{\omega}^-) &= \hat{i} \times \vec{T}. \end{aligned} \quad (4.22)$$

Expanding these equations along the $(\hat{i}, \hat{n}, \hat{b})$ system gives

$$\begin{aligned}
m(u^+ - u^-) &= \frac{dT_i}{ds} - S_{ni}\Omega_3 \\
m(v^+ - v^-) &= \frac{dS_{ni}}{ds} + T_i\Omega_3 - S_{bi}\Omega_1 \\
m(w^+ - w^-) &= \frac{dS_{bi}}{ds} + S_{ni}\Omega_1 \\
\rho_c I_p(\omega_1^+ - \omega_1^-) &= 0 \\
\rho_c I(\omega_2^+ - \omega_2^-) &= -S_{bi} \\
\rho_c I(\omega_3^+ - \omega_3^-) &= S_{ni}
\end{aligned} \tag{4.23}$$

together with the compatibility relations (4.7). It is interesting to note that ω_1 did not appear explicitly in the previous equations which neglect bending. The results here show that ω_1 is in fact zero, independent of the initial configuration.

By eliminating the translation and angular velocities in (4.23) and (4.7), we find three equations in terms of the impulsive tension and shear forces (note that, for brevity, the subscript i is omitted).

$$\begin{aligned}
\frac{d^2 T}{ds^2} - T\Omega_3^2 - 2\Omega_3 \frac{dS_n}{ds} - S_n \frac{d\Omega_3}{ds} + \Omega_1 \Omega_3 S_b &= 0 \\
\frac{d^2 S_n}{ds^2} - (\delta^2 + \Omega_1^2 - \Omega_3^2)S_n - 2\Omega_1 \frac{dS_b}{ds} - S_b \frac{d\Omega_1}{ds} + 2\Omega_3 \frac{dT}{ds} + T \frac{d\Omega_3}{ds} &= 0 \\
\frac{d^2 S_b}{ds^2} - (\delta^2 + \Omega_1^2)S_b + 2\Omega_1 \frac{dS_n}{ds} + S_n \frac{d\Omega_1}{ds} + \Omega_1 \Omega_3 T &= 0
\end{aligned} \tag{4.24}$$

where $\delta^2 = m/(\rho_c I)$.

For a cable of circular cross-section, $\delta^2 = 4/r^2$, where r is the radius of the cable cross-section. As a result, we find $\delta \gg (\Omega_1, \Omega_3)$ since neither the radius of curvature nor the radius of geometric torsion can be as small as the radius of the cable. As shown in the next section, this implies the formation of boundary layers in shear.

4.5 Solution of the Cable Equations with Bending Stiffness

As an application we consider the two-dimensional impulsive motion of a cable, and reduce (4.24) to the following:

$$\begin{aligned} \frac{d^2 T}{ds^2} - T \left(\frac{d\phi}{ds} \right)^2 - S_n \frac{d^2 \phi}{ds^2} - 2 \frac{d\phi}{ds} \frac{dS_n}{ds} &= 0 \\ \frac{d^2 S_n}{ds^2} - S_n (\delta^2 - \left(\frac{d\phi}{ds} \right)^2) + T \frac{d^2 \phi}{ds^2} + 2 \frac{d\phi}{ds} \frac{dT}{ds} &= 0 \end{aligned} \quad (4.25)$$

where $\phi(s)$ denotes the initial angle of the tangential vector of the cable with respect to a fixed direction.

We now reconsider the problem of a cable initially at rest in the form of a circle of radius a (figure 4.2). The boundary conditions described previously are imposed, as well as $S_n = 0$ at $s = 0, L$. To provide greater insight into the form of the equations of motion, we normalize the spatial variable s by the radius of curvature and set $x = s/a$. In addition, we define the quantity $\alpha = 4r^2/a^2$, where by physical considerations, $\alpha \ll 1$.

In terms of these quantities, the equations of motion are given as

$$\frac{d^2 T}{dx^2} - T - 2 \frac{dS_n}{dx} = 0 \quad (4.26)$$

$$\alpha \frac{d^2 S_n}{dx^2} - (1 - \alpha) S_n + 2 \frac{dT}{dx} = 0. \quad (4.27)$$

The form of (4.27) clearly suggests the formation of boundary layers in shear because the highest-order derivative term is multiplied by α , meaning that, in general, it is not possible to obtain a solution which satisfies both boundary conditions if the equations are not reformulated near the boundaries. By conducting an asymptotic expansion in terms of α and a boundary layer analysis near $s = 0, L$, we find the following asymptotic solution, valid for $\alpha \ll 1$:

$$T(s) = T_0 \frac{\sinh(s/a)}{\sinh(L/a)} \quad (4.28)$$

$$\begin{aligned}
u^+(s) &= \frac{T_o \cosh(s/a)}{ma \sinh(L/a)} \\
v^+(s) &= \frac{T_o \sinh(s/a)}{ma \sinh(L/a)} \\
S_n(s) &= \frac{2\rho_c I T_o}{ma^2 \sinh(L/a)} (\cosh(s/a) - e^{-2s/r} - e^{-2(L-s)/r} \cosh(L/a)) \\
\omega_3(s) &= \frac{2T_o}{ma^2 \sinh(L/a)} (\cosh(s/a) - e^{-2s/r} - e^{-2(L-s)/r} \cosh(L/a)).
\end{aligned}$$

The correction, therefore, with respect to solution (4.10) is restricted to the boundary layers formed at the two ends, affecting only the shear force, which is order α , and the rotational velocity. Here we find $\omega_3 = 0$ at $s = 0, L$, which differs from the solution given in (4.11). The width of the boundary layer was found to be $1/\delta$.

Next we consider the cable with reversing curvature (figure 4.3), which is the prime example which motivated this analysis. We consider a smooth initial curvature, in the form:

$$\frac{d\phi}{ds} = \frac{\tanh(s/\epsilon)}{a} \quad (4.29)$$

where $\epsilon \ll L$, i.e. the reversal in curvature occurs within a small region. Obviously, ϵ is directly related to the length of the transition region of changing curvature, which in turn depends on the value of the (usually small) bending stiffness of the cable. The initial configuration requires a (small) distributed moment in order to sustain the static shape in the presence of bending stiffness. This moment, however, has an insignificant effect on the developing dynamic response.

A numerical solution of (4.25) for the curvature specified in (4.29) was obtained using centered finite differences. Figure 4.4 shows the tension and rotational velocity along the cable for $\epsilon = 0.01$ and $\delta = 1,000$. The cable length is set equal to 2. As readily seen, a large peak in the rotational velocity occurs at the curvature reversing region, which is inversely proportional to the length over which the curvature reversal occurs (ϵ). Once again the solution for ω_3 contains boundary layers near $s = L$ and the width of the boundary layer depends on δ .

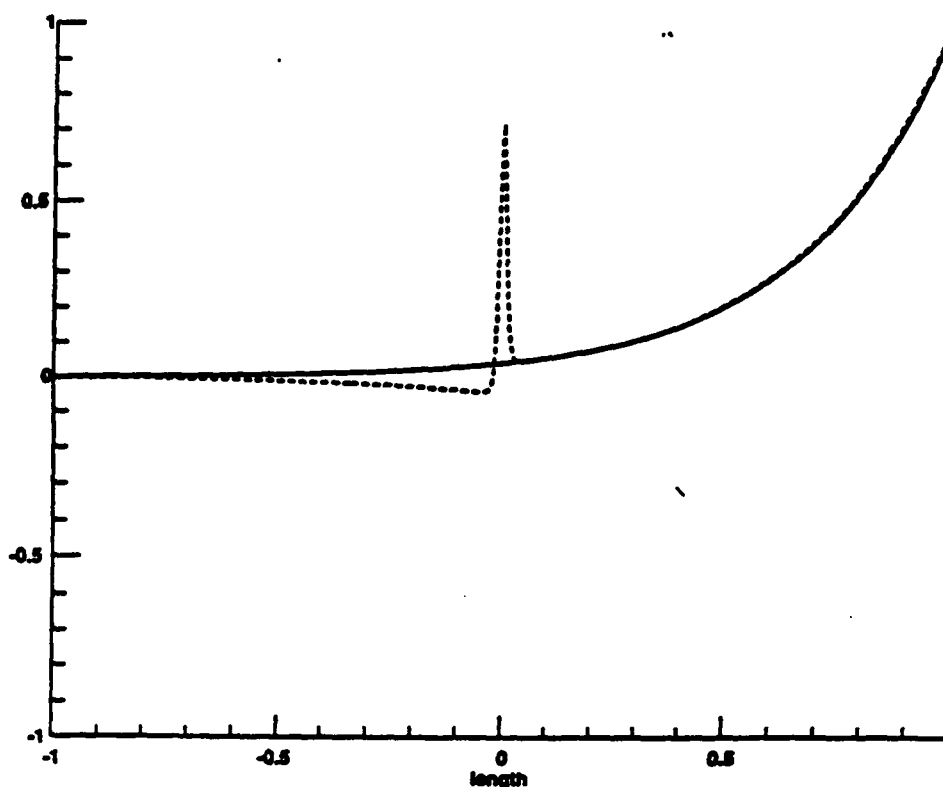


Figure 4.4: Tension (solid line) and angular velocity (dotted line) developing along a cable of reversing curvature (figure 4.3).

4.6 Comparison of Analytic and Numerical Results

The numerical techniques presented in chapter 3 were used to simulate the examples discussed previously. In particular, the explicit finite difference algorithm was used extensively to model the dynamics in the absence of bending stiffness.

Numerical results were obtained for the cable initially in the form of a circle (figure 4.2). Figures 4.5, 4.6, and 4.7 show simulation results for the tension and normal and tangential velocities, respectively, shortly after the impulsive tension was applied at one end. Also shown are the analytic results derived in section 4.3.2. As shown, the two results are nearly indistinguishable.

The example involving a cable of reversing curvature (figure 4.3) was simulated numerically as well. A curvature change, as described in section 4.3.4 was implemented, using a moderately small value of $\epsilon = 0.01$ to avoid the development of sharp boundary layers.

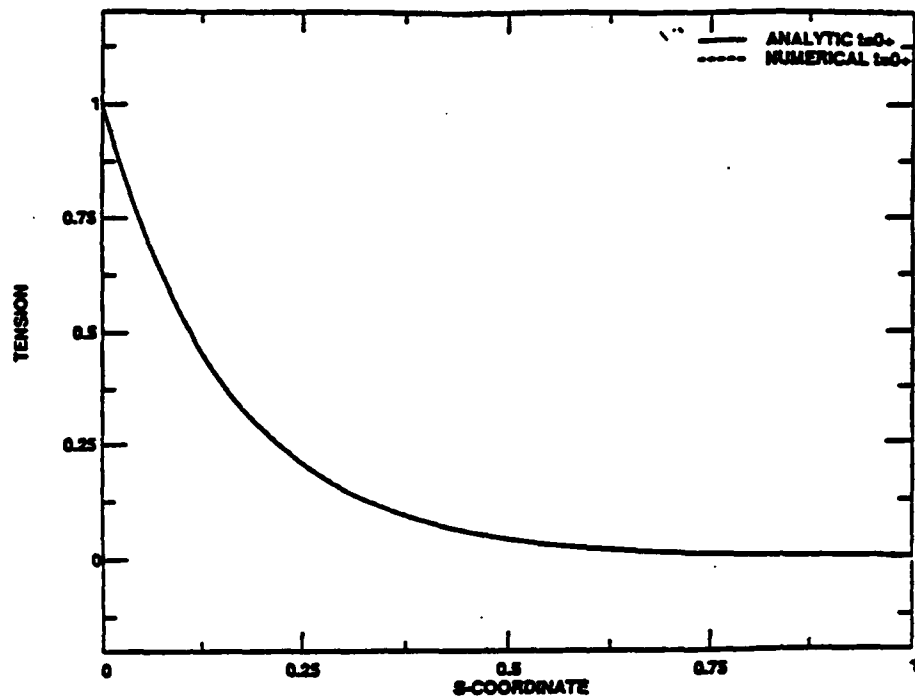


Figure 4.5: Analytically and numerically predicted tension along a cable lying in a circle (figure 4.2) immediately after the application of impulsive loading.

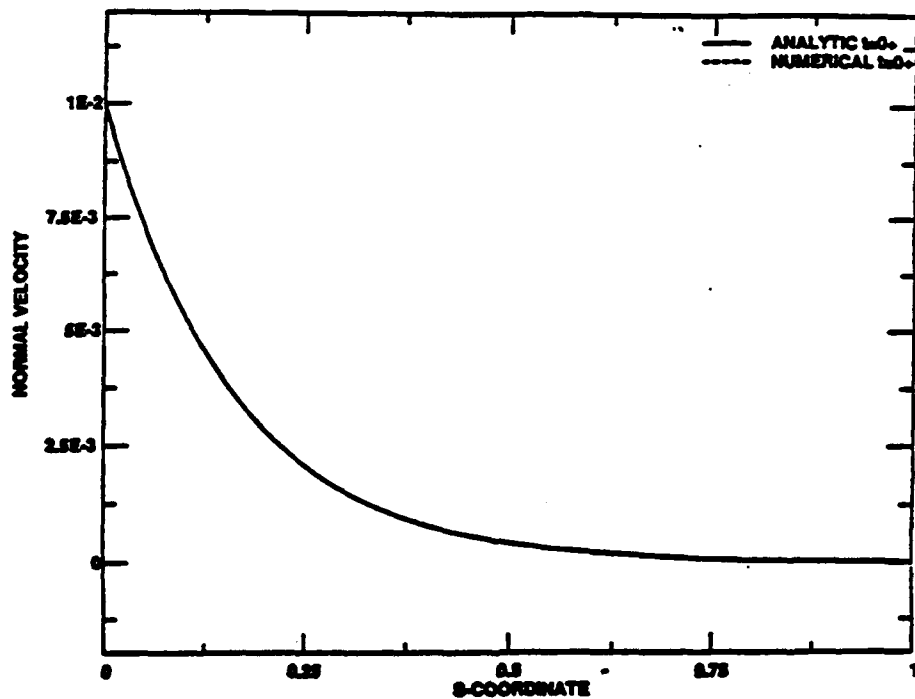


Figure 4.6: Analytically and numerically predicted normal velocity along a cable lying in a circle (figure 4.2) immediately after the application of impulsive loading.

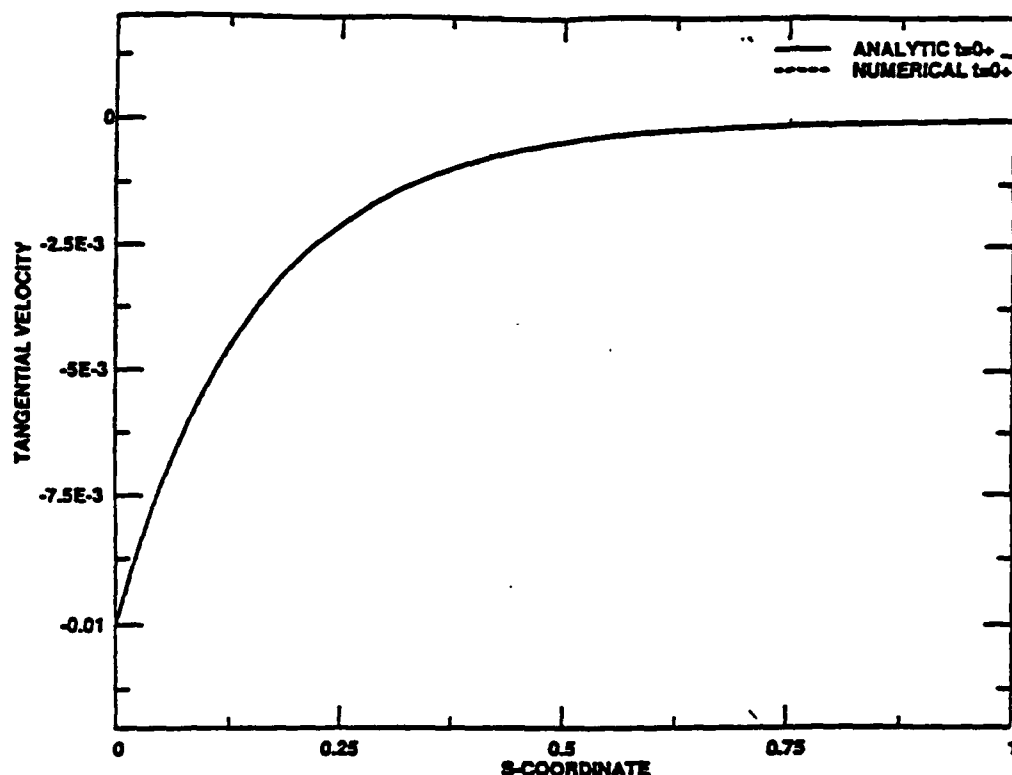


Figure 4.7: Analytically and numerically predicted tangential velocity along a cable lying in a circle (figure 4.2) immediately after the application of impulsive loading.

Figure 4.8 shows the normal velocity immediately after the application of the impulsive load (solid line). This solution coincides with the analytic results, provided a sufficient number of nodes are used in the numerical scheme to ensure adequate treatment of the boundary layer-type behavior. As predicted analytically, a steep change in the normal velocity occurs at the point of changing curvature. Also shown is the response at several times after the initial loading. We find that the effect of the large angular velocity imparted at the cable midpoint spreads over an increasingly larger region with time, demonstrating the significance of the mechanism, particularly for small values of ϵ .

In the next chapter, impulsive tension forces are addressed further, in the context of a harmonically excited hanging chain. In this case, the tension prior to loading varies linearly along the chain length.

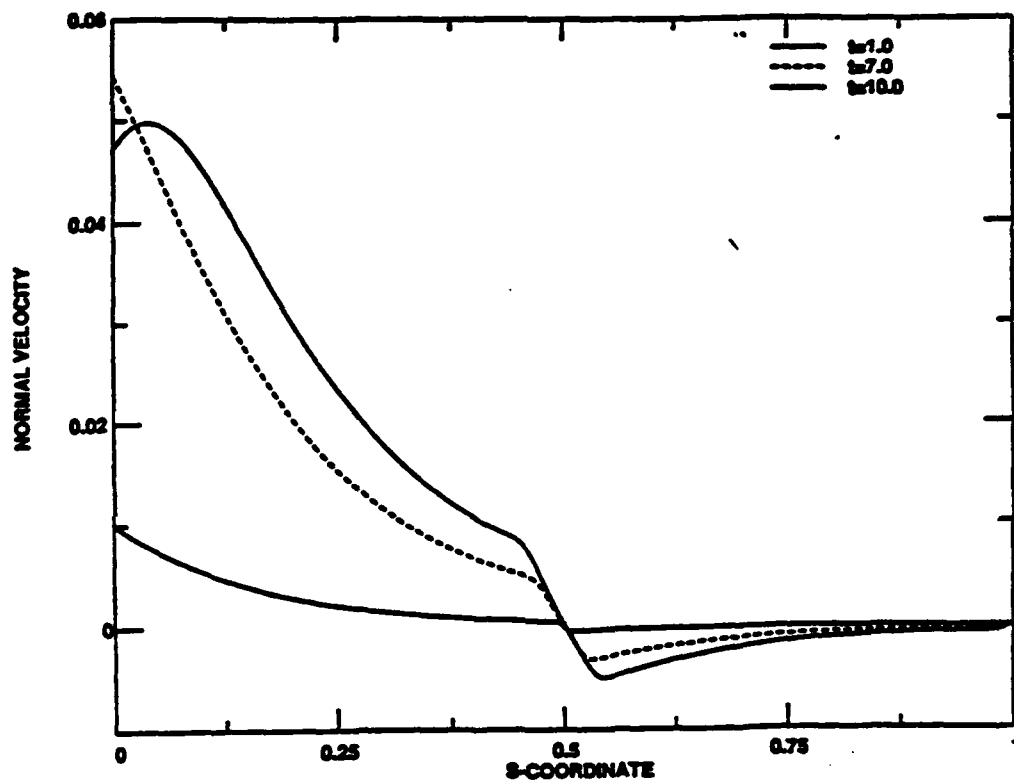


Figure 4.8: Transverse velocity along cable having initial configuration shown in figure 4.3, at three time intervals.

Chapter 5

Analysis of Response of Hanging Chain

5.1 Introduction

A chain hanging freely under its own weight is subject to a static tension component which varies linearly over the chain length, beginning with zero tension at the free boundary. As such, a hanging chain exhibits both high tension behavior (near the top boundary) and low tension behavior (near the free boundary) along its span. Therefore, the hanging chain problem affords an opportunity to study the dynamics in both tension regions as well as the transition between high and low tension behavior.

Herein we investigate the nonlinear dynamics of a hanging chain, driven by a planar harmonic excitation at the top, first analytically and numerically and then experimentally. We consider the dynamics of the chain in air to isolate and study the effects of geometric nonlinearities. As detailed by Triantafyllou and Howell [73], asymptotic results demonstrate a sensitive dependence on excitation frequency and amplitude. Results for moderately large excitation amplitudes identify the existence of separate regions of stable two-dimensional and stable three-dimensional response as a function of frequency, as well as a distinct region in which all steady state solutions are found to be unstable. Numerical and experimental studies were conducted to confirm these findings.

The finding of a three-dimensional response to a planar excitation has been shown

previously by other researchers studying the nonlinear dynamics of cables or strings as well. Neyfeh [47] and then Miles [42] studied the nonlinear dynamics of a stretched string, pinned at one end and subject to a harmonic planar excitation over its length. They found that three-dimensional whirling motions develop over a discrete range of excitation frequencies. Perkins [54] found similar results for a suspended shallow sag cable subject to an end point excitation. These previously studied problems differ from the present analysis in that they each involved a constant static tension along the cable or string. To the author's knowledge, this is the first asymptotic analysis of a chain with variable static tension.

In this chapter we develop in detail the principal derivations and asymptotic results first presented by Triantafyllou and Howell [73]. In addition, numerical and experimental results which were used to verify the asymptotic solutions are discussed. These results have been summarized in a second paper by Triantafyllou and Howell [72]. Finally, we concentrate on the response of the chain for larger excitation amplitudes.

5.2 Formulation of the Problem

The problem under consideration is the three-dimensional dynamics of a chain, hanging freely under its own weight, as shown in figure 5.1. Here we simplify the governing equations derived in chapter 2 in the following manner. First, chains, unlike cables, are perfectly flexible and therefore no forces arise due to bending stiffness. Secondly, because we are considering the dynamics in air, the hydrodynamic effects of added mass and drag are neglected. This creates some complications in that in the absence of damping, transient motions will not decay. We therefore will consider the affect of incorporating a linear drag model in section 5.3.2. Finally, the chain is considered to be inextensible. Due to the condition for zero tension at the lower end, this assumption is valid provided the excitation frequencies are small compared to the first elastic natural frequency and the imposed velocities are small compared to the speed of elastic waves [71].

The governing equations and compatibility relations for the hanging chain problem are found to be

$$\begin{aligned}
m\left(\frac{\partial u}{\partial t} + \frac{\partial \theta}{\partial t}w - \frac{\partial \phi}{\partial t}v \cos(\theta)\right) &= \frac{\partial T}{\partial s} - mg \cos(\phi) \cos(\theta) \\
m\left(\frac{\partial v}{\partial t} + \frac{\partial \phi}{\partial t}u \cos(\theta) + \frac{\partial \phi}{\partial t}w \sin(\theta)\right) &= T \frac{\partial \phi}{\partial s} \cos(\theta) + mg \sin(\phi) \\
m\left(\frac{\partial w}{\partial t} - \frac{\partial \phi}{\partial t}v \sin(\theta) - \frac{\partial \theta}{\partial t}u\right) &= -T \frac{\partial \theta}{\partial s} - mg \cos(\phi) \sin(\theta) \\
\frac{\partial v}{\partial s} + \frac{\partial \phi}{\partial s}u \cos(\theta) + \frac{\partial \phi}{\partial s}w \sin(\theta) &= \frac{\partial \phi}{\partial t} \cos(\theta) \\
\frac{\partial w}{\partial s} - \frac{\partial \phi}{\partial s}v \sin(\theta) - \frac{\partial \theta}{\partial s}u &= -\frac{\partial \theta}{\partial t} \\
\frac{\partial u}{\partial s} + \frac{\partial \theta}{\partial s}w - \frac{\partial \phi}{\partial s}v \cos(\theta) &= 0.
\end{aligned} \tag{5.1}$$

The chain is considered to be excited harmonically at the top. This excitation is confined to the global x-y plane and the excitation frequency λ is chosen close to one of the natural frequencies, defined as ω . A small transverse velocity is imposed at the top, given by:

$$v(t, s = L) = \alpha V_0 \cos(\lambda t). \tag{5.2}$$

where V_0 is the velocity amplitude corresponding to a motion amplitude $Y_0 = V_0/\lambda$ and α is a small positive number, $\alpha \ll 1$. In addition, zero tension is imposed at the lower end ($s = 0$) and the velocities, u and w are set to zero at the upper boundary ($s = L$).

Due to the direction of the excitation, we adopt the terminology that v and ϕ represent the in-plane velocity and angle, respectively, while w and θ represent these quantities in the out-of-plane direction.

5.3 Analytic Analysis

In this section we derive the analytic solutions using asymptotic techniques. The main goal of the analytic studies was to determine the response of the chain to a wide range of excitation frequencies and amplitudes. In particular, the motions at the free end of the chain are discussed.

5.3.1 Asymptotic Solution

The first step toward obtaining an analytic solution of the hanging chain equations was to employ a perturbation expansion. This expansion is made in terms of the small parameter ϵ , where ϵ is given by $\alpha = \epsilon^3$. The nature of the equations dictates that the tangential velocity and tension are even functions in ϵ while the remaining variables include only odd terms. Therefore, incorporating the static solution, the perturbation expansion can be written as follows:

$$u(s, t) = \epsilon^2 u_2(s, t) + \epsilon^4 u_4(s, t) + O(\epsilon^6) \quad (5.3)$$

$$v(s, t) = \epsilon v_1(s, t) + \epsilon^3 [v_3(s, t) + V_0 \cos(\lambda t) \frac{s}{L}] + O(\epsilon^5)$$

$$w(s, t) = \epsilon w_1(s, t) + \epsilon^3 w_3(s, t) + O(\epsilon^5)$$

$$\phi(s, t) = \epsilon \phi_1(s, t) + \epsilon^3 [\phi_3(s, t) + \frac{Y_0}{L} \sin(\lambda t)] + O(\epsilon^5)$$

$$\theta(s, t) = \epsilon \theta_1(s, t) + \epsilon^3 \theta_3(s, t) + O(\epsilon^5)$$

$$T(s, t) = mgs + \epsilon^2 T_2(s, t) + \epsilon^4 T_4(s, t) + O(\epsilon^6).$$

The expanded variables given by (5.3) are substituted into the governing equations and compatibility relations and terms of each order in ϵ are grouped together. The equations to first order in ϵ are found to be

$$\begin{aligned} m \frac{\partial v_1}{\partial t} &= mgs \frac{\partial \phi_1}{\partial s} + mg\phi_1 \\ \frac{\partial \phi_1}{\partial t} &= \frac{\partial v_1}{\partial s} \\ m \frac{\partial w_1}{\partial t} &= -mgs \frac{\partial \theta_1}{\partial s} - mg\theta_1 \\ \frac{\partial \theta_1}{\partial t} &= -\frac{\partial w_1}{\partial s}. \end{aligned} \quad (5.4)$$

With regard to the first-order equations, two points are worthy of note. First, as expected, these equations represent the linear solution of the hanging chain problem. Secondly, no coupling between in-plane and out-of-plane motions exists to first order.

The first-order equations can be reduced to the following:

$$\begin{aligned}\frac{\partial^2 \phi_1}{\partial t^2} &= 2g \frac{\partial \phi_1}{\partial s} + g^2 \frac{\partial^2 \phi_1}{\partial s^2} \\ \frac{\partial^2 \theta_1}{\partial t^2} &= 2g \frac{\partial \theta_1}{\partial s} + g^2 \frac{\partial^2 \theta_1}{\partial s^2}.\end{aligned}\tag{5.5}$$

These equations are straight-forward to solve using the method of separation of variables [10] and the solution is given by

$$\begin{aligned}\phi_1 &= A(t) \frac{J_1(z)}{z} \\ \theta_1 &= B(t) \frac{J_1(z)}{z}.\end{aligned}\tag{5.6}$$

where $z = 2\omega\sqrt{s/g}$, $J_n(z)$ denotes the Bessel function of the first kind and order n , and $A(t)$ and $B(t)$ represent time dependent amplitudes. In concurrence with the method of multiple time scales [4], the unknown amplitudes are decomposed into functions of two time scales, t and τ , where τ represents the long time scale, which is given by $\tau = \epsilon^3 t$, anticipating the final result. This relation between time scales was selected because secular terms first arise at order ϵ^3 . The amplitudes are then expressed as follows:

$$\begin{aligned}A(t) &= A_1(\tau)e^{i\omega t} + cc \\ B(t) &= B_1(\tau)e^{i\omega t} + cc\end{aligned}\tag{5.7}$$

where i is the imaginary unit, cc denotes the complex conjugate of the preceding quantity. Using these results, we may now solve for the first-order velocities.

$$\begin{aligned}v_1 &= -\frac{g}{2\omega}(iA_1e^{i\omega t} + cc)J_0(z) \\ w_1 &= \frac{g}{2\omega}(iB_1e^{i\omega t} + cc)J_0(z).\end{aligned}\tag{5.8}$$

The natural frequencies are obtained from the requirement that, to first order in ϵ , the transverse velocities v and w are zero at $s = L$. This results in the classical equation for the natural frequencies of a hanging chain, as given by

$$J_0(z_0) = 0 \quad (5.9)$$

where

$$z_0 = 2\omega\sqrt{\frac{L}{g}}. \quad (5.10)$$

The second order equations in ϵ are found to be given by

$$\begin{aligned} m\left(\frac{\partial u_2}{\partial t} + w_1 \frac{\partial \theta_1}{\partial t} - v_1 \frac{\partial \phi_1}{\partial t}\right) &= \frac{\partial T_2}{\partial s} + mg \frac{\phi_1^2 + \theta_1^2}{2} \\ \frac{\partial u_2}{\partial s} &= v_1 \frac{\partial \phi_1}{\partial s} - w_1 \frac{\partial \theta_1}{\partial s}. \end{aligned} \quad (5.11)$$

Solving these equations for T_2 and u_2 and imposing $u_2(t, s = L) = 0$, we find

$$\begin{aligned} u_2 &= \frac{g}{4\omega}((A^2 + B^2)e^{2i\omega t} + cc)h_1(z) \\ T_2 &= \frac{mg^2}{8\omega^2}[(2AA^* + 2BB^*)J_1(z)^2 - ((A^2 + B^2)e^{2i\omega t} + cc)h_2(z)] \end{aligned} \quad (5.12)$$

where $*$ denotes the complex conjugate and the functions $h_1(z)$ and $h_2(z)$ are defined as follows:

$$\begin{aligned} h_1(z) &= J_1(z)^2 - J_2(z)J_0(z) - J_1(z_0)^2 \\ h_2(z) &= 2z^2(J_0(z)^2 + J_1(z)^2) - J_1(z)^2 - 2zJ_1(z)J_0(z) - z^2J_1(z_0)^2. \end{aligned}$$

Finally, we proceed to investigate the third-order equations in ϵ . The third-order equations are found to be given by

$$\begin{aligned}
\frac{\partial v_3}{\partial t} - g s \frac{\partial \phi_3}{\partial s} - g \phi_3 &= \frac{Y_0}{2L} (s \lambda^2 + g) (i e^{i \lambda t} + c.c) \\
- \frac{\partial v_1}{\partial \tau} - \frac{\partial \phi_1}{\partial t} (u_2 + \theta_1 w_1) + \frac{T_2}{m} \frac{\partial \phi_1}{\partial s} - g s \frac{\theta_1^2}{2} \frac{\partial \phi_1}{\partial s} - g \frac{\phi_1^3}{6} & \quad (5.13) \\
\frac{\partial w_3}{\partial t} + g s \frac{\partial \theta_3}{\partial s} + g \theta_3 &= \\
- \frac{\partial w_1}{\partial \tau} + u_2 \frac{\partial \theta_1}{\partial t} + \theta_1 v_1 \frac{\partial \phi_1}{\partial t} - \frac{T_2}{m} \frac{\partial \theta_1}{\partial s} + g \left(\frac{\theta_1^3}{6} + \frac{\theta_1 \phi_1^2}{2} \right) & \\
\frac{\partial \phi_3}{\partial t} - \frac{\partial v_3}{\partial s} &= - \frac{\partial \phi_1}{\partial \tau} + \frac{\theta_1^2}{2} \frac{\partial \phi_1}{\partial t} + \frac{\partial \phi_1}{\partial s} (u_2 + \theta_1 w_1) \\
\frac{\partial \theta_3}{\partial s} + \frac{\partial w_3}{\partial s} &= - \frac{\partial \theta_1}{\partial \tau} + u_2 \frac{\partial \theta_1}{\partial s} + \theta_1 v_1 \frac{\partial \phi_1}{\partial s}
\end{aligned}$$

The expressions given by (5.6), (5.8), and (5.12) are introduced into (5.13) and the spatial dependence is eliminated using a Galerkin procedure in which the resulting equations are multiplied by the zeroth order Bessel function, corresponding to the nearest natural frequency, and then integrating along the chain length. Finally, the secular terms are removed from the resulting equations by imposing the following conditions:

$$\begin{aligned}
\frac{1}{\omega} \frac{dA_1}{d\tau} &= -[f_1(\sigma + 1)^2 + f_2] e^{i\sigma\tau} + i[\gamma_0 A_1^2 A_1^* + \gamma_1 B_1^2 A_1^*] \\
\frac{1}{\omega} \frac{dB_1}{d\tau} &= i[\gamma_0 B_1^2 B_1^* + \gamma_2 A_1^2 B_1^* + \gamma_3 A_1 A_1^* B_1].
\end{aligned} \quad (5.14)$$

Here the following definitions are used:

$$\begin{aligned}
f_1 &= \frac{Y_0 \alpha_2}{4 \alpha_1 L} \\
f_2 &= \frac{Y_0 \alpha_0}{\alpha_1 L} \\
\gamma_0 &= \frac{\alpha_3}{2 \alpha_1} \\
\gamma_1 &= \frac{\alpha_4}{2 \alpha_1} \\
\gamma_2 &= \frac{\alpha_5}{2 \alpha_1} \\
\gamma_3 &= \frac{\alpha_6}{2 \alpha_1}
\end{aligned}$$

where

$$\begin{aligned}
\alpha_0 &= \int_0^{z_0} z J_0(z) dz \\
\alpha_1 &= \int_0^{z_0} z J_0(z)^2 dz \\
\alpha_2 &= \int_0^{z_0} z^3 J_0(z) dz \\
\alpha_3 &= \int_0^{z_0} z J_0(z) h_3(z) dz \\
\alpha_4 &= \int_0^{z_0} \frac{J_0(z)}{z} [h_2(z) J_2(z) + J_2(z) J_1(z)^2 - z h_1(z) J_1(z) - 2 J_0(z) J_1(z)^2] dz \\
\alpha_5 &= \int_0^{z_0} \frac{J_0(z)}{z^2} [z h_2(z) J_2(z) - 2 J_1(z)^3 - z^2 h_1(z) J_1(z) - 2 z J_0(z) J_1(z)^2] dz \\
\alpha_6 &= \int_0^{z_0} \frac{J_0(z)}{z^2} [4 z J_0(z) J_1(z)^2 - 4 J_1(z)^3 - 2 z J_1(z)^2 J_2(z)] dz \\
h_3(z) &= -\left[\frac{J_1(z) h_1(z)}{z} + (2 J_1(z)^2 - h_2(z)) \frac{J_2(z)}{z^2} + \frac{2 J_1(z)^3}{z^3} \right].
\end{aligned}$$

Note that the amplitude of excitation Y_0 is incorporated in the terms f_1 and f_2 and the excitation frequency is expressed in terms of the detuning σ , where

$$\sigma = \left(\frac{\lambda}{\omega} - 1 \right). \quad (5.15)$$

The amplitudes are further decomposed as follows:

$$\begin{aligned}
A_1(\tau) &= a(\tau) e^{i\epsilon_1(\tau)} \\
B_1(\tau) &= b(\tau) e^{im(\tau)}.
\end{aligned} \quad (5.16)$$

Substitution of these expressions into (5.14) and grouping real and imaginary terms yields:

$$\begin{aligned}
\frac{1}{\omega} \frac{dp}{d\tau} &= q[\sigma - \gamma_0(q^2 + p^2) - \gamma_1(s^2 - r^2)] - 2\gamma_1 p r s \\
\frac{1}{\omega} \frac{dq}{d\tau} &= -[f_1(\sigma + 1)^2 + f_2] - p[\sigma - \gamma_0(q^2 + p^2) + \gamma_1(s^2 - r^2)] + 2\gamma_1 q r s \\
\frac{1}{\omega} \frac{dr}{d\tau} &= s[\sigma - \gamma_0(r^2 + s^2) - \gamma_2(q^2 - p^2) - \gamma_3(p^2 + q^2)] - 2\gamma_2 p q r \\
\frac{1}{\omega} \frac{ds}{d\tau} &= -r[\sigma - \gamma_0(r^2 + s^2) + \gamma_2(q^2 - p^2) - \gamma_3(p^2 + q^2)] - 2\gamma_2 p q s.
\end{aligned} \quad (5.17)$$

Note that following Miles [42], the phase angles have been removed by setting

$$p = a(\tau)\sin(\xi) \quad (5.18)$$

$$q = a(\tau)\cos(\xi)$$

$$r = b(\tau)\sin(\eta)$$

$$s = b(\tau)\cos(\eta)$$

where $\xi = \sigma\tau - \xi_1$ and $\eta = \sigma\tau - \eta_1$.

Steady state solutions are given by the fixed points of (5.17). Setting the time derivatives equal to zero, two classes of fixed points are determined. The first class corresponds to a 2-D response, where

$$p = \pm a \quad (5.19)$$

$$q = r = s = 0. \quad (5.20)$$

From these fixed points, the 2-D solution is given by the following:

$$\sigma a \pm [f_1(\sigma + 1)^2 + f_2] - \gamma_0 a^3 = 0. \quad (5.21)$$

The second class of fixed points correspond to 3-D motions. The fixed points are given by

$$p = \pm a \quad (5.22)$$

$$q = 0$$

$$r = \pm b \cos\left(\frac{N\pi}{2}\right)$$

$$s = \pm b \sin\left(\frac{N\pi}{2}\right).$$

Substitution of these fixed points into (5.17) yields the following:

$$\begin{aligned}\sigma \pm \frac{[f_1(\sigma + 1)^2 + f_2]}{a} - \gamma_0 a^2 - \gamma_1 b^2 (-1)^N &= 0 \\ \sigma - \gamma_0 b^2 - \gamma_2 a^2 (-1)^N - \gamma_3 a^2 &= 0.\end{aligned}\tag{5.23}$$

The solutions given by (5.21) and (5.23) are used to generate response amplitude versus frequency (or detuning) curves for a fixed excitation amplitude. However, we must first determine if the corresponding solutions are stable, as discussed in the next section.

5.3.2 Stability Analysis

Stability of the solutions is determined by investigating the eigenvalues of the Jacobian matrix formed from (5.17). In general, the real part of all four eigenvalues must be less than zero for the solution to be stable to small perturbations [27]. Otherwise, small perturbations will not decay in time.

In the absence of damping, the Jacobian matrix for this problem has zeros along the main diagonal and is separable into two 2×2 matrices. As such, all eigenvalues occur in complex conjugate pairs. Therefore, the only solutions which do not grow exponentially in time are those in which the eigenvalues are purely imaginary. Generally, solutions with purely imaginary eigenvalues are considered neutrally stable and are sensitive to nonlinearities.

Incorporating a small degree of linear damping into the governing equations introduces negative terms along the main diagonal of the Jacobian matrix. The net effect is that all purely imaginary eigenvalues develop a negative real component. In other words, all neutrally stable centers become stable spirals or stable nodes, depending on the amount of damping. This finding is demonstrated in figure 5.2 in which the eigenvalues near a saddle-node bifurcation are shown with and without damping. As a result, for this analysis all solutions with purely imaginary eigenvalues will also be considered as stable.

5.3.3 Results

Analytic results, for detuning values near the second natural frequency, are presented for an excitation amplitude of 0.0087L. Figures 5.3 and 5.4 show the in-plane and out-of-plane

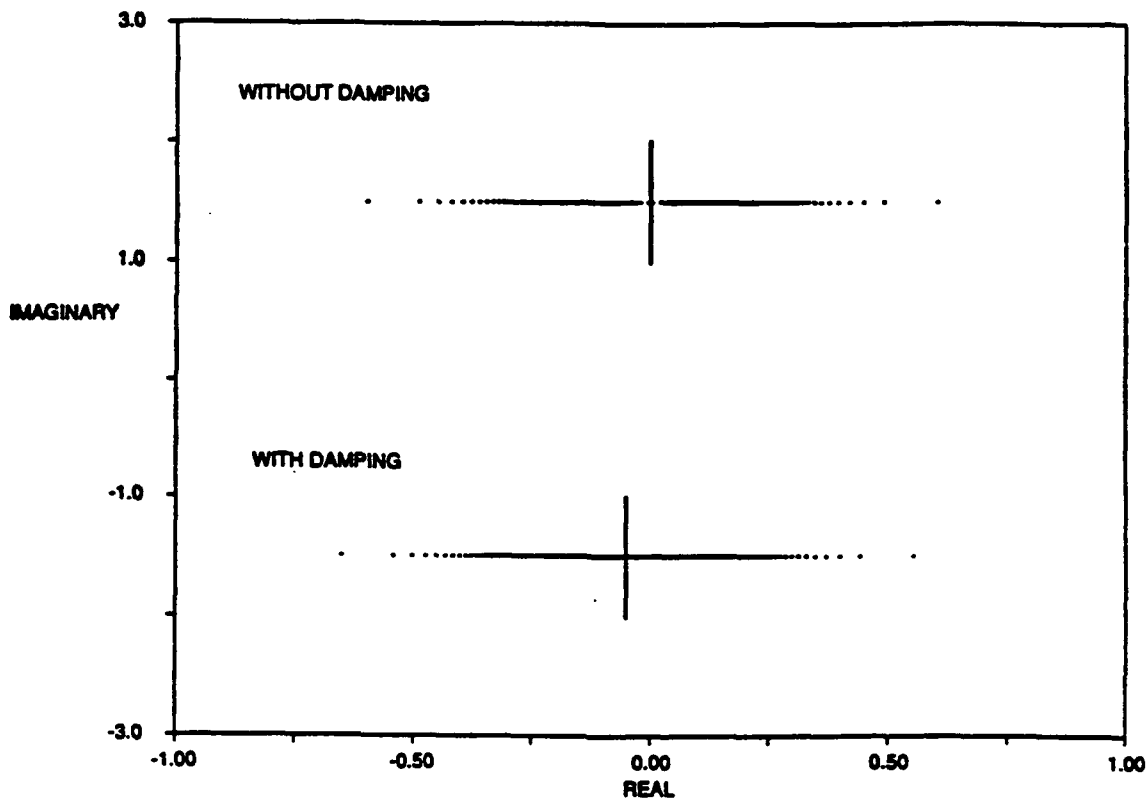


Figure 5.2: Effect of linear damping on eigenvalues near a saddle-node bifurcation.

velocities, respectively, at the free end of the chain. The velocities are nondimensionalized by \sqrt{gL} , which is directly proportional to ωL . Note that for clarity, only one branch of the two-dimensional solution is shown in figure 5.4.

As shown, several bifurcations, labeled from A to D, were found to occur. The bifurcations at A and B are saddle-node bifurcations, while a pitchfork bifurcation occurs at D. At C, the stability of the three-dimensional branch changes suddenly for increasing detuning values. The variation of the eigenvalues along the associated three-dimensional branch is shown in figure 5.5. Based on the variation of the eigenvalues, the stability transition at C is identified as a Hamiltonian-Hopf bifurcation. This class of bifurcation has been identified by other researchers in the past (see for example [75]).

As a result of the bifurcations that occur, a region develops in which no stable response is predicted. For the example shown, this region lies between $-0.08 \leq \sigma \leq -0.035$. The dynamics within this region were investigated through numerical and experimental means,

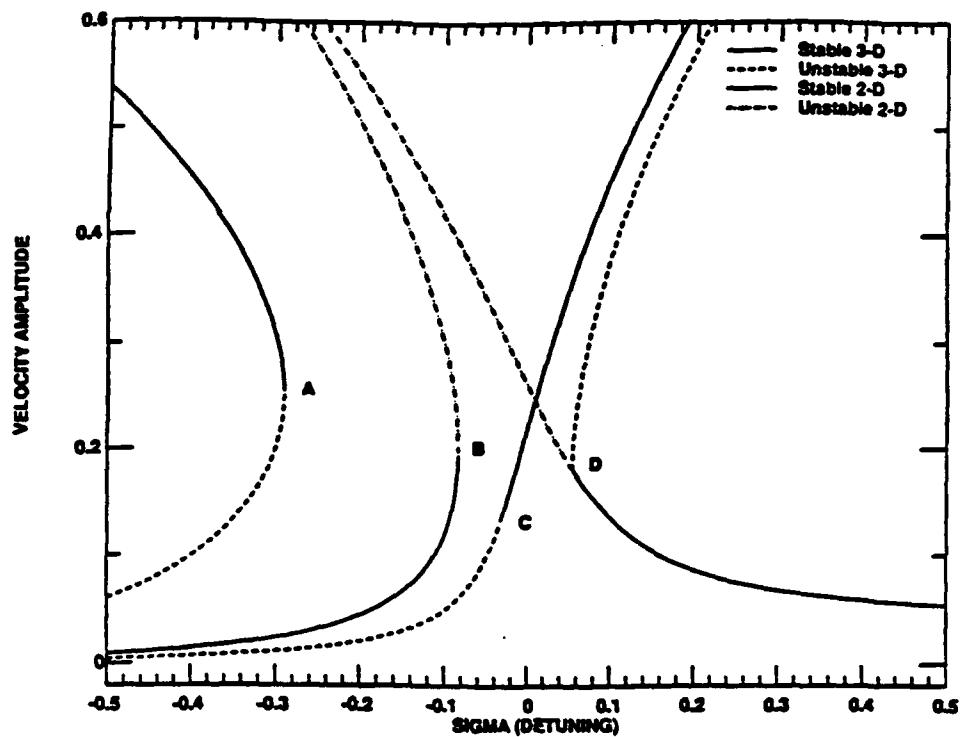


Figure 5.3: Stability curves: In-plane velocity at lower end versus detuning for excitation amplitude $Y_0 = 0.0087L$, near the second natural frequency.

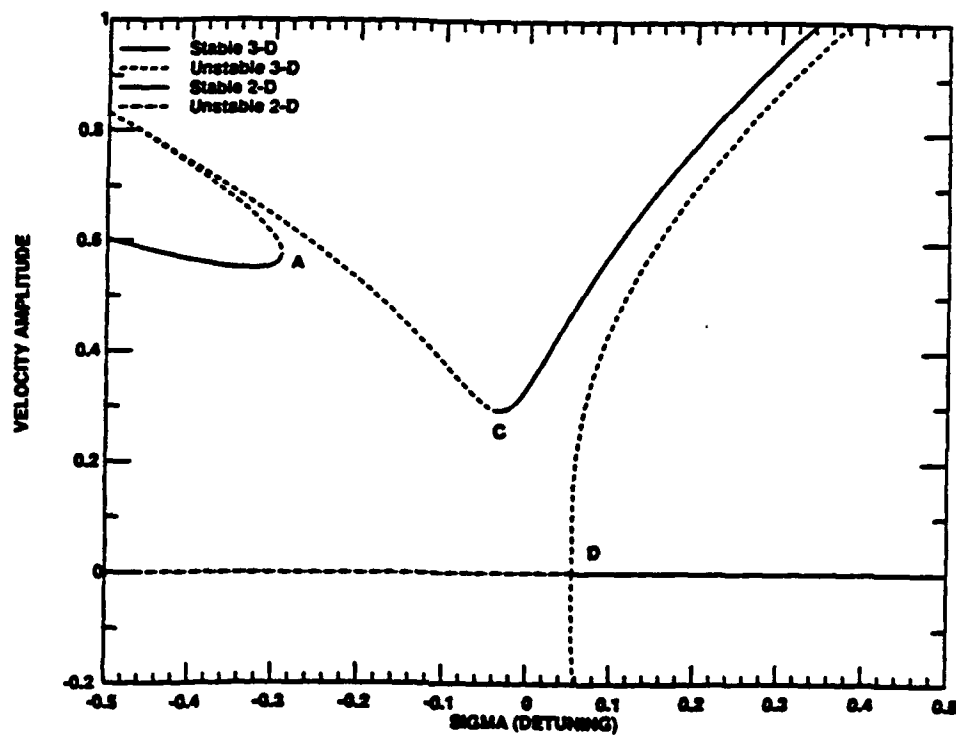


Figure 5.4: Stability curves: Out-of-plane velocity at lower end versus detuning for excitation amplitude $Y_0 = 0.0087L$, near the second natural frequency.

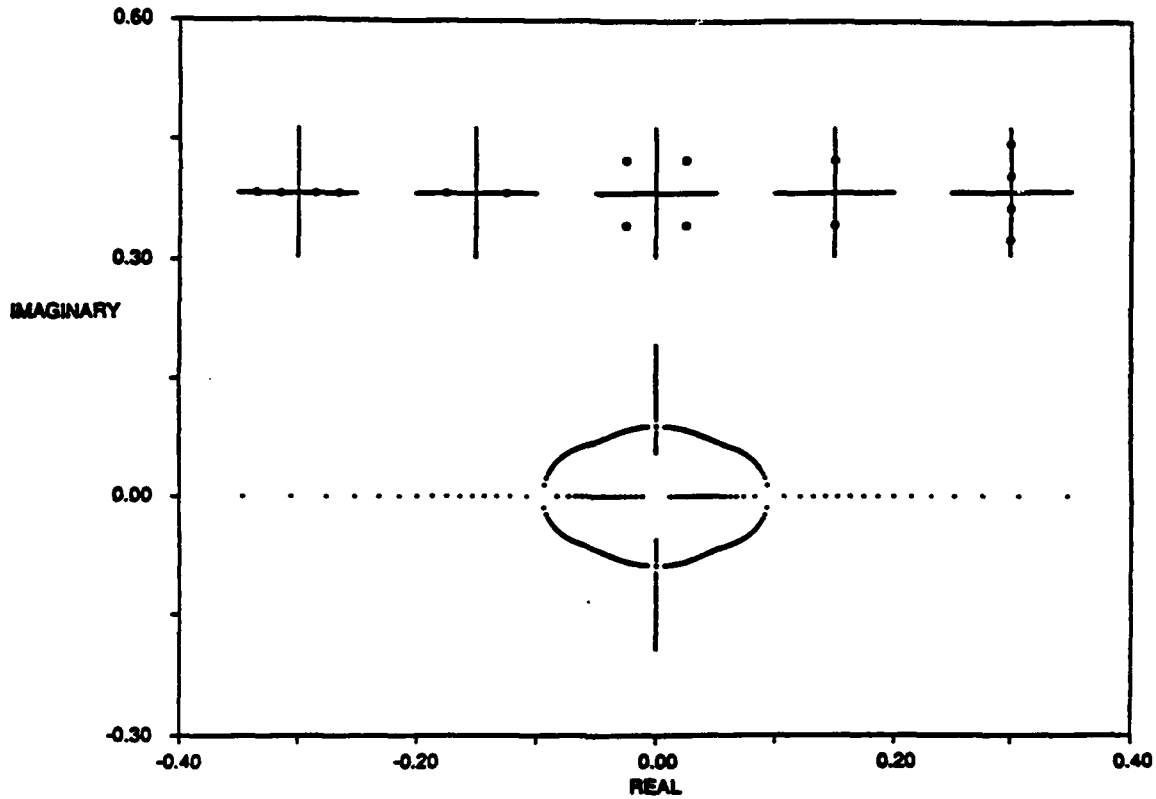


Figure 5.5: Hamiltonian-Hopf bifurcation: Variation of eigenvalues along 3-D branch.

as discussed later in this chapter.

As the excitation amplitude is increased, the unstable region increases and shifts to a lower frequency range. This is demonstrated in figure 5.6, in which the excitation amplitude is shown versus the unstable frequency region. As one would expect, the size of the region vanishes as the excitation amplitude approaches zero.

5.4 Numerical Solution

The purpose of the numerical analysis was twofold. First, verification of the stable response regions determined analytically was sought. By solving the fully nonlinear equations, the effect of higher-order correction terms beyond ϵ^3 could be determined. Secondly, the numerical approach provides a means with which to verify the existence of the unstable response region and investigate the dynamics within the region.

The second-order implicit finite difference approximation scheme described in chapter 3

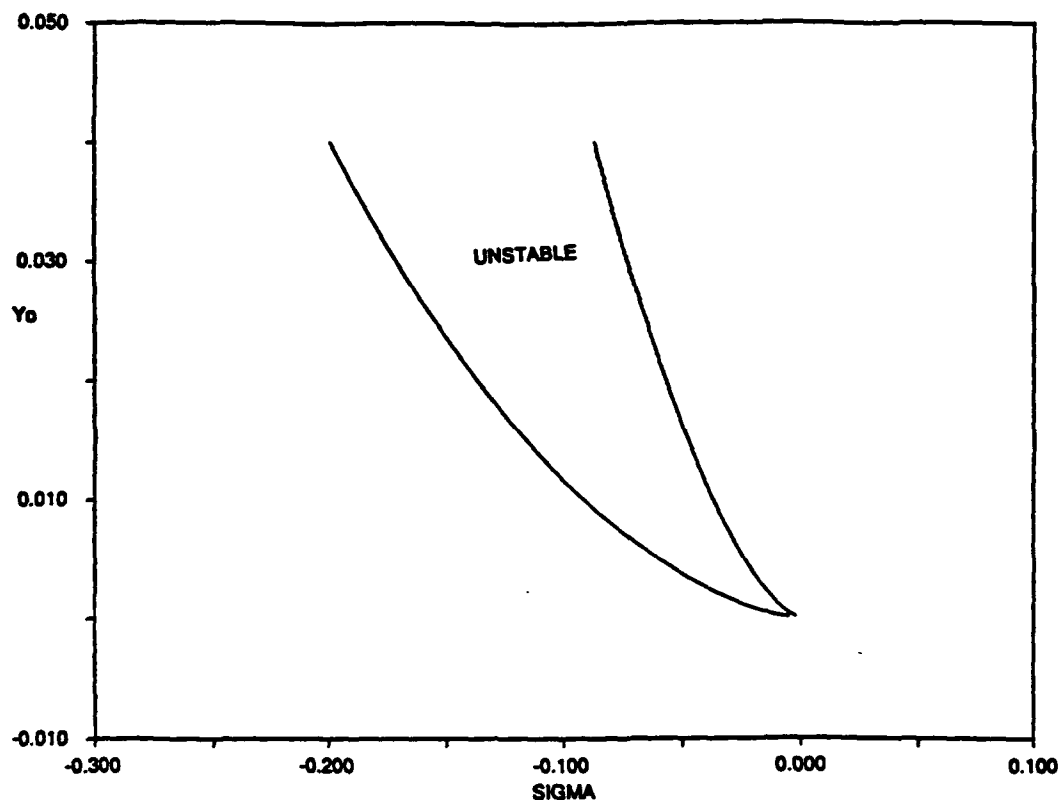


Figure 5.6: Bifurcation diagram: Excitation amplitude versus frequency region in which all stationary solutions are predicted to be unstable.

was applied to the set of equations given by (5.1). For simulations involving moderately large excitation amplitudes the tension remains finite; however, for larger excitation amplitudes, as discussed in section 5.6, the tension does vanish and a small amount of bending stiffness was incorporated for stability.

Numerical studies were first conducted for detuning values at which the analytic technique predicted a stable response. As shown in figure 5.7, good agreement was obtained between the analytical and numerical solutions. Both the character of the response, i.e. stable 2-D or 3-D, and the magnitude compared favorably. It should be noted that a small amount of linear damping, corresponding to less than 1 percent critical, was incorporated to eliminate starting transients.

A numerical analysis of the unstable region ($-0.08 \leq \sigma \leq -0.035$) was also conducted and results are presented for $\sigma = -0.06$ and -0.05 . Figure 5.8 shows the time series records for the in-plane and out-of-plane transverse velocities at the free end of the chain for σ

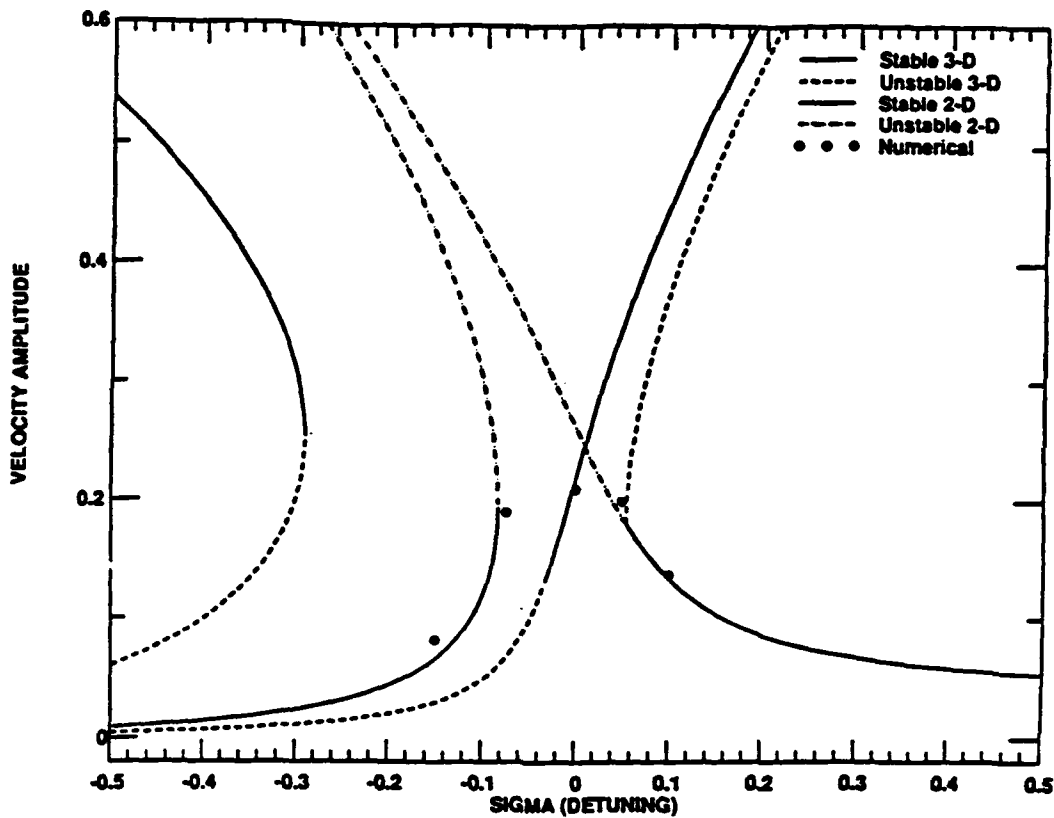


Figure 5.7: Numerical results (circles) compared with perturbation results (lines): In-plane velocity at lower end for excitation amplitude $Y_0 = 0.0087L$.

$= -0.06$. The response is characterized by slightly irregular beating, despite the fact that sufficient time has elapsed to eliminate starting transients. The power spectrum for the in-plane response (figure 5.9) shows a widening of the frequency content around the frequency of excitation. Further insight into the nature of the response is provided by constructing a Poincare plot (figure 5.10) [5]. As shown, at this excitation frequency the beating motion is only slightly irregular and the response is close to quasi-periodic.

Time series records for the detuning value $\sigma = -0.05$, which lies further inside the unstable response region, are shown in figure 5.11. As shown, the response is characterized by irregular beating and the associated power spectra (figure 5.12) also demonstrates a widening of the spectrum near the excitation frequency. The Poincare plot (figure 5.13) exhibits a much more detailed structure than for the previous case.

Simulations were also conducted in which, after the starting transients had decayed, damping was removed using a linear ramping function. Steady state solutions were found

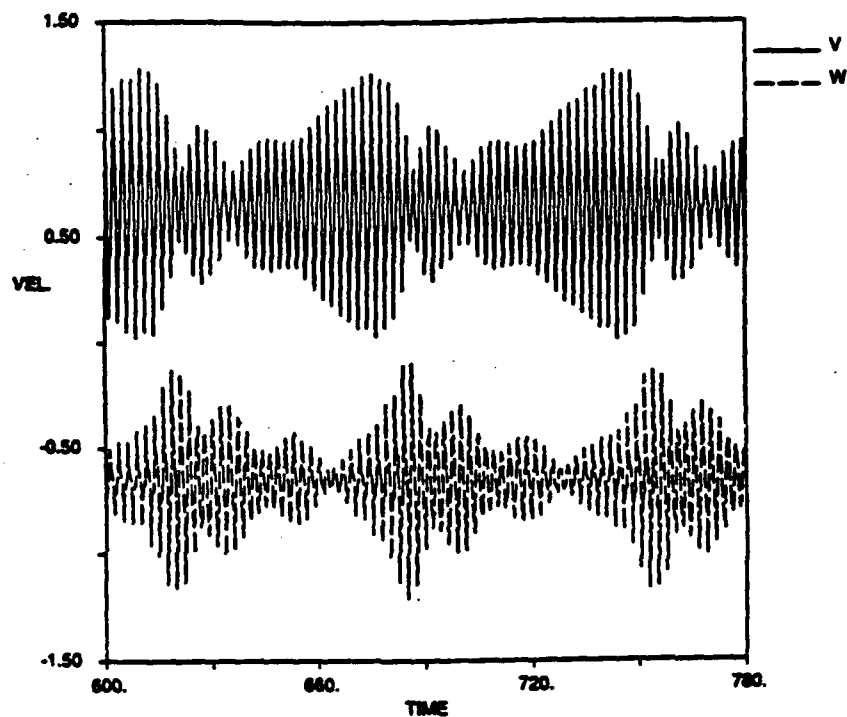


Figure 5.8: Numerical results: Time series record for in-plane and out-of-plane velocities at free end, with excitation amplitude $Y_0 = 0.0087L$ and detuning $\sigma = -0.06$

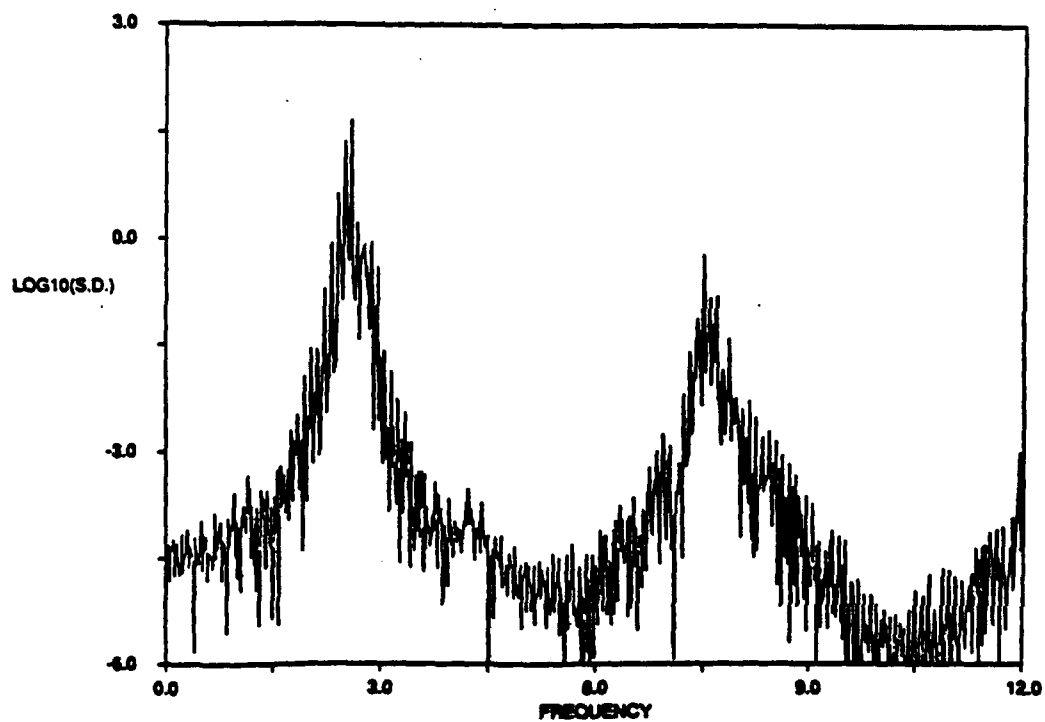


Figure 5.9: Power spectrum of in-plane velocity shown in 5.8.

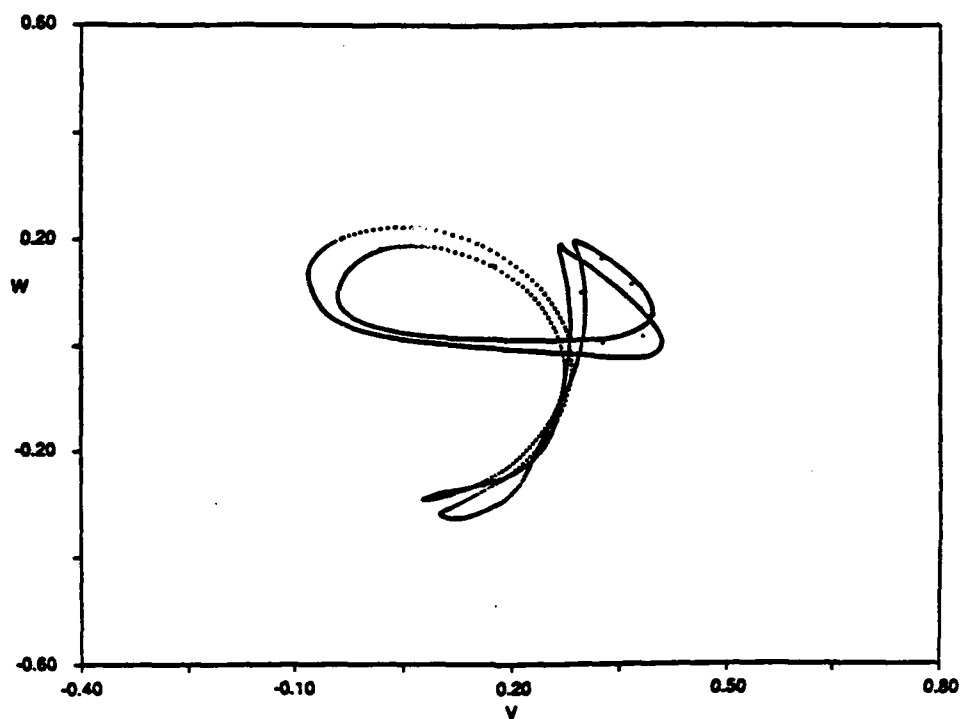


Figure 5.10: Poincare plot of in-plane velocity shown in 5.8.

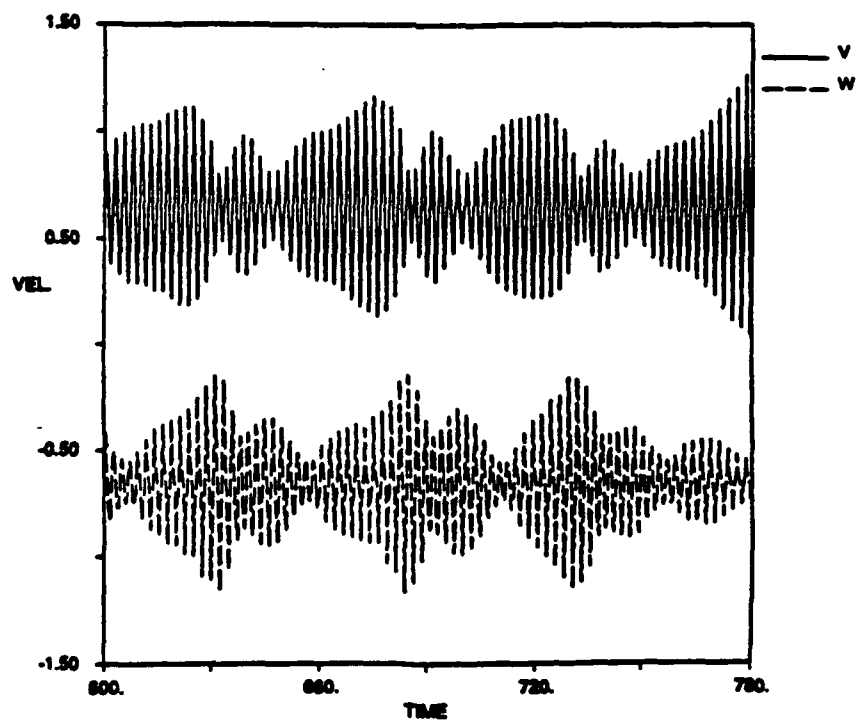


Figure 5.11: Numerical results: Time series record for in-plane and out-of-plane velocities at free end, with excitation amplitude $Y_0 = 0.0087L$ and detuning $\sigma = -0.05$

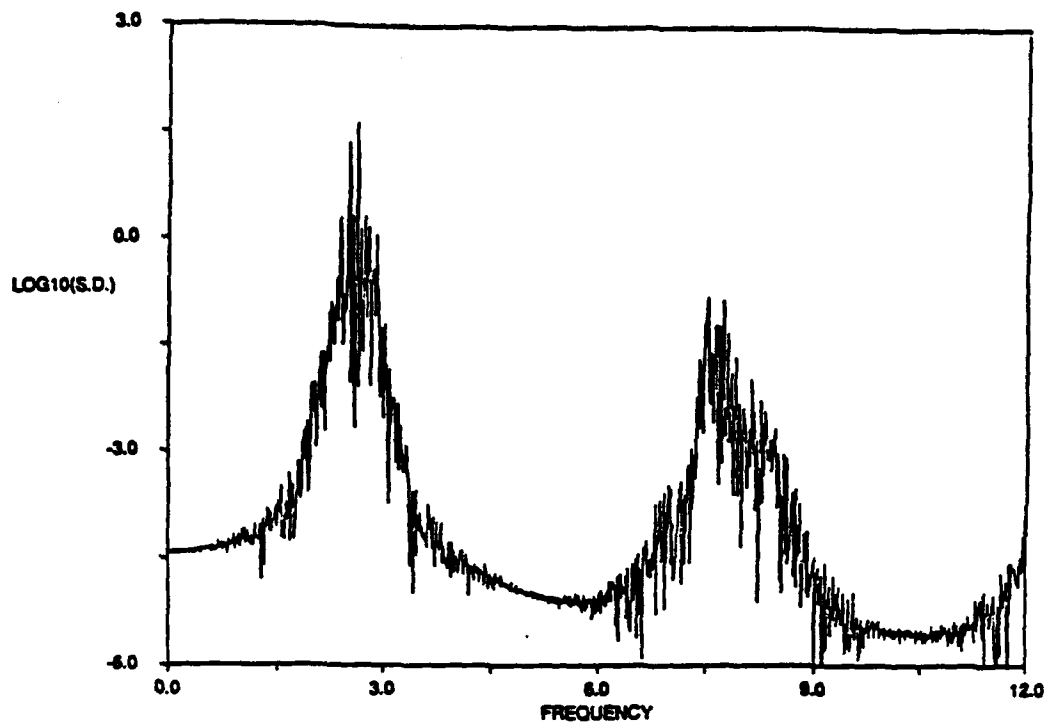


Figure 5.12: Power spectrum of in-plane velocity shown in 5.11.

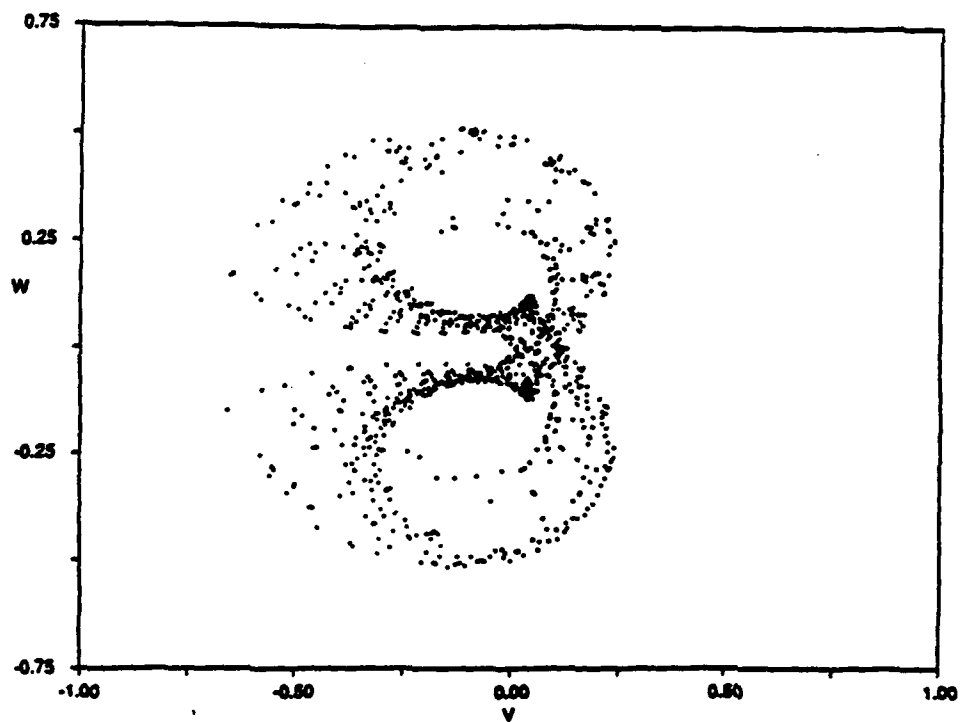


Figure 5.13: Poincare plot of in-plane velocity shown in 5.11.

to be only slightly affected. However, for simulations within the unstable frequency region, the chain was found to lose tension and collapse. This prevented obtaining long time series records, as required for Poincare plots. This topic is addressed further in section 5.6.

5.5 Experimental Study

Experiments were conducted to verify the analytic and numerical results. The relative simplicity of the physical problem under study allowed for a simple experimental setup. However, the analytic results show a sensitive dependence on the excitation frequency and amplitude, therefore, strict control was maintained over these two input parameters.

5.5.1 Experimental setup

Experiments were conducted at the MIT Ocean Engineering Testing Facility. A 1.75 meter chain was selected, having its second natural frequency at 1.04 hertz. Excitation of the chain was accomplished by a LINTECH leadscrew positioning table, with a travel of ± 8.5 centimeters, driven by a microprocessor-controlled SEIBERCO AIM-3400 closed-loop digital servomotor. The tracking signal input to the servo controller (corresponding to the desired motion at the top of the chain) was calculated in real time, by a NEC Powermate 1 286-class computer, from an initial user specified set of parameters and generated with the help of an onboard METRABYTE DASH-16 12 bit D/A converter. An analysis of the system determined that errors in the excitation frequency and amplitude were maintained below 1 and 5 percent, respectively. An overview of the experimental setup is shown in figure 5.14..

Several points along the chain were illuminated, using cotton balls soaked in a light emitting fluid, and their in-plane and out-of-plane displacements recorded on video tape using two separate PANASONIC PV160 video cameras. Displacement time series records were then generated from the video data using a MOTION ANALYSIS VP110 motion analyzer, located at the Woods Hole Oceanographic Institute, which calculates the center of intensity and resulting motion of each light source on the chain.

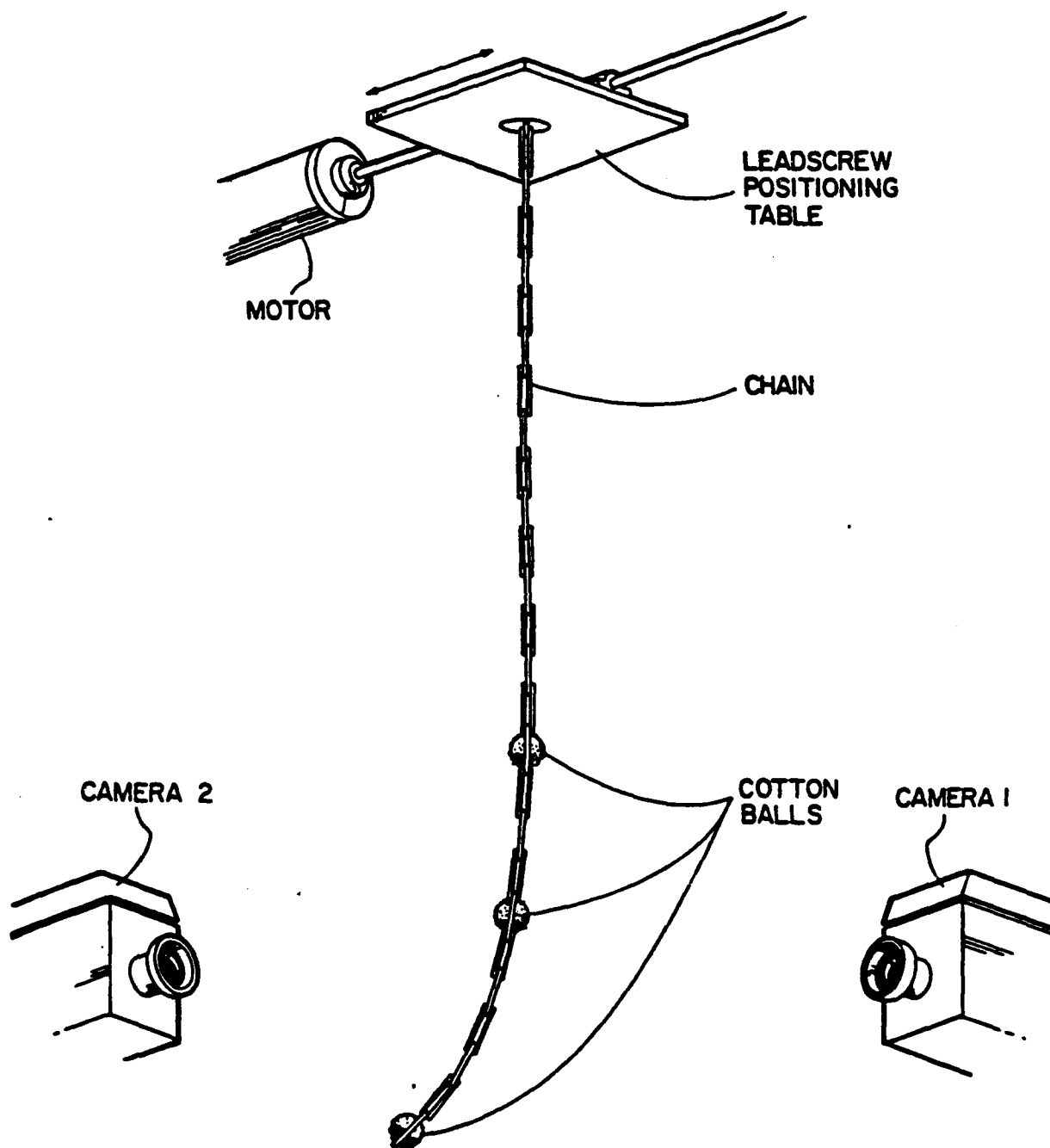


Figure 5.14: Experimental setup.

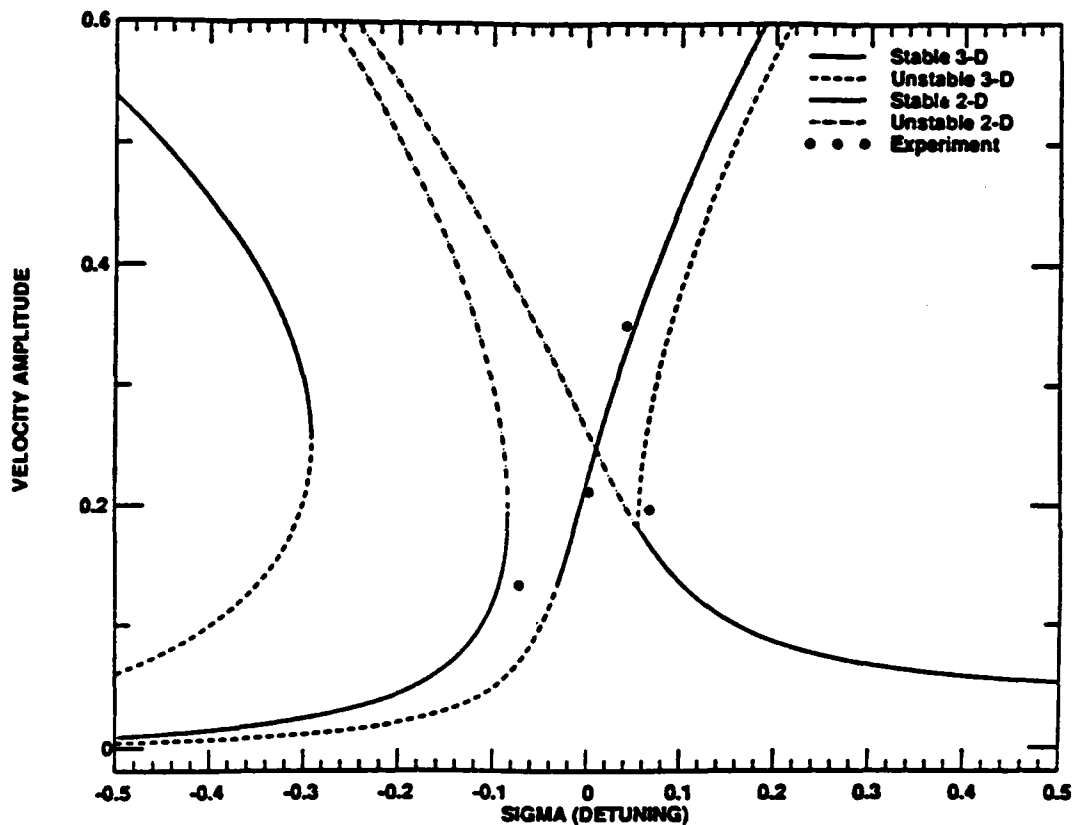


Figure 5.15: Experimental results (circles) compared with perturbation results (lines): In-plane velocity at lower end for excitation amplitude $Y_0 = 0.0087L$.

5.5.2 Experimental Data

A number of experimental runs were conducted for detuning values at which a stable response was predicted analytically. Good agreement was obtained between methods, as shown in figure 5.15. The character of the response, as well as the amplitude, matched favorably and the results proved stable to perturbations.

Based on preliminary experimental runs, the frequency region characterized by irregular response appeared to be shifted to slightly higher frequency values than predicted analytically. This trend is apparent in figure 5.15. Overall, however, the shift in frequency was found to be less than 2 percent.

Time series records, presented in figures 5.16 and 5.17, show the experimentally obtained in-plane and out-of-plane velocities at the free-end for detuning values of -0.028 and -0.047, respectively. As shown, the response is irregular, despite ramping the excitation amplitude

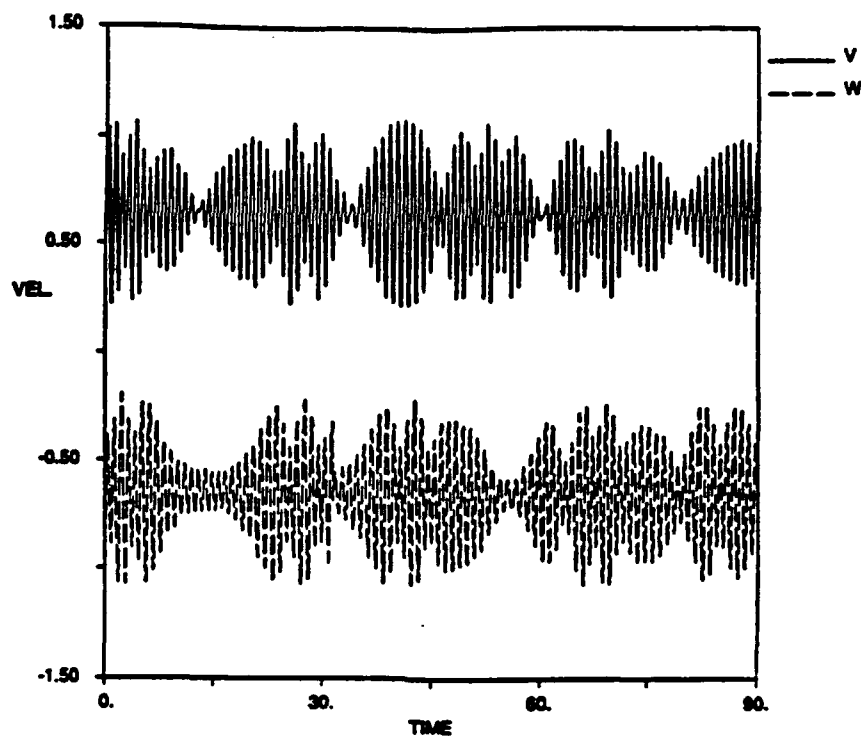


Figure 5.16: Experimental results: Time series record for in-plane and out-of-plane velocities at free end, with excitation amplitude $Y_0 = 0.0087L$ and detuning $\sigma = -0.028$

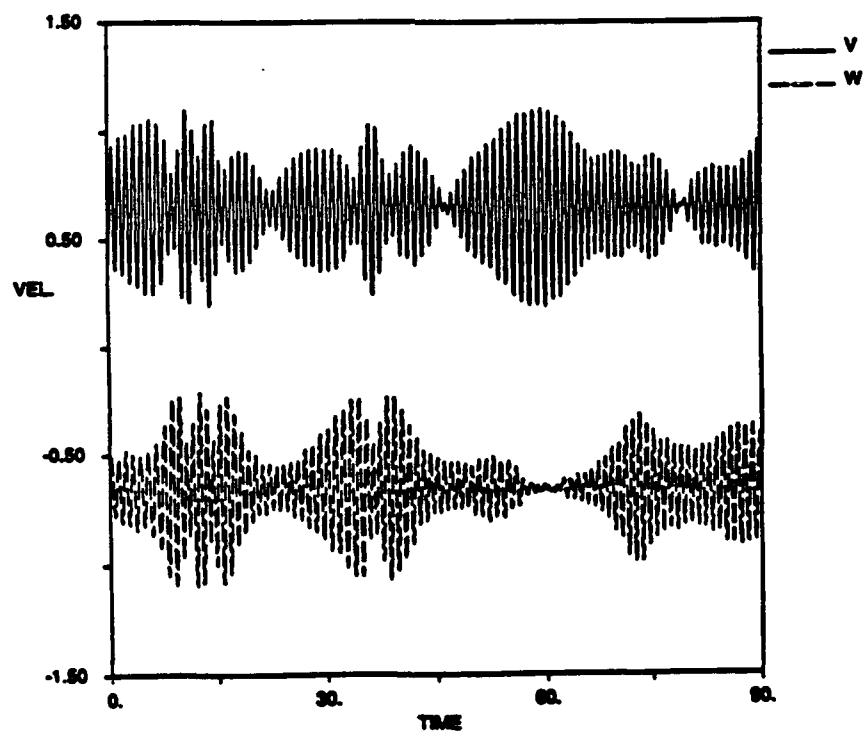


Figure 5.17: Experimental results: Time series record for in-plane and out-of-plane velocities at free end, with excitation amplitude $Y_0 = 0.0087L$ and detuning $\sigma = -0.047$

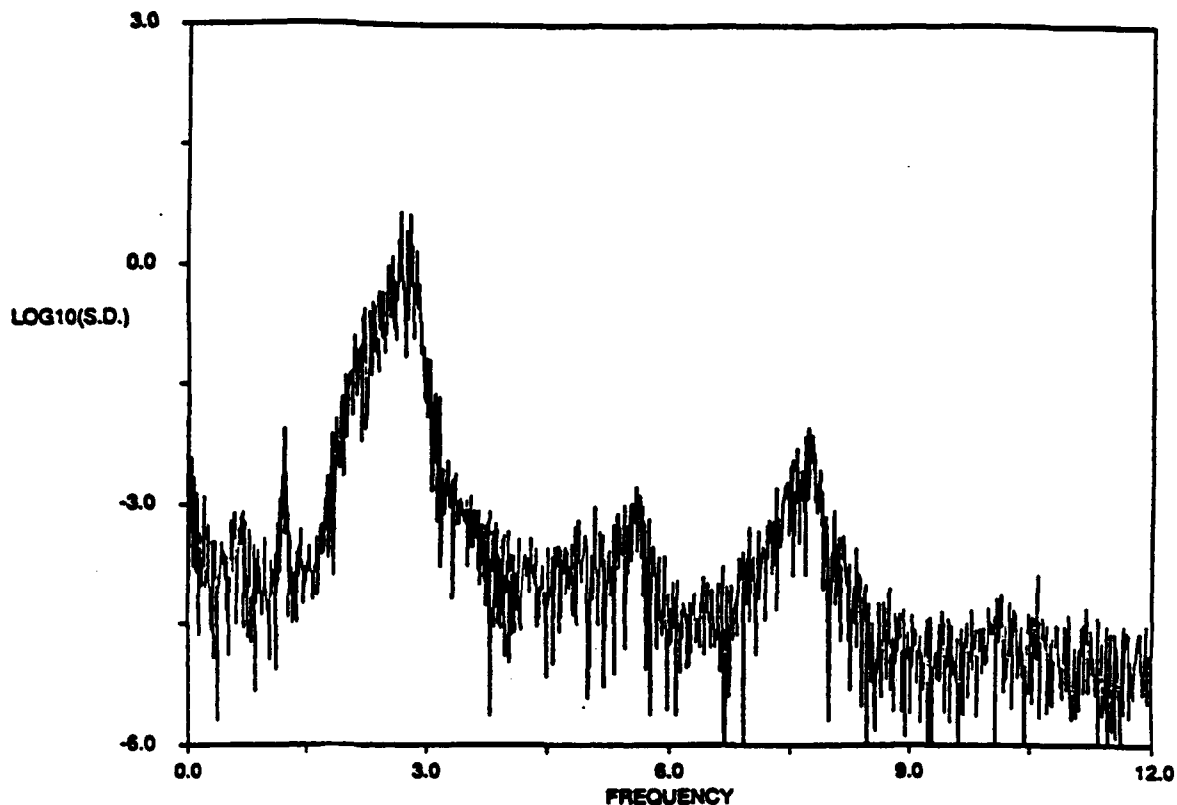


Figure 5.18: Power spectrum of in-plane velocity shown in 5.16.

up to the desired value and allowing sufficient time for starting transients to decay. The associated power spectra (figures 5.18 and 5.19) show a marked widening of the spectrum, around the excitation frequency. This is in contrast to the narrow banded spectra obtained at other excitation frequencies.

5.6 Response to Large Amplitude Excitation

In this section we investigate the response of the chain to excitation amplitudes in excess of those studied previously. Much of the work detailed here is summarized in a paper by Howell [23].

As discussed earlier the asymptotic analysis results predict that increased excitation amplitude widens the frequency region in which all steady state solutions are determined to be unstable. Therefore it is logical to investigate unsteady solutions for larger excitation amplitudes. However, the numerical scheme was found to encounter stability problems when bending stiffness was neglected. In addition, solutions within the unstable frequency range were found to be unobtainable numerically when damping was removed. To understand why

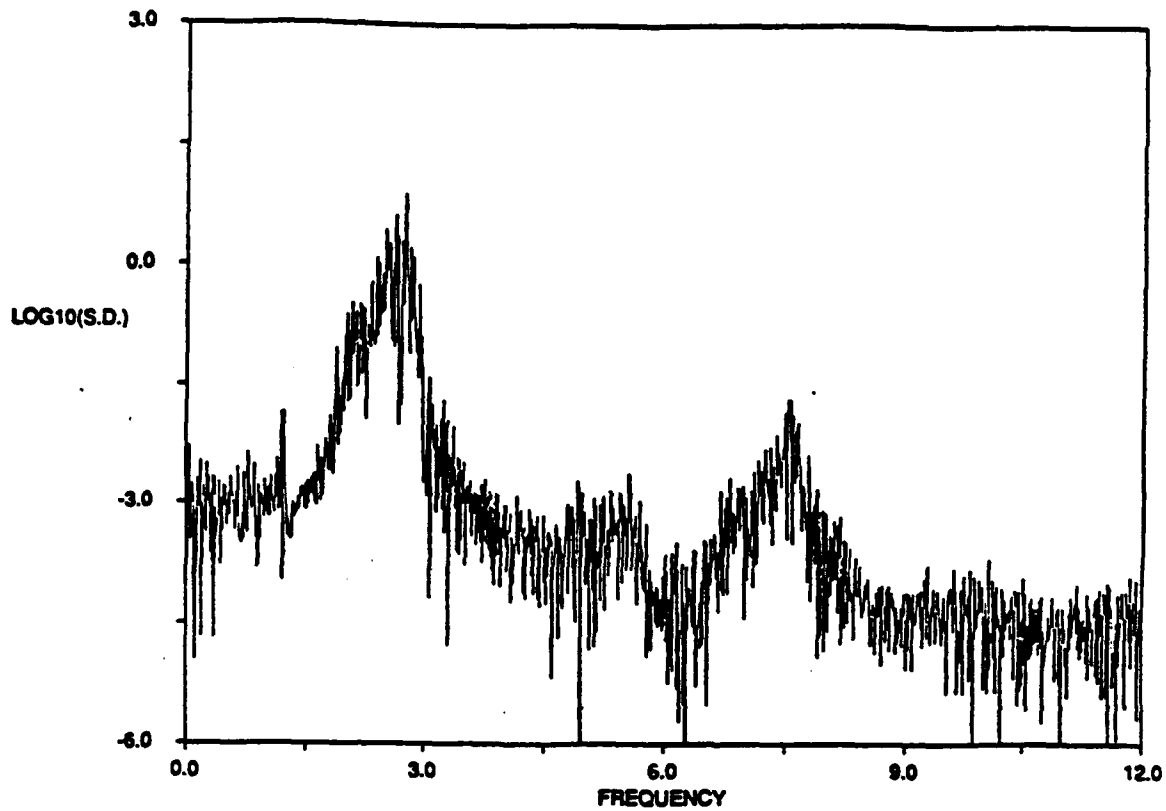


Figure 5.19: Power spectrum of in-plane velocity shown in 5.17.

this occurs, we further investigate the perturbation results to determine if it is possible for the dynamic tension to cancel the static tension, thereby causing the chain to lose tension over a portion of its length. Here we simplify the analysis by concentrating on the region near the lower boundary because that is the location where it is most likely that tension will be lost.

Using the previously obtained results we find that

$$\lim_{s \rightarrow 0} \frac{T_2(s, t) + mgs}{mgs} = \frac{a^2[1 \pm (3 - 4J_1(z_0)^2)] + 4}{4}.$$

Therefore, if we express the condition for negative tension values to occur in terms of the angle at the free-end we find

$$a > \sqrt{\frac{2}{1 - 2J_1(z_0)^2}} \quad (5.24)$$

In terms of solutions near the second natural frequency, this means the angle must exceed 1.61 radians for the tension to become negative. This corresponds to the free-end of

the cable slightly exceeding a horizontal orientation.

This analysis shows that, according to the perturbation technique, above a certain level of response amplitude, and near resonance, negative tension occurs near the free end. Since negative tensions cannot be sustained, the chain loses tension over a portion of its length. This leads to increased angles, eventually resulting in the chain collapsing.

Numerical and experimental tests were conducted at larger excitation amplitudes aimed at verifying the numerical model so that it could be used as a tool for studying the dynamics leading to the collapse of the chain. Results are presented herein for an excitation amplitude of $0.017L$ and a frequency of 1.5 hertz, corresponding to a detuning of 0.44. The excitation amplitude was ramped linearly in time over 2.0 seconds. This short ramping interval was chosen to simplify the analysis by not allowing sufficient time for exciting dynamics out-of-plane. A number of ramping intervals were investigated and quantitatively similar results were obtained in each case. Therefore, the ramping interval selected is not of importance.

Numerical studies were first conducted neglecting bending stiffness. Numerical results for the chain shape at several different time steps, prior to the loss of tension, are shown in figure 5.20. The lower one-fifth of the chain has been enlarged to show that only a small segment of the chain loses tension. After tension is lost, the numerical scheme becomes unstable and fails to converge.

As discussed previously, the cable equations are singular for zero tension if bending stiffness is neglected. There is an additional singularity, however, when the tension becomes zero which appears in the compatibility relations.

The compatibility relations derived in chapter 2 are based on spatial and temporal continuity of the position vector $\vec{r}(t, s)$.

Once tension is lost, however, there is no physical mechanism that enforces slope continuity in the line. It is possible for a perfectly flexible cable to form corners in its configuration. As a result the compatibility relations in differential form, as derived in chapter 2, are invalid once tension is lost and a new set of compatibility relations must be devised to preserve the chain length. One could also model the chain as a series of rigid links, however, this would require an inordinate number of degrees of freedom thereby significantly reducing the computational efficiency.

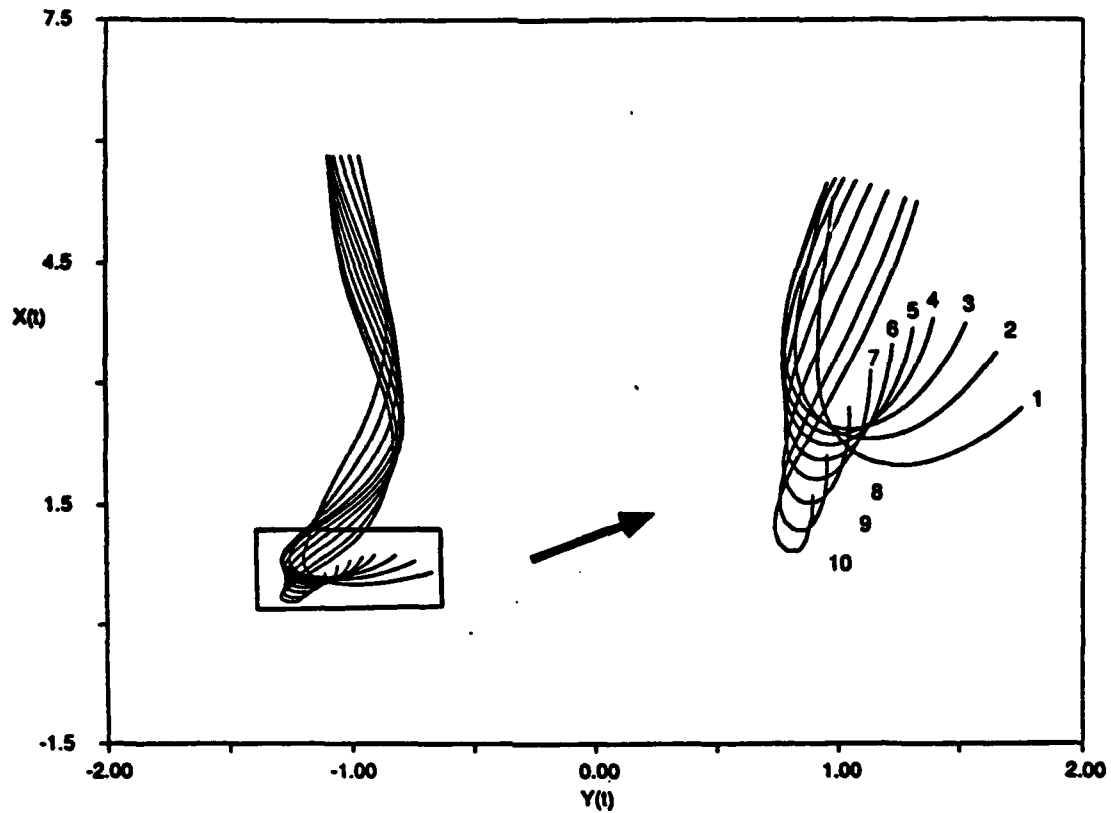


Figure 5.20: Numerical results: Chain configuration at several times prior to the collapse of the lower region. Segment in box enlarged on the right.

Both problems, i.e. the singularity in the equations of motion and the discontinuities in slope, are eliminated by incorporating bending stiffness. Bending stiffness smooths out discontinuities, as addressed in chapter 4, and provides a physical mechanism for energy propagation in the absence of tension. For cables bending stiffness is the actual physical mechanism that must be included for accurate modelling. For chains the link interaction is far more complex to model, so we treat the chain as a highly flexible cable by adopting a small value of bending stiffness as a mathematical fix of the singularities encountered. The numerical procedure for incorporating bending stiffness presented in chapter 3 was adopted for this analysis.

Numerical results after the chain has lost tension and collapsed were obtained using a nondimensional bending stiffness value of $EI/mgL^3 = EI^* = 10^{-6}$. Computations proceeded through the onset of zero tension, eventually determining one-half cycle later that, after tension has been restored, the chain intersects itself as shown in figure 5.21.

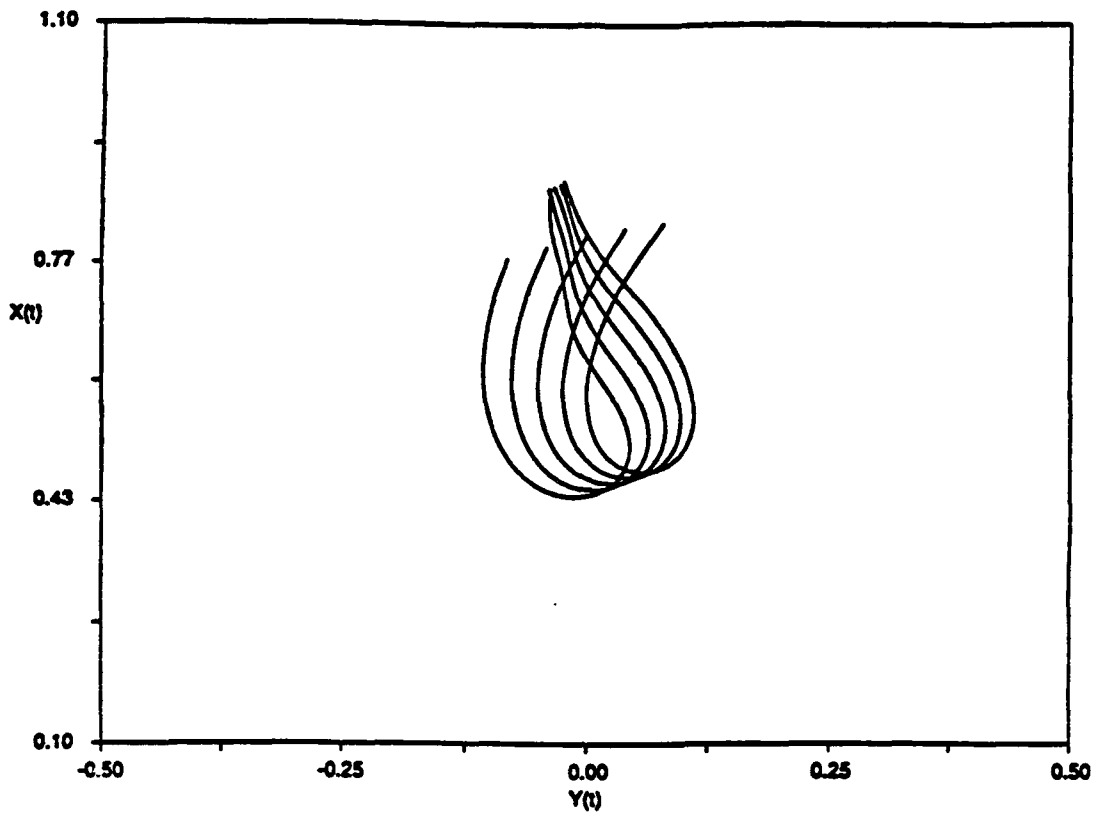


Figure 5.21: Numerical results: Predicted chain configuration as free-end intersects the chain.

To demonstrate that incorporating bending a small degree of bending stiffness eliminates the zero tension singularities, while not significantly altering the solution, figure 5.22 shows numerical results for two values of EI^* . As shown, similar results are obtained for an order of magnitude variation in flexural stiffness. Note that this is attributable to the magnitude of the bending stiffness incorporated.

Figures 5.23 through 5.26 show the numerically obtained time series records for the tension, tangential velocity, normal velocity, and angle, at four locations along the chain. Figure 5.23 clearly depicts the transition from low to high tension. Near the lower boundary, impulse-like tension peaks are exhibited, followed by periods in which the tension is nearly zero. These tension peaks result in rapid variations in velocity, as shown in figures 5.24 and 5.25. Further up the chain, the response remains regular and behaves like the response of a taut cable. In contrast, at the lower end the angle increases beyond the value of π , at which time an entire segment of the chain loses tension and collapses (figure 5.26).

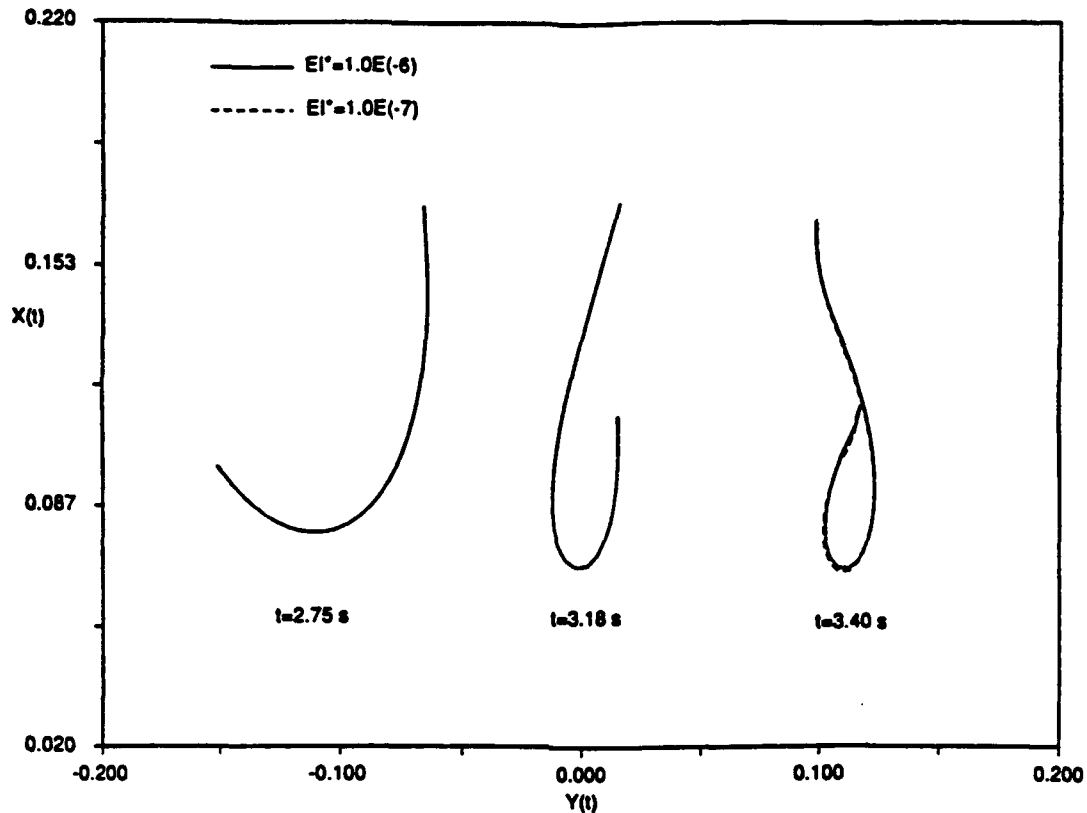


Figure 5.22: Comparison of simulation results for two values of EI^* .

The normal velocity along the chain is shown in figure 5.27 for four different times. As shown an energy wave is generated at the top which amplifies as it travels toward the free end. Steep gradients in velocity develop which in turn give rise to large angular accelerations. Eventually the angular momentum builds to where the tension is canceled and the angle increases beyond π .

The dynamic tension along the chain, obtained by removing the static tension from the total tension, is shown in figure 5.28 for the listed times. Figure 5.28 clearly demonstrates that low tension effects are confined to a region encompassing less than 10 percent of the total chain length, while the remaining chain exhibits a taut cable response.

Figures 5.29 and 5.30 compare experimental and numerical results for the chain displacement at three different times. The lower half of the chain is isolated in figure 5.29, while the lower one-eighth is shown in figure 5.30. Note that the numerical results were obtained using the small value of bending stiffness discussed previously. As readily seen the

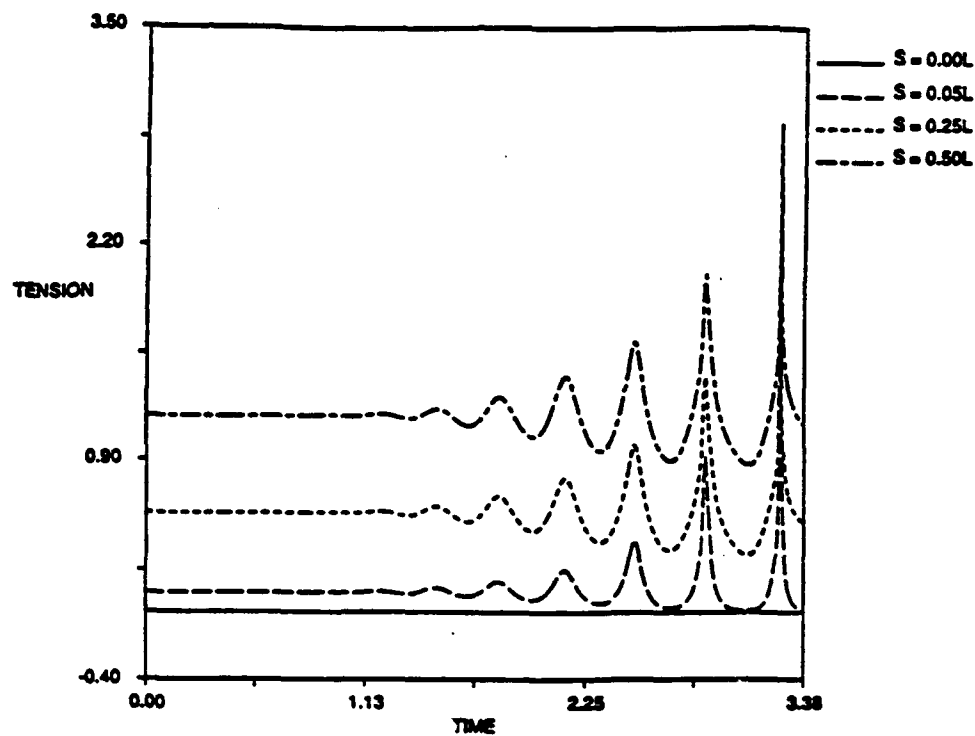


Figure 5.23: Numerical results: Total tension at four locations along the chain, for case under study.

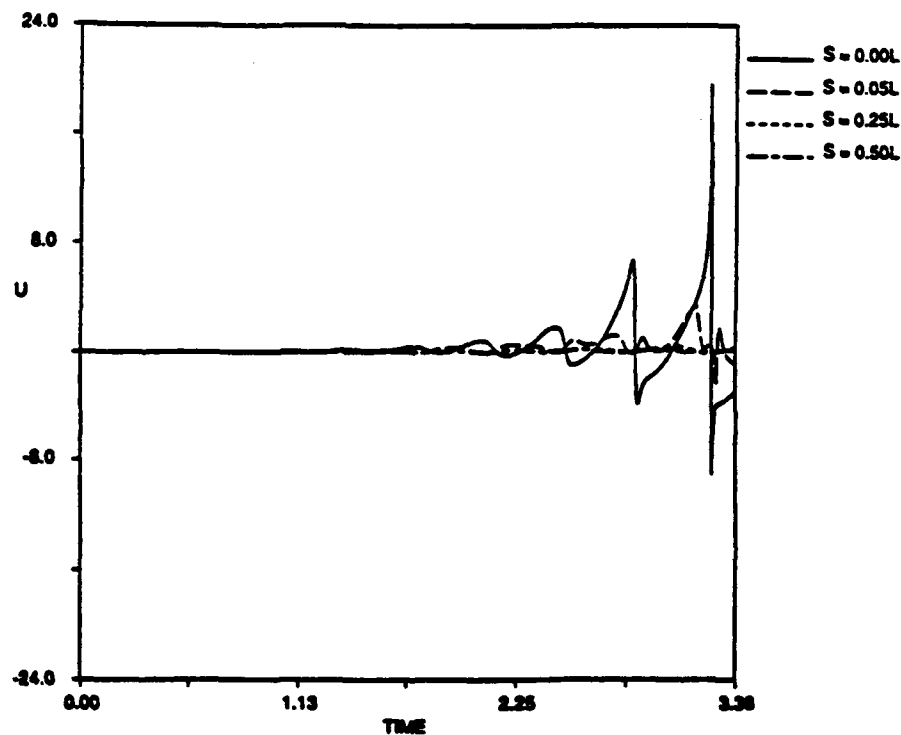


Figure 5.24: Numerical results: Tangential velocity at four locations along the chain, for case under study.

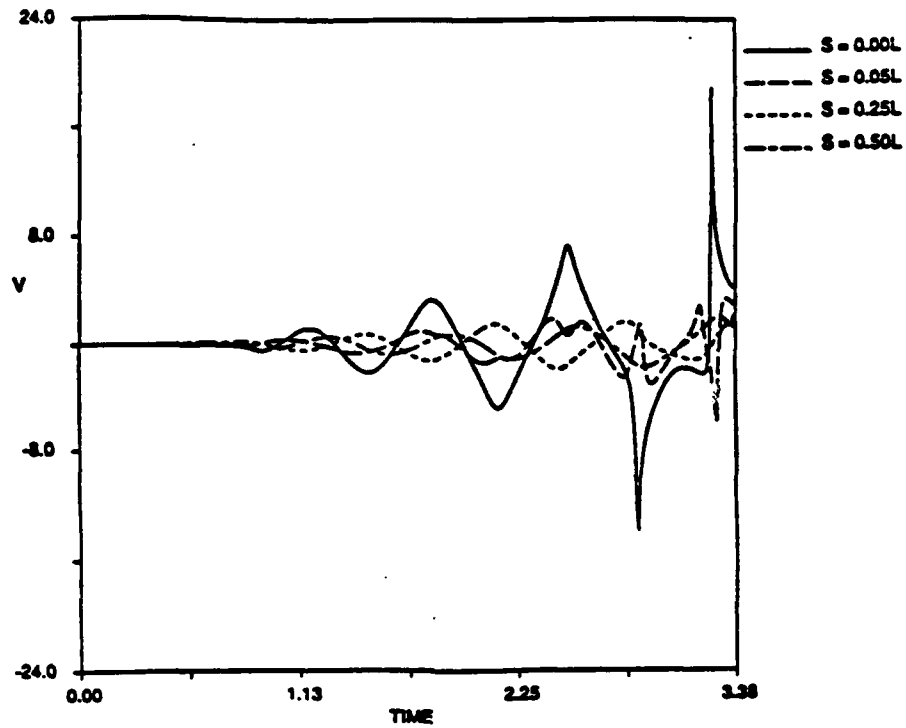


Figure 5.25: Numerical results: Normal velocity at four locations along the chain, for case under study.

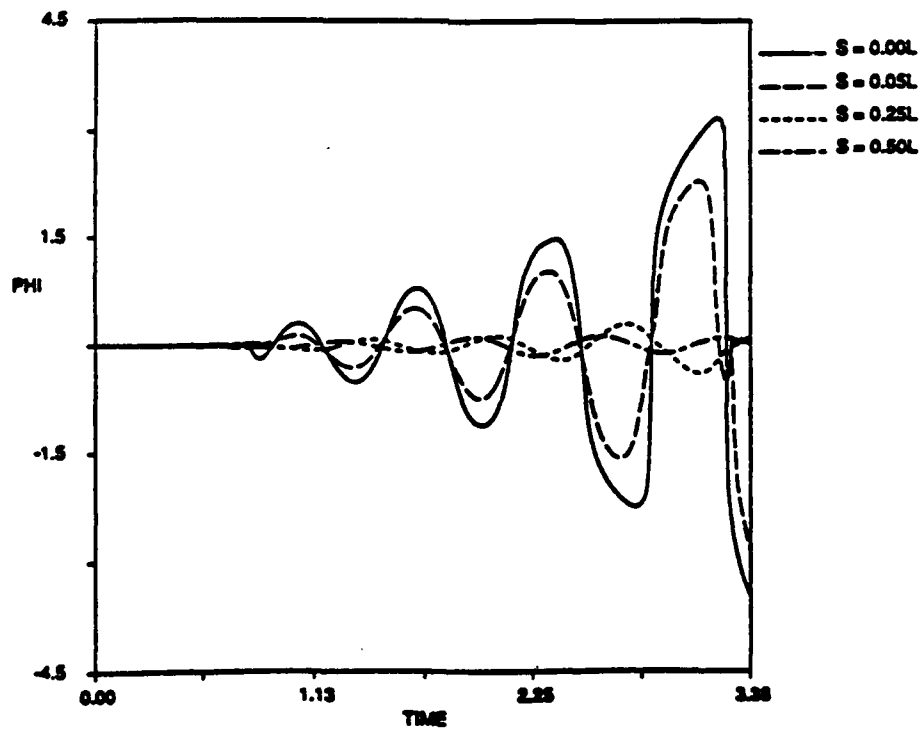


Figure 5.26: Numerical results: Angle (radians) at four locations along the chain, for case under study.

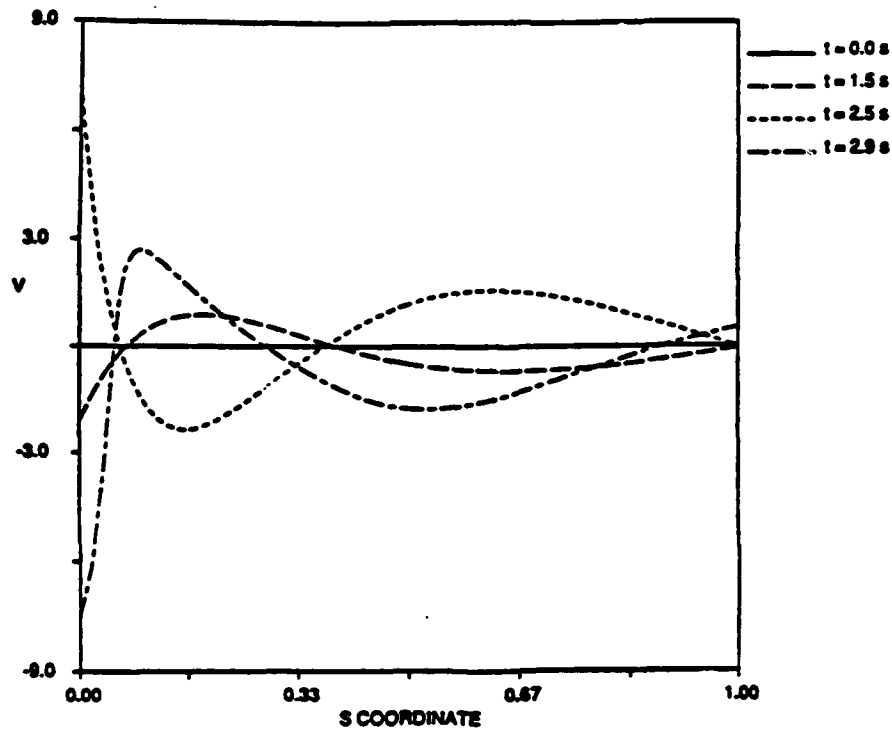


Figure 5.27: Numerical results: Normal velocity along chain at four different times, for case under study.

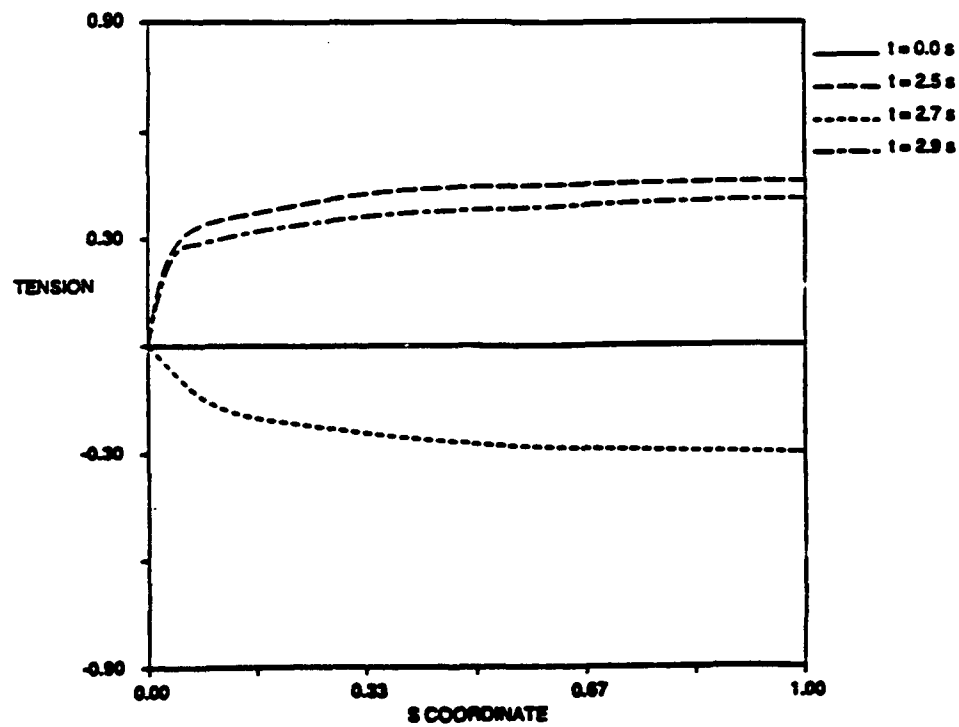


Figure 5.28: Numerical results: Dynamic tension along chain at four different times, for case under study.

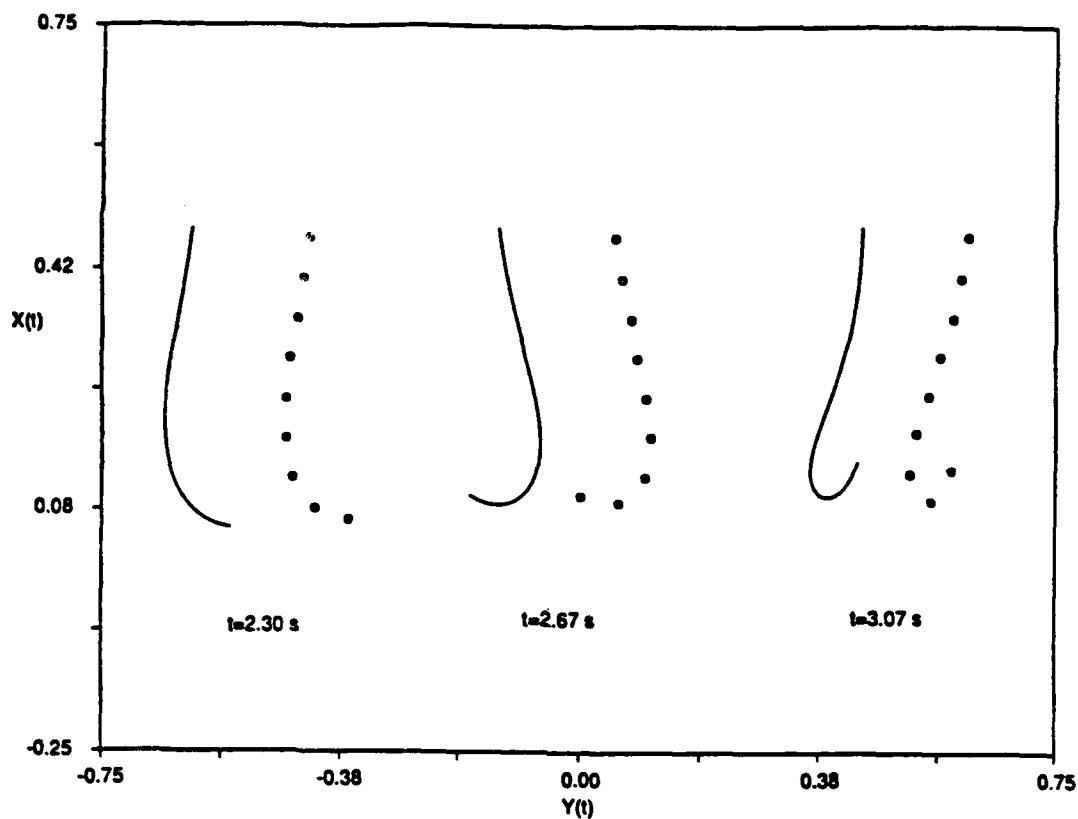


Figure 5.29: Comparison of experimental and numerical results for collapsing chain: lower half of chain.

numerical technique accurately predicts the displacement up to the point where tension was lost and good agreement was found at the point where the chain intersects itself ($t=3.8$ s, figure 5.30).

Figure 5.31 depicts the experimental results for the chain intersection with itself. This intersection was found to occur at the same time predicted numerically. It should be noted that the experimental tests did remain two-dimensional as demonstrated by the free-end colliding with the chain.

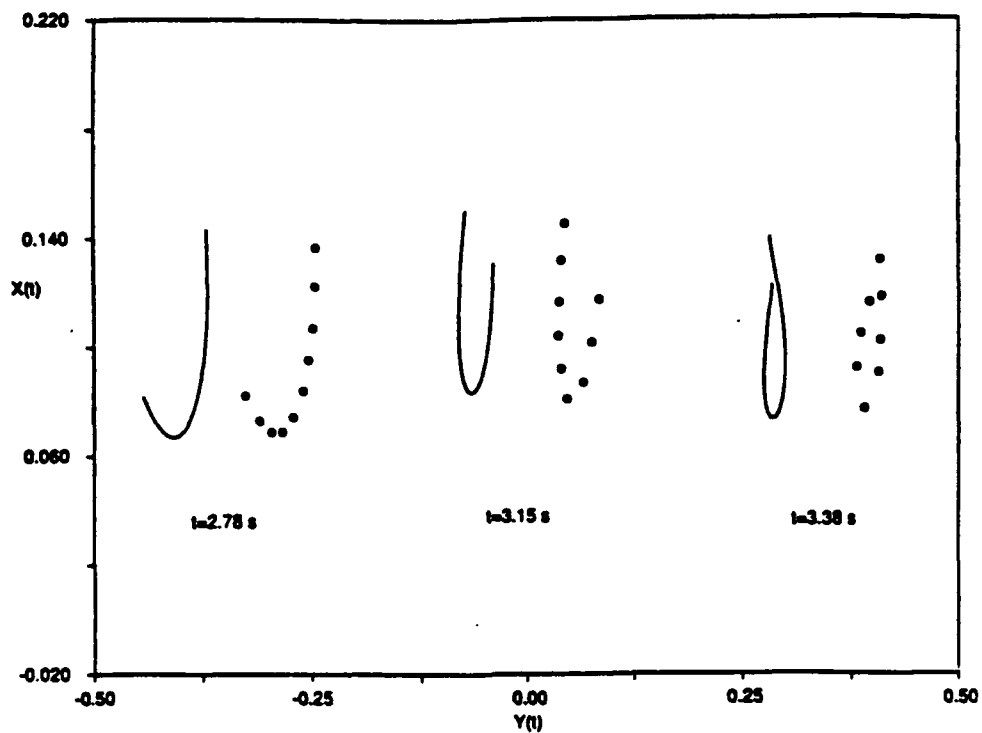


Figure 5.30: Comparison of experimental and numerical results for collapsing chain: lower one-eighth of chain.

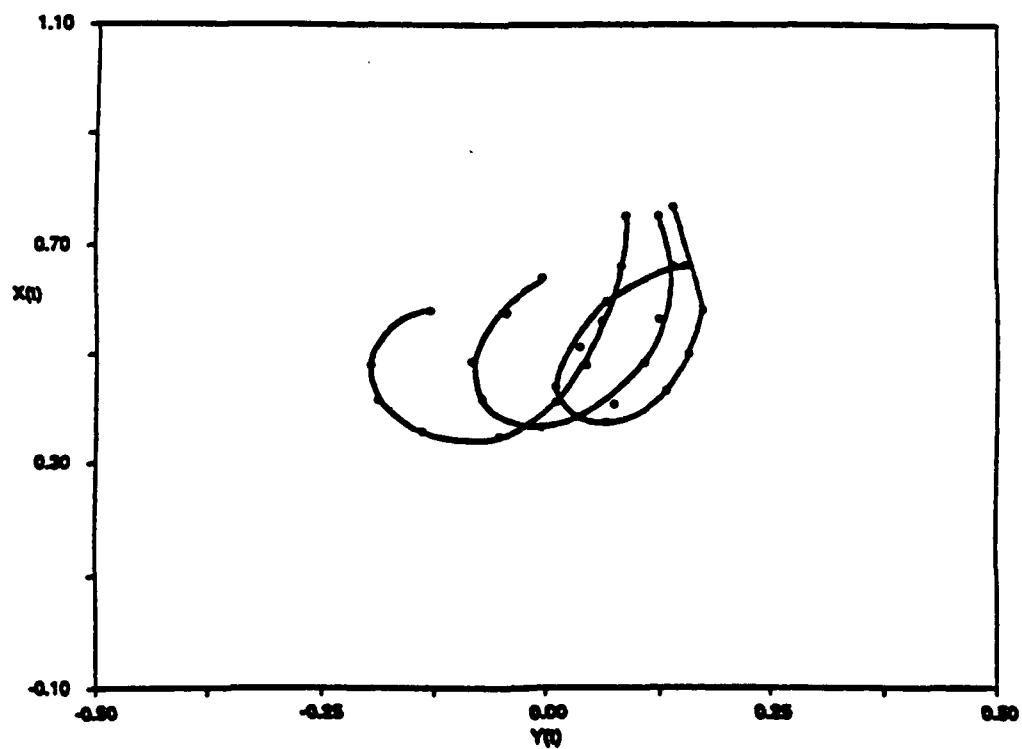


Figure 5.31: Experimental results: Chain configuration at several times prior to the collapse of the lower region.

Chapter 6

Analysis of Elastic Cable Behavior

6.1 Introduction

Up to this point, we have considered the dynamics of cables with infinite elastic stiffness. In this chapter we relax this restriction and incorporate elasticity in the equations of motion.

The effects of elasticity can be separated into two categories; quasi-static stretching and elastic or longitudinal waves. The significance of quasi-static stretching has been the subject of extensive research in the past (see for example [26], [63], and [67]) and will be addressed in section 6.2. Insight into the importance of elastic waves can be gained by considering the relative magnitudes of transverse and elastic wave speeds. Blik [6], using the method of characteristics, derived expressions for the transverse and elastic wave speeds C_{tr} and C_{el} , respectively, for an elastic cable. Assuming a linear stress-strain relation, the expressions are given by

$$C_{tr} = \pm \left[\frac{T}{(m + m_a)(1 + e)} \right]^{1/2} \quad (6.1)$$

$$C_{el} = \pm \left[\frac{EA}{m} \right]^{1/2} \quad (6.2)$$

Therefore, the ratio of wave speeds is roughly given by

$$\frac{C_{el}}{C_{tr}} \approx \left[\frac{EA}{T} \right]^{1/2} \quad (6.3)$$

For low tension values this ratio is very large, therefore, the fundamental frequency of elastic waves corresponds to a very high-order transverse mode. If the cable tension is large, it must still remain below an upper bound given by the breaking stress. For metallic cables, the upper bound is given by

$$\frac{T}{A} = \mu < \mu_b \ll E \quad (6.4)$$

where μ and μ_b denote the axial and breaking stress, respectively. Therefore, for metallic cables, the ratio of wave speeds remains high regardless of the cable tension [69].

For the reasons discussed above, if the excitation frequency is narrow-banded and corresponds to a low-order transverse mode, it can be assumed that elastic vibrations will not be excited. However, if the excitation frequency is broad-banded, sufficient energy may exist at high frequency to excite elastic waves.

The results derived in section 5.6 (figure 5.23) demonstrate that the response of the hanging chain to large amplitude excitation is characterized by impulse-like tension peaks. The energy content of these tension peaks is broad-banded, which brings into question the validity of neglecting elasticity in this case.

To resolve this question, a linear stress-strain model was incorporated into the implicit finite-difference algorithm discussed in chapter 3. An implicit time domain routine is necessary as the high propagation speed of elastic waves would require prohibitively small time-step increments in an explicit algorithm [60]. To validate the model, we consider the linear dynamics of an elastic catenary, as discussed in the next section.

It should be reiterated that a major reason for the increase in low-tension systems is the frequent use of synthetic cables. Aside from the decrease in density, the modulus of elasticity E of synthetic cables is appreciably less than that of metallic cables. As a result, synthetic cables have reduced axial and flexural stiffness than metallic cables of equivalent size. The reduction in flexural stiffness simplifies storage and handling of the cable. This in fact is one of the major benefits of synthetic cables. The low axial stiffness, however, can result in substantial stretching and thus a large buildup of potential energy. This makes synthetic cables extremely dangerous in failure. For this reason, and the fact that the dynamics of highly extensible cables are not fully understood, large safety factors are

used in design and the diameters selected are often much greater than necessary, thereby reducing their benefits to some degree. The topic of highly elastic cables is the subject of on-going research at the Massachusetts Institute of Technology, under the direction of Professor M.S. Triantafyllou.

6.2 Elastic Motions of Shallow Sag Cables

The elastic dynamics of suspended cables undergoing quasi-static stretching, i.e. no elastic waves are excited, has received considerable attention. Much of the research was aimed at resolving a discrepancy between taut-string results and inelastic horizontal catenary solutions in the limit that the cable sag to span ratio approaches zero. A clear explanation of the phenomena involved was presented by Irvine and Caughey [26]. Their results demonstrate that the significance of elastic effects is governed by the ratio of elastic to catenary stiffness, denoted as λ^2 . Also shown was that for shallow sag cables, the fundamental natural frequency of symmetric modes crosses the fundamental frequency of antisymmetric modes at a critical value of λ^2 , the so-called mode cross-over phenomena. Triantafyllou and Grin-fogel [69] show that the dynamics of inclined cables are distinctly different than those of horizontal cables in that frequency cross-overs do not occur and that large dynamic tension amplification occurs in the region of avoided crossings. Their results are based on more general asymptotic solutions, also derived by Triantafyllou [67], in which elastic waves are retained.

For completeness, we derive the linear solutions presented by Irvine and Caughey [26] in terms of body-fixed coordinates. These results are then used to verify the accuracy of the numerical algorithm.

6.2.1 Derivation of Linear Equations

We consider the dynamics of a perfectly flexible cable supported by two frictionless end supports at the same level, as shown in figure 6.1. The cable is assumed to have a small sag to span ratio, i.e. $\delta/S < 1/8$ where δ and S denote the cable sag and span respectively. Irvine and Caughey [26] have shown that within the linear regime, i.e. small motions, the

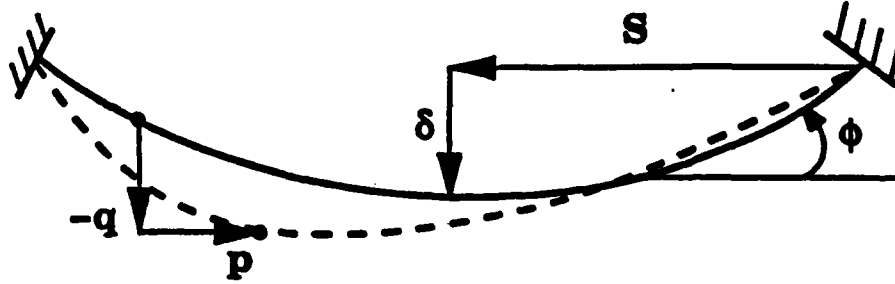


Figure 6.1: Cable suspended between two endpoints.

out-of-plane dynamics decouple from in-plane dynamics. This is because, to first-order, out-of-plane motions involve not additional cable tension. In addition, Rega *et al* [57] demonstrated that for nonlinear motions, planar oscillations are stable, with the exception of the case where the in-plane linear frequency is twice the out-of-plane natural frequency. As such, in this section we restrict our attention to two-dimensional dynamics. The two-dimensional governing equations and compatibility relations for an elastic cable, as derived in chapter 2, are given by

$$\begin{aligned}
 m\left(\frac{\partial u}{\partial t} - v\frac{\partial \phi}{\partial t}\right) &= \frac{\partial T}{\partial s} - w_o \sin \phi \\
 m\left(\frac{\partial v}{\partial t} + u\frac{\partial \phi}{\partial t}\right) &= T\frac{\partial \phi}{\partial s} - w_o \cos \phi \\
 \frac{\partial u}{\partial s} - v\frac{\partial \phi}{\partial s} &= \frac{\partial e}{\partial t} \\
 \frac{\partial v}{\partial s} + u\frac{\partial \phi}{\partial s} &= \frac{\partial \phi}{\partial t}(1 + e) \\
 T &= EAe.
 \end{aligned} \tag{6.5}$$

Here we have adopted the same nomenclature defined in chapter 2, with the exception that the angle ϕ is measured with respect to the horizontal, rather than the vertical, as shown in figure 6.1.

We seek to study the linear dynamics of the cable by considering small motions from the static configuration. Toward this end, we decompose the variables into static and dynamic terms as follows:

$$T = T_0 + T_1 \quad (6.6)$$

$$\phi = \phi_0 + \phi_1$$

$$e = e_0 + e_1$$

where the subscripts 0 and 1 denote static and dynamic quantities, respectively, and all dynamic quantities are assumed to be of order $O(\epsilon)$, where $\epsilon \ll 1$.

Eliminating all dynamic quantities from (6.5) yields the equations of static equilibrium.

$$\begin{aligned} \frac{\partial T_0}{\partial s} &= w_0 \sin \phi_0 \\ T_0 \frac{\partial \phi_0}{\partial s} &= w_0 \cos \phi_0 \\ T_0 &= EAe_0. \end{aligned} \quad (6.7)$$

The solution of (6.7) gives the shape of the catenary. These equations can be written in a more convenient form as follows:

$$\begin{aligned} T_0 &= \frac{H}{\cos \phi_0} \\ \frac{\partial \phi_0}{\partial s} &= \frac{\alpha}{L} \cos^2(\phi_0) \end{aligned} \quad (6.8)$$

where H is the horizontal component of the static tension and α is given by

$$\alpha = \frac{w_0 L}{H}. \quad (6.9)$$

For cables with small sag to span ratios, the slope of the cable is everywhere small. Therefore, $\cos(\phi_0) \simeq 1$ and the static solution can be expressed as

$$\begin{aligned} T_0 &\simeq H \\ \sin \phi_0 &\simeq \phi_0 \simeq \frac{\alpha}{L}s. \end{aligned} \quad (6.10)$$

For small motions we can approximate the velocities in terms of small displacements from the static configuration, as follows:

$$\begin{aligned} u &\simeq \frac{\partial p}{\partial t} \\ v &\simeq \frac{\partial q}{\partial t} \end{aligned} \quad (6.11)$$

where p and q are the tangential and normal displacements from the static configuration, respectively.

Substitution of (6.6), (6.10), and (6.11) into (6.5), removing the static solution, and retaining only first-order quantities yields

$$\begin{aligned} m \frac{\partial^2 p}{\partial t^2} &= \frac{\partial T_1}{\partial s} - \phi_1 \frac{\alpha H}{L} \\ m \frac{\partial^2 q}{\partial t^2} &= T_1 \frac{\alpha}{L} + H \frac{\partial \phi_1}{\partial s} \\ \frac{\partial p}{\partial s} - q \frac{\alpha}{L} &= \frac{T_1}{EA} \\ \frac{\partial q}{\partial s} + p \frac{\alpha}{L} &= \phi_1. \end{aligned} \quad (6.12)$$

Note that we have removed the time derivatives from the compatibility relations by integrating the two equations in time. For small displacements, longitudinal motions are small compared to transverse motions. As such,

$$p \frac{\alpha}{L} \ll \frac{\partial q}{\partial s}, \phi_1 \quad (6.13)$$

therefore, we can neglect this term from the final equation in (6.12).

We eliminate the time dependence in (6.12) by considering harmonic motions, and express the variables as follows:

$$\begin{aligned} p_1 &= \bar{p}e^{i\omega t} \\ q_1 &= \bar{q}e^{i\omega t} \\ \phi_1 &= \bar{\phi}e^{i\omega t} \\ T_1 &= \bar{T}e^{i\omega t} \end{aligned} \quad (6.14)$$

where ω is the natural frequency of vibration. Introducing (6.14) into (6.12) yields

$$\begin{aligned} -m\omega^2 \bar{p} &= \frac{\partial \bar{T}}{\partial s} - \bar{\phi} \frac{\alpha H}{L} \\ -m\omega^2 \bar{q} &= \bar{T} \frac{\alpha}{L} + H \frac{\partial \bar{\phi}}{\partial s} \\ \frac{\partial \bar{p}}{\partial s} - \bar{q} \frac{\alpha}{L} &= \frac{\bar{T}}{EA} \\ \frac{\partial \bar{q}}{\partial s} &= \bar{\phi}. \end{aligned} \quad (6.15)$$

Finally, we integrate the first equation in (6.15) with respect to space yielding

$$\bar{T}(s) = h + \int_0^s (\bar{\phi} \frac{\alpha H}{L} - m\omega^2 \bar{p}) ds \quad (6.16)$$

where h is a constant. Assuming quasi-static stretching, no significant longitudinal dynamics are excited. The basis of this assumption is that for metallic cables, transverse wave speeds are, in general, much smaller than those of longitudinal waves [6]. Therefore, for low frequencies, longitudinal wavelengths are much greater than the overall cable length. However, for high excitation frequencies, longitudinal wavelengths may be less than L , and the quasi-static stretching assumption is no longer valid. This is an important consideration which must be taken into account in considering synthetic cables, which have a smaller Young's modulus than metallic cables, and therefore, smaller longitudinal wave speeds.

Introducing (6.16) into (6.15) and combining expressions yields

$$\frac{\partial^2 \tilde{q}}{\partial s^2} + \beta^2 \tilde{q} = -\frac{h\alpha}{HL} \quad (6.17)$$

$$\frac{\partial \tilde{p}}{\partial s} - \tilde{q} \frac{\alpha}{L} = \frac{h}{EA} \quad (6.18)$$

where

$$\beta = \omega \sqrt{\frac{m}{H}}. \quad (6.19)$$

These equations are equivalent to the linear equations derived by Irvine and Caughey [26] and can be combined to form a single equation in $\tilde{q}(s)$. Toward this end we integrate (6.18) along the cable and impose the boundary conditions $\tilde{p}(-L/2) = \tilde{p}(L/2) = 0$, which yields

$$h = -\frac{EA\alpha}{L^2} \int_{-L/2}^{L/2} \tilde{q} ds. \quad (6.20)$$

Substitution of (6.20) into (6.17) yields the linear equation for transverse motions.

$$\frac{\partial^2 \tilde{q}}{\partial s^2} + \beta^2 \tilde{q} = -\frac{\lambda^2}{L^3} \int_{-L/2}^{L/2} \tilde{q} ds \quad (6.21)$$

where

$$\lambda^2 = \left(\frac{EA}{H}\right) \left(\frac{w_o L}{H}\right)^2 \quad (6.22)$$

6.2.2 Analytic Solution of Linear Equations

Solutions of (6.17) and (6.18) can be separated into two classes of mode shapes, i.e. symmetric and antisymmetric modes. Herein, a symmetric in-plane mode is defined as a mode in which the vertical component of the mode is symmetric, and vice-versa. We will treat the two classes separately.

We first consider antisymmetric modes. According to (6.20), the additional tension component h is zero, independent of the cable elasticity. Therefore, (6.17) reduces to

$$\frac{\partial^2 \tilde{q}}{\partial s^2} + \beta^2 \tilde{q} = 0. \quad (6.23)$$

Solving this equation and imposing the boundary conditions $\tilde{q}(0) = \tilde{q}(L/2) = 0$ yields

$$\bar{q}_n(s) = A_n \sin\left(\frac{2\pi ns}{L}\right) \quad (6.24)$$

where the nondimensional frequencies are given by $\beta_n L = 2n\pi$ and $n = 1, 2, 3, \dots$

We next consider antisymmetric modes. Solving (6.17) and imposing the boundary conditions $\bar{q}(-L/2) = \bar{q}(L/2) = 0$ yields the following expression for $\bar{q}(s)$:

$$\bar{q}(s) = \frac{h\alpha}{LH\beta^2} \left(\frac{\cos(\beta s)}{\cos(\beta L/2)} - 1 \right). \quad (6.25)$$

In order to determine the natural frequencies, (6.25) is substituted into (6.21), providing the following transcendental equation for βL :

$$\tan(\beta L/2) = \beta L/2 - \frac{4}{\lambda^2} (\beta L/2)^3 \quad (6.26)$$

As stated by Irvine and Caughey [26], (6.26) "is of fundamental importance in the theory of cable vibrations." In physical terms, λ^2 expresses the ratio of elastic to catenary stiffness. For cables with low elastic stiffness, i.e. $\lambda^2 \rightarrow 0$, we recover the classic solution of the taut string equation, where

$$\lim_{\lambda^2 \rightarrow 0} \beta_n L = (2n - 1)\pi, \quad n = 1, 2, 3, \dots \quad (6.27)$$

For large values of λ^2 , the cable can be considered inextensible, and (6.26) reduces to the transcendental equation for an inextensible catenary, where

$$\tan\left(\frac{\beta L}{2}\right) = \frac{\beta L}{2} \quad (6.28)$$

This equation was first derived by Rohrs [58] and the first two roots are given by

$$\lim_{\lambda^2 \rightarrow \infty} \beta_{1,2} L = 2.86\pi, 4.92\pi. \quad (6.29)$$

As derived previously, the fundamental frequency of antisymmetric modes is given by $\beta_1 L = 2\pi$. However, as we have shown, solutions for the two limiting values of λ^2 fall on either side of this value. The relationship between λ^2 and the first root of (6.26) is

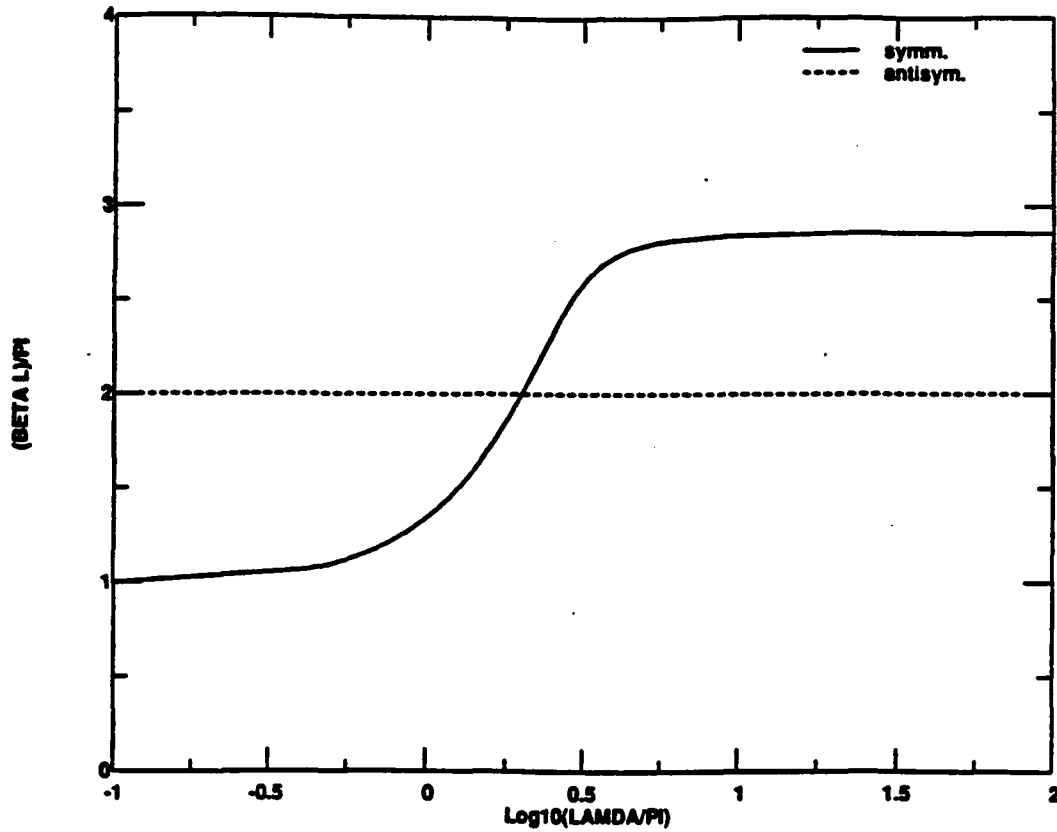


Figure 6.2: Dependence of fundamental natural frequency on λ .

shown in figure 6.2. Of particular interest is that symmetric natural frequencies cross the antisymmetric frequency for increasing values of λ^2 . The cross-over point for the first mode corresponds to $\lambda = 2\pi$, and a steep transition in frequency occurs near this value. Similar frequency cross-overs occur at other modes as well [7].

The mode shapes for longitudinal modes can be determined by introducing (6.25) into (6.18) and integrating along the cable from $-L/2$ to s . Imposing the boundary condition $\tilde{p}(-L/2) = 0$ yields

$$\tilde{p}(s) = \frac{h}{H} \left(\frac{\alpha}{\beta L} \right)^2 \left[\left(\frac{\beta L}{\lambda} \right)^2 (s + L/2) + \frac{1}{\beta} \left(\frac{\sin(\beta s)}{\cos(\beta L/2)} + \tan(\beta L/2) \right) - (s + L/2) \right]. \quad (6.30)$$

Note that for symmetric normal modes, longitudinal modes are antisymmetric.

6.2.3 Numerical Results

In order to verify the numerical algorithm's ability to model elastic cable behavior, simulations of the suspended catenary problem were conducted for a range of λ values. Specifically, we attempt to demonstrate numerically the transition in mode shapes predicted by linear theory.

As discussed, the linear equations are derived on the basis of small displacements from some known static configuration. Therefore, because the nonlinear terms are retained in the numerical model, excitation amplitudes were maintained at small values. A separate routine was developed to calculate the static shape, as input to the dynamic algorithm. In addition, the boundary conditions were modified, with the new conditions being given by

$$u(t, -L/2) = 0 \quad (6.31)$$

$$v(t, -L/2) = 0$$

$$u(t, L/2) = 0$$

$$v(t, L/2) = 0$$

Numerical solutions were obtained using a cable of unit length and the nondimensional parameters $\alpha = 0.1$ and $h/H = 0.01$. The normal and tangential velocities along the cable were initialized according to the linear solutions given by (6.25) and (6.30), respectively.

Numerical results for the calculated symmetric mode shapes, after 20 cycles have elapsed, are shown in figures 6.3, 6.4, and 6.5 for $\lambda = \pi$, 2π , and 3π , respectively. Also shown are the linear results derived in the previous section. As readily seen, the two results are indistinguishable and the numerical algorithm is able to accurately model the modal transition that occurs.

6.3 Extensible Dynamics of Hanging Chain

The asymptotic and numerical solutions of the hanging chain problem presented in chapter 5 were obtained under the assumption that the chain was inextensible. In this section, we

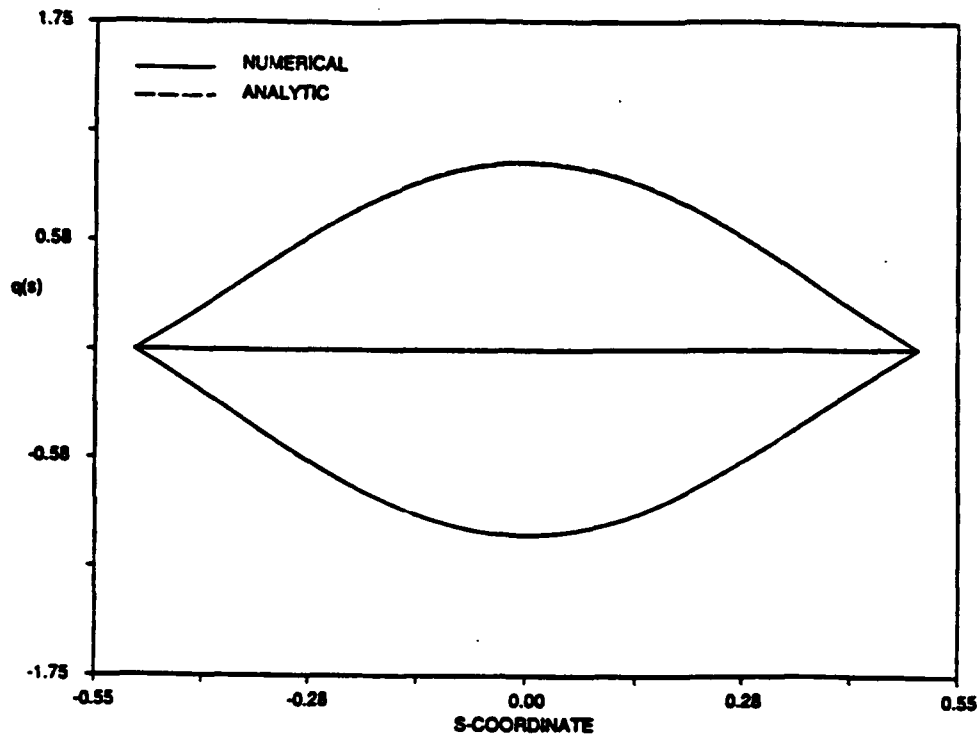


Figure 6.3: Transverse symmetric mode shape for $\lambda = \pi$; numerical and analytic results shown.

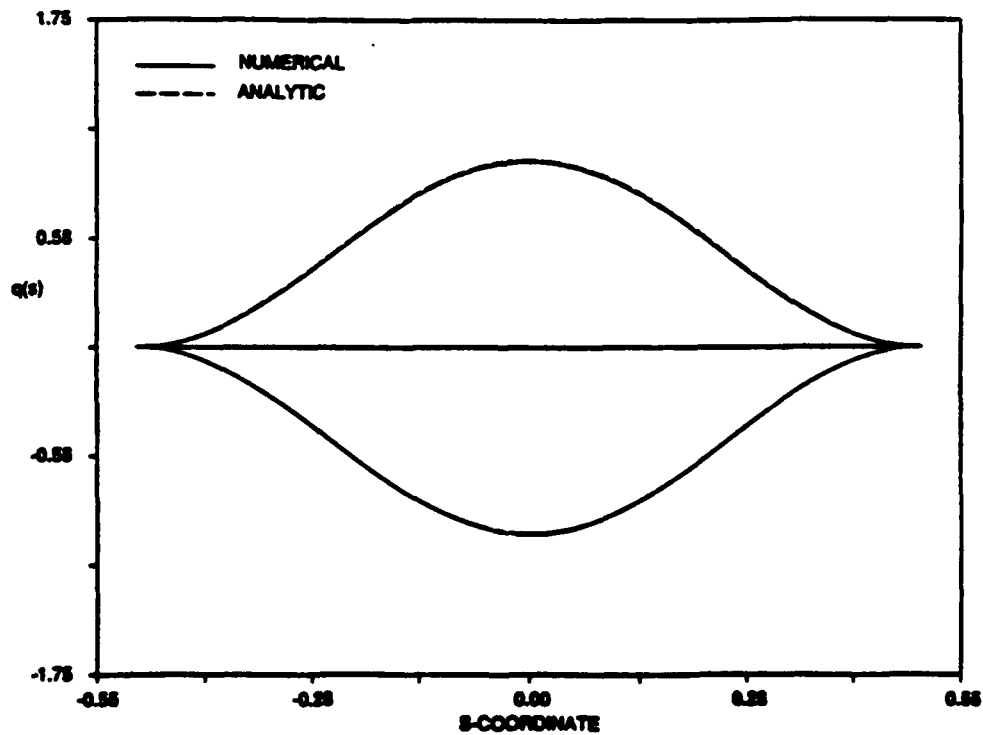


Figure 6.4: Transverse symmetric mode shape for $\lambda = 2\pi$ (cross-over point); numerical and analytic results shown.

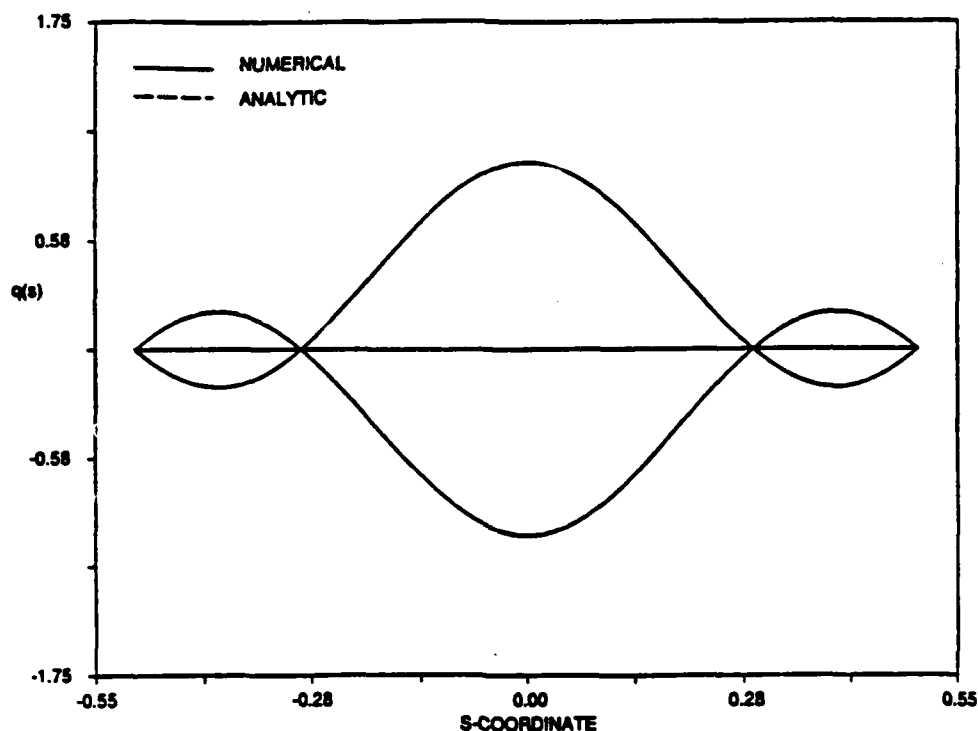


Figure 6.5: Transverse symmetric mode shape for $\lambda = 3\pi$; numerical and analytic results shown.

consider the extensible chain dynamics to verify the validity of this assumption. In addition, the effects of reducing the elastic stiffness in the chain are investigated to determine at which point elasticity becomes important.

6.3.1 Moderate Excitation Amplitudes

The chain used throughout the experimental tests was comprised of steel links, roughly 5 mm in diameter. The equivalent nondimensional elastic stiffness was found to be on the order of $EA/w_0L = EA^* = 4 \times 10^5$. This value will be used as a reference value for determining the validity of neglecting elasticity. For this value of EA^* , the ratio of elastic to transverse wave speeds is of order 600 or greater. A synthetic chain of the same dimensions would have a ratio on the order of 60. The ratio of the fundamental elastic frequency to the driving frequency, assuming the elastic frequencies correspond to those associated with free-fixed end conditions, is given by

$$\tau_\omega = \frac{\pi[EA^*]^{1/2}}{\beta_n(1 + \sigma)} \quad (6.32)$$

where β_n is the n^{th} root of the Bessel function of the first kind and order 0.

Numerical simulations were conducted using the excitation amplitude given in section 5.4 ($Y_0 = 0.0087L$), for a range of EA^* values. The excitation frequency was chosen to correspond to resonance, i.e. $\sigma = 0$. Figure 6.6 shows the tension time history, at four locations along the chain, obtained using $EA^* = 4 \times 10^3$. Also shown are the results for the inextensible chain. As readily seen, elastic effects are insignificant for values of elastic stiffness above this value. This is attributable to the excitation frequencies remaining in a narrow frequency band, well below the elastic frequencies. Therefore, for moderate excitation amplitudes, it proves valid to neglect elasticity.

Numerical results are shown in figure 6.7 for a chain with very low elastic stiffness ($EA^* = 100$). The results show only a slight shift in frequency and amplitude occurs due to elasticity. The first elastic natural frequency, in this case, is roughly 8 times the excitation frequency.

6.3.2 Large Amplitude Excitation

Here we consider the large amplitude response of a chain with elasticity. Results are presented for the three cases listed in table 6.1. Figure 6.8 shows the tension time history, at four points along chain, using the value $EA^* = 4.0 \times 10^4$ (case 1). Note that this value is an order of magnitude below the reference value. As readily seen, elasticity does not affect the chain's dynamics for this case as elastic waves are not excited. These results show that the excitation energy, although broad-banded near the point of the chain's collapse, remains below the fundamental frequency of elastic waves. The frequency ratio in this case is large, as shown in table 6.1. Based on these results, and the results presented in the previous section, we can conclude that the results obtained in chapter 5, which are based on the assumption the chain is inextensible, are valid.

We next consider the effects of reducing the elastic stiffness further (cases 2 and 3). For case 2 we find that elastic waves do begin to develop (figure 6.9) after the tension peaks become sufficiently narrow in time, i.e. begin to look impulsive. Prior to the point

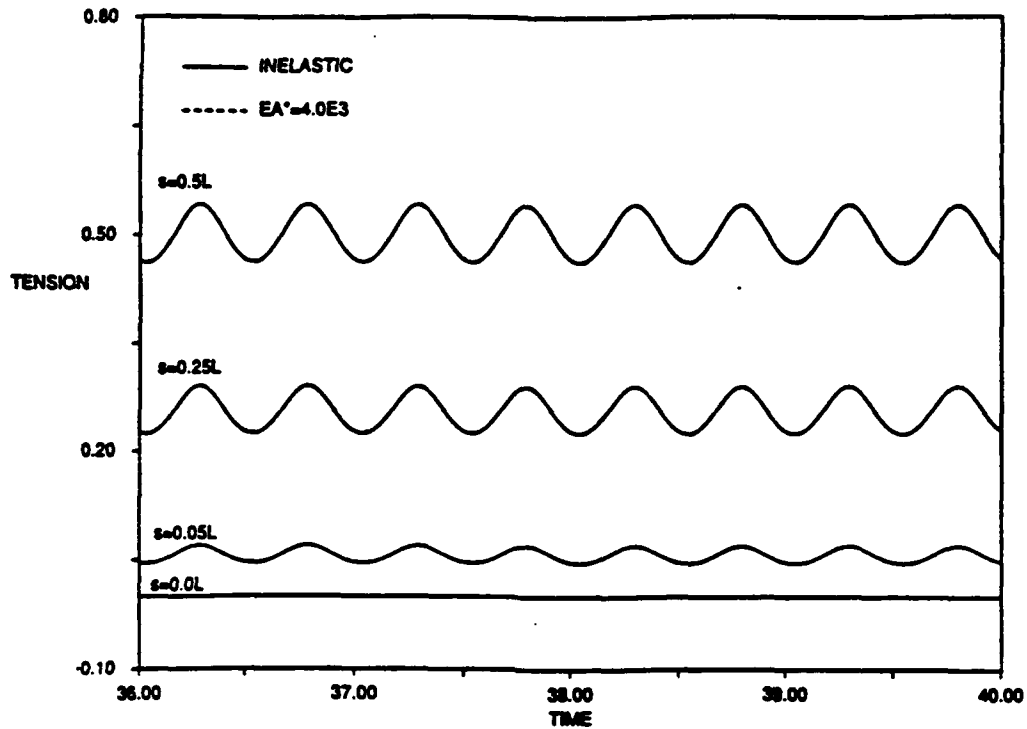


Figure 6.6: Comparison between tension time history at four locations along chain for inextensible chain and elastic chain ($EA^* = 4 \times 10^3$).

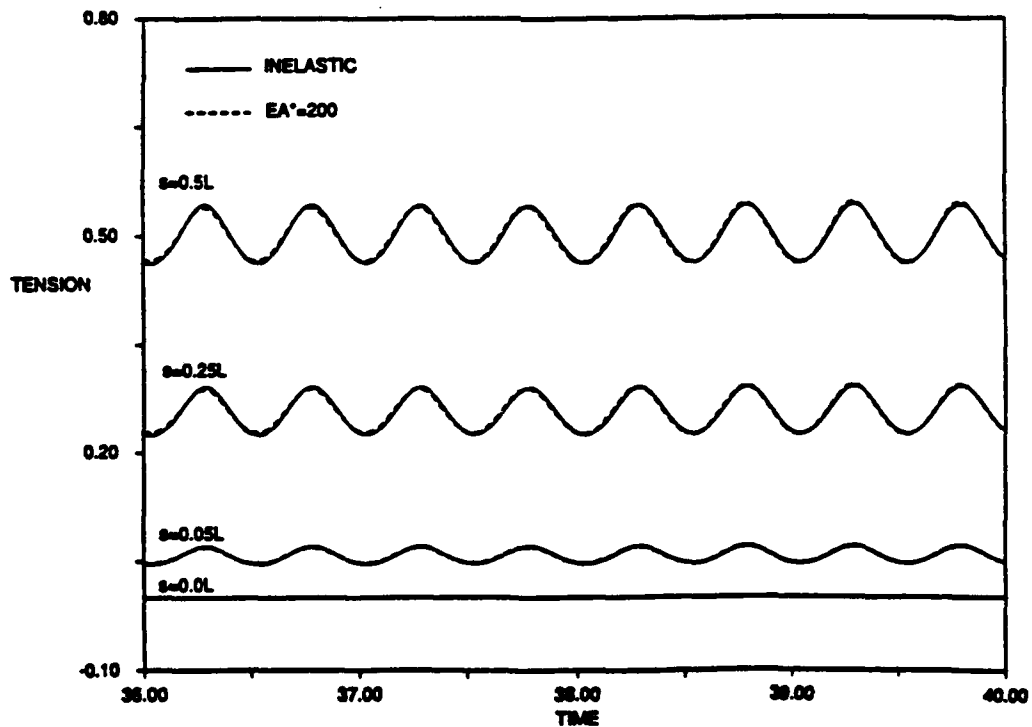


Figure 6.7: Comparison between tension time history at four locations along chain for inextensible chain and elastic chain ($EA^* = 200$).

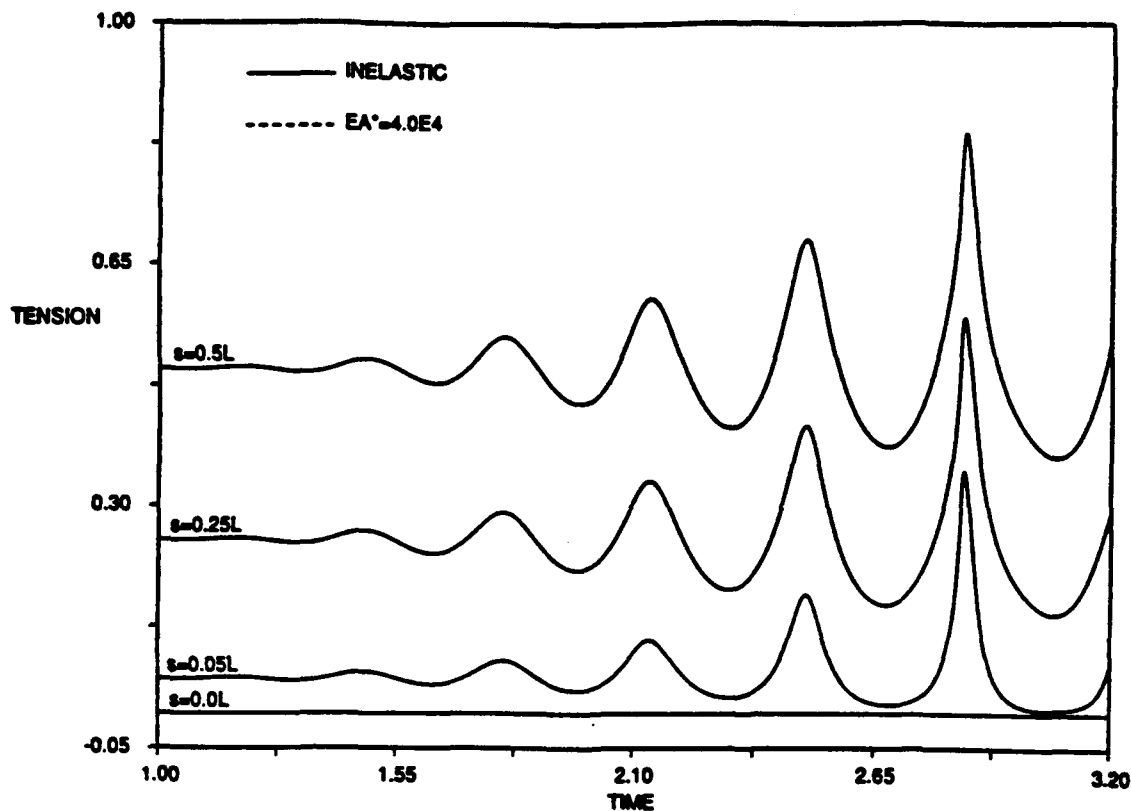


Figure 6.8: Comparison between tension time history at four locations along chain for inextensible chain and elastic chain ($EA^* = 4.0 \times 10^4$).

of maximum tension, no elastic effects are present. The observed frequency of the elastic waves (table 6.1) differs from the value predicted by linear theory by roughly 14 percent.

As shown in figure 6.9, the elastic wave amplitude grows in the direction away from the free boundary. The tension variation that occurs due to the elastic waves can be isolated by removing the tension found for the inextensible case. Here we find an interesting result. The elastic waves that form are not travelling waves. Instead, we find that a standing wave develops that encompasses the entire chain. The mode shape of this standing wave is

Case#	EA^*	ω^* (linear)	ω^* (observed)	τ_ω
1	4×10^4	314.	—	80
2	4×10^3	99.3	113.	25
3	4×10^2	31.4	36.6	8

Table 6.1: Case studies for analysis of elastic affects.

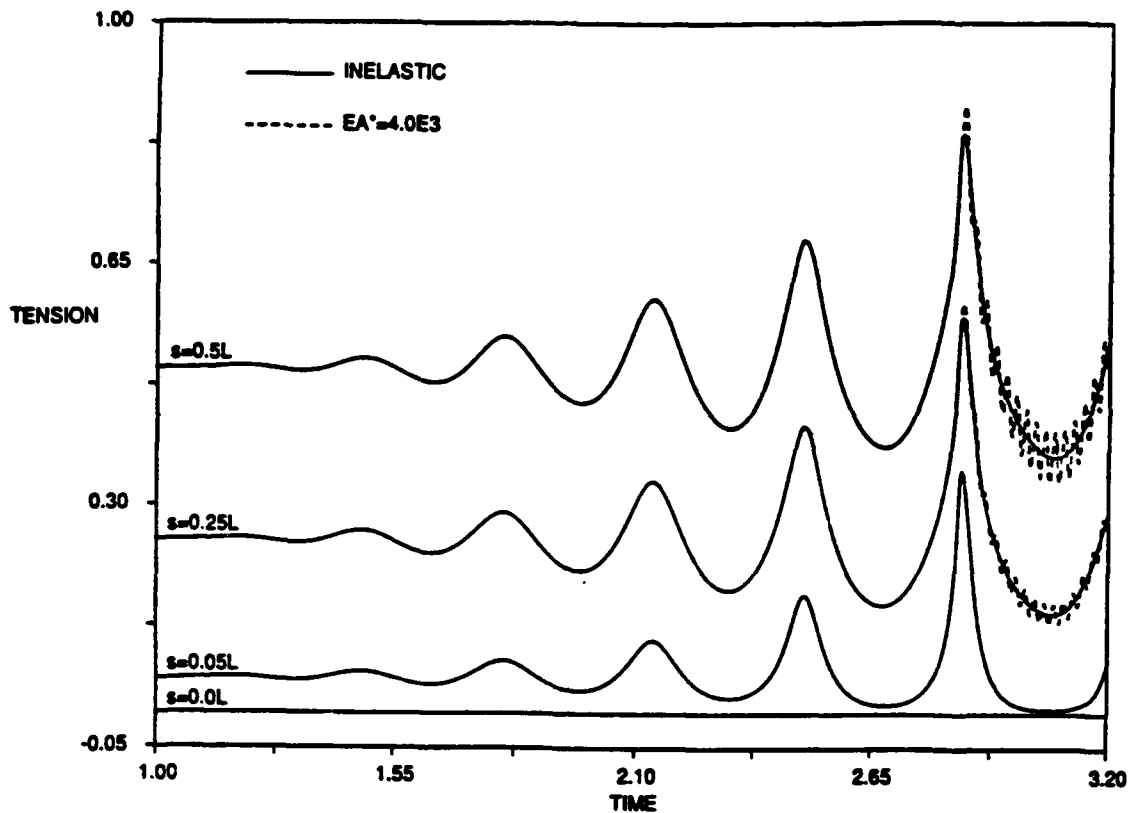


Figure 6.9: Comparison between tension time history at four locations along chain for inextensible chain and elastic chain, $EA^* = 4.0 \times 10^3$.

shown in figure 6.10, along with the linear mode shape of a straight cable with free-fixed boundary conditions. As shown, the largest discrepancy occurs near the free-end. In this region the curvature is greatest and curvature has been shown to have a significant affect on the elastic frequencies and mode shapes [9]. Curvature effects, therefore, may also account for the discrepancy in the observed elastic frequency.

Further proof that the elastic waves are stationary is provided by a contour plot of the elastic tension variation along the chain in time (figure 6.11). As shown, the characteristics are vertical, indicating elastic energy does not travel along the cable. If the elastic waves did travel, the characteristics would have a finite slope, given by the elastic wave speed.

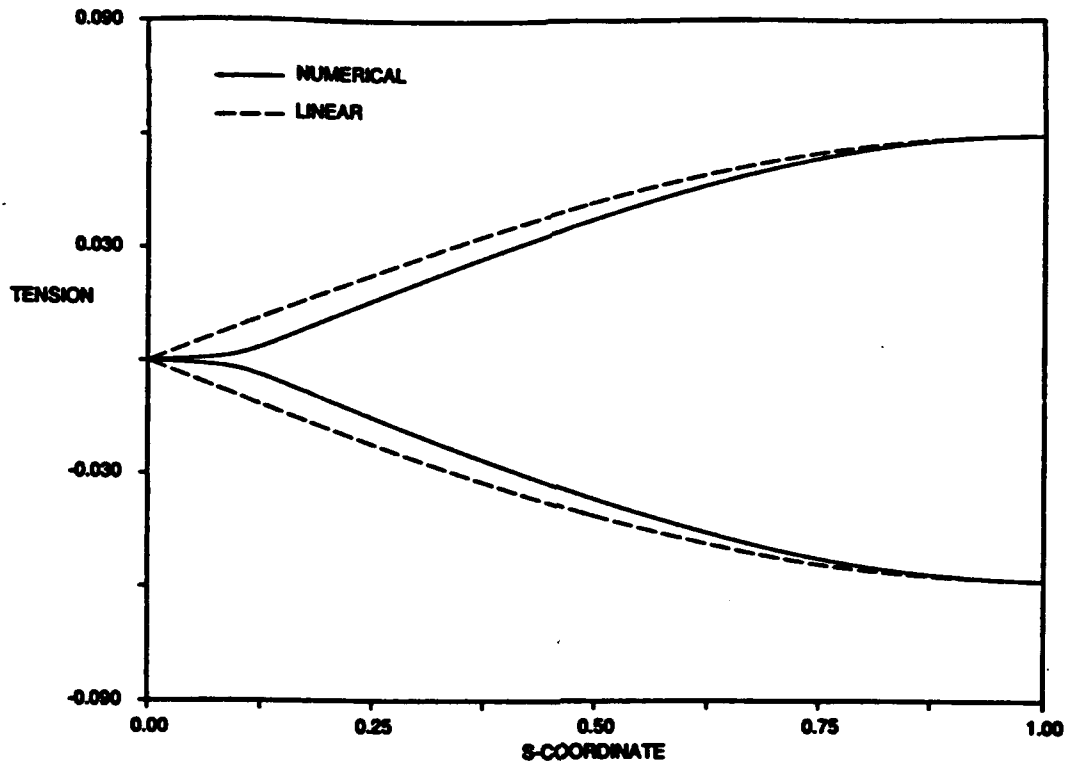


Figure 6.10: Mode shape for tension variation due to elastic waves, using $EA^* = 4.0 \times 10^3$.

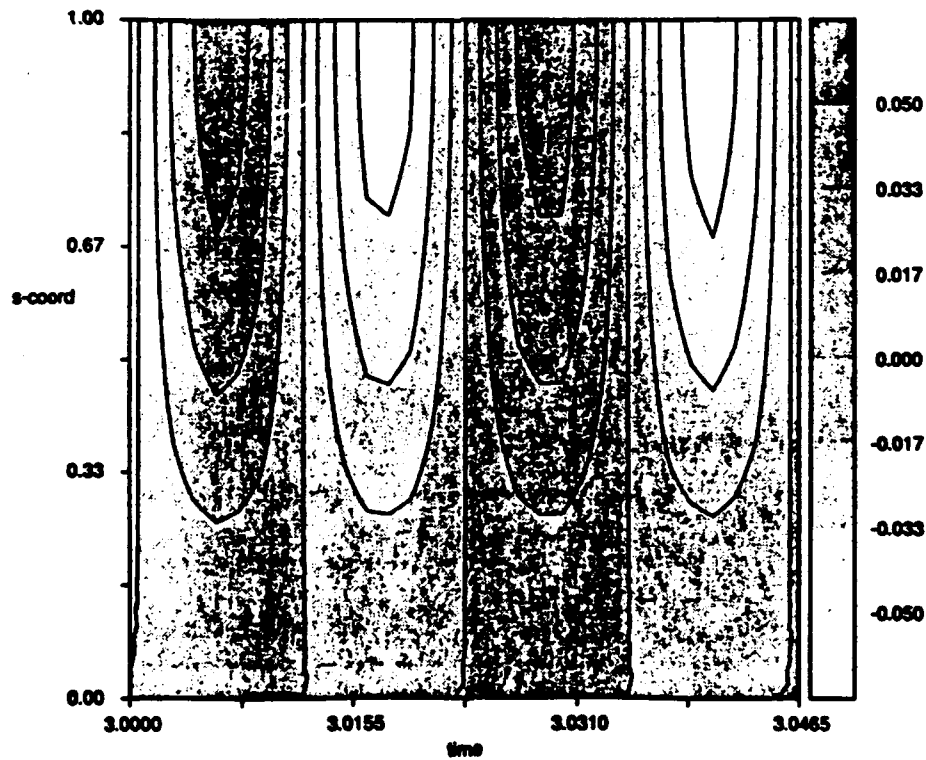


Figure 6.11: Contour plot of elastic tension variation in time and space for $EA^* = 4.0 \times 10^3$.

Similar results were obtained for still further reductions in the value of EA^* (case 3). Here, however, we find that elastic waves begin to develop at lower tension amplitudes (figure 6.12). In this case the fundamental elastic frequency is much closer to the excitation frequency, i.e. $r_\omega = 8$. Again we find that the elastic waves are stationary and qualitatively similar results are found for the mode shape (figure 6.13) and characteristics (figure 6.14).

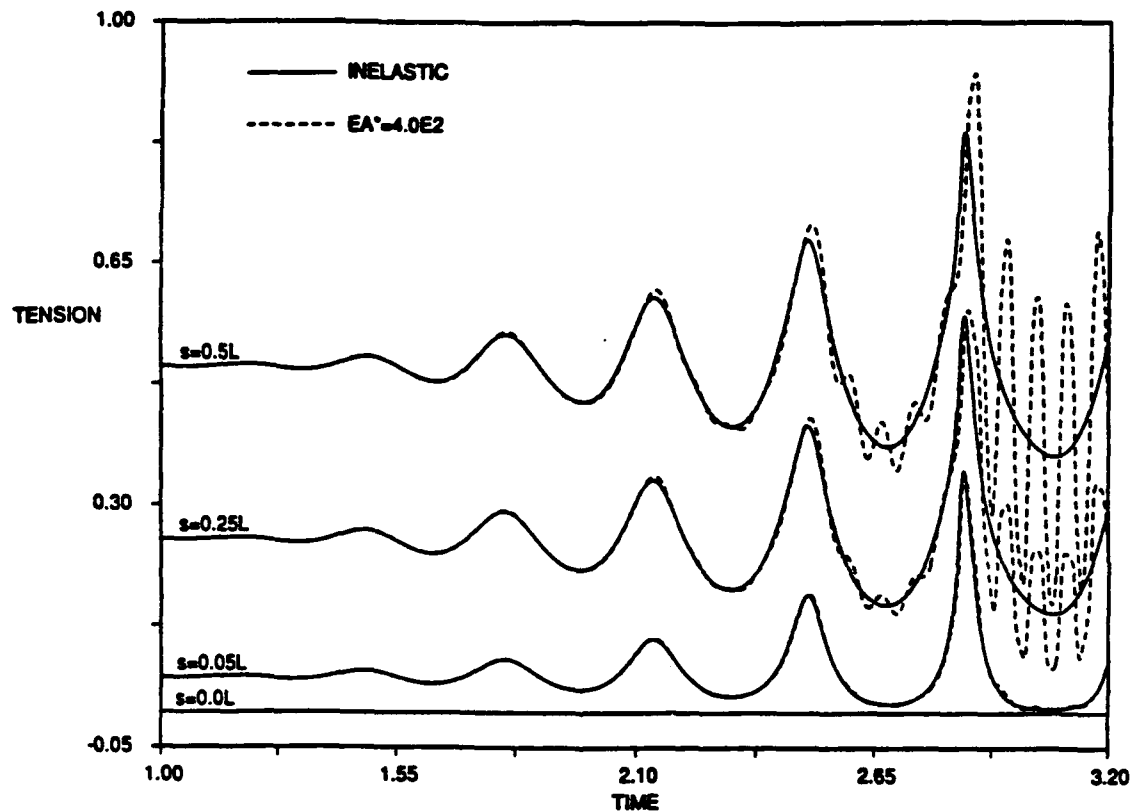


Figure 6.12: Comparison between tension time history at four locations along chain for inextensible chain and elastic chain, $EA^* = 4.0 \times 10^2$.

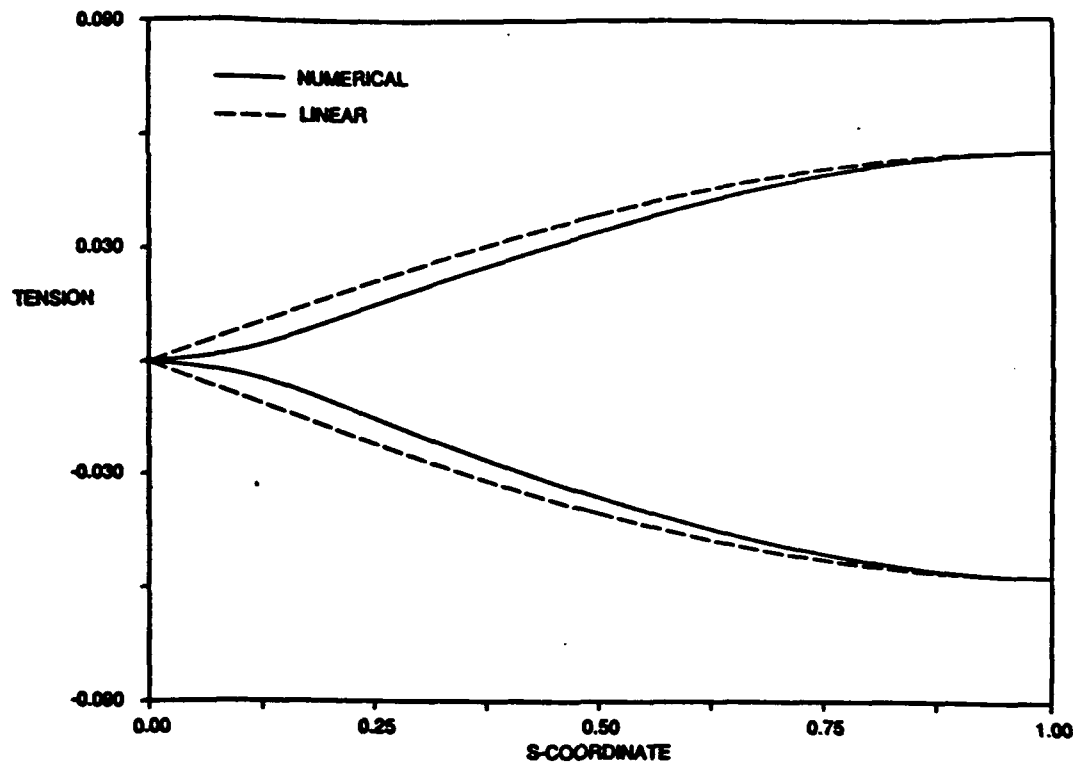


Figure 6.13: Mode shape for tension variation due to elastic waves, using $EA^* = 4.0 \times 10^2$.

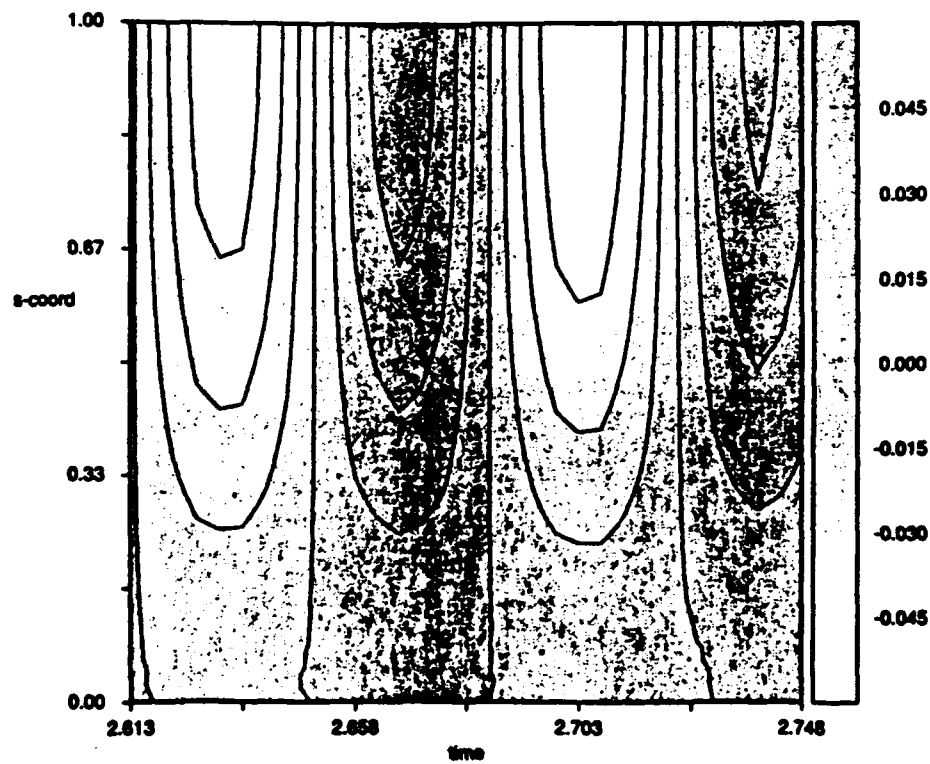


Figure 6.14: Contour plot of elastic tension variation in time and space for $EA^* = 4.0 \times 10^2$.

Chapter 7

Applications

7.1 Introduction

In this chapter we consider applications of the methodology presented in previous chapters. In particular, we consider the coupled dynamics of a remotely operated vehicle (ROV) employing a low-tension tether.

7.2 Coupled Low-Tension Tether/Vehicle System

Tethered remotely operated underwater vehicles are used extensively by the offshore industry and oceanographic research community. The ROV systems that have been developed can be separated into two classes. The first entails a direct connection from the surface to a heavy vehicle, through a highly tensioned cable. As such, the vehicle is directly coupled to the ship motions. To eliminate this coupling, an alternative system has been developed which is comprised of two components. The neutrally buoyant vehicle is connected by a low-tension tether to a heavy working platform, which in turn is connected to the surface by a high tension cable as shown in figure 7.1. This decouples the vehicle from the sea surface. Here we focus on the coupled dynamics of the low-tension tether and vehicle.

Simulations are conducted using the algorithm developed for low-tension cables, combined with a dynamic model of the ROV [24]. A number of vehicle-tether simulation techniques have been developed previously (see for example [3], [38], [70]). However, these

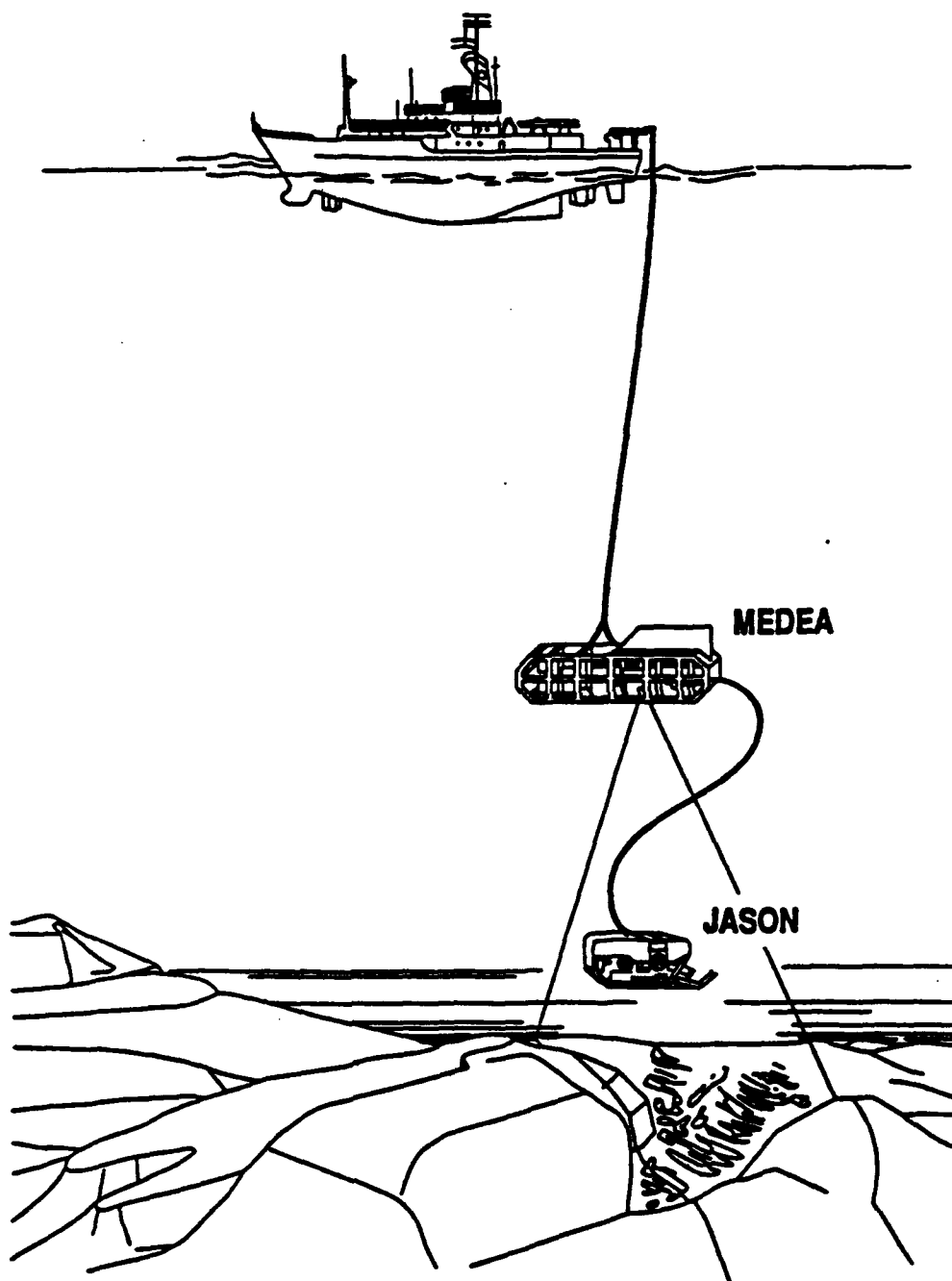


Figure 7.1: Two component remotely operated underwater vehicle system. (Courtesy of the Woods Hole Oceanographic Institution).

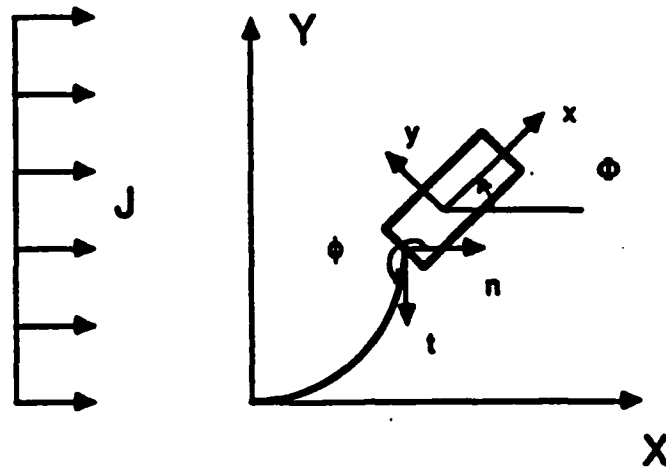


Figure 7.2: Tether and vehicle coordinate systems.

models greatly simplified the implementation of the cable dynamics.

7.2.1 Equations of Motion

The equations are derived for motion in the vertical plane and include gravitational forces. For simulating motion in a horizontal plane, all the gravitational forces are set equal to zero.

Separate body-fixed coordinate systems are used for the tether and the vehicle (figure 7.2). For the tether, we employ the coordinates \hat{i} and \hat{n} defined in chapter 2. We consider the vehicle to be a rigid body and place the origin of its coordinate system at its center of gravity. The x -axis defines the direction of *surge* motion and the y -axis defines the direction of *heave* motion.

The ROV operates in a spatially uniform current of magnitude J . The direction of the current is constant though the magnitude can vary with time. We define a global coordinate system such that the X -axis is parallel to the current direction. Transformation from the moving coordinate system of the vehicle to the global coordinate system is accomplished

through an Eulerian transformation.

The equations for the tether and the vehicle are presented separately and these results are then coupled through a set of relations.

Tether Equations

We are interested in accurately modeling the low-tension behavior of tethers. As such, we retain the effects of bending stiffness and consider the tether as inextensible. The two-dimensional governing equations and compatibility relations, as derived in chapter 2, are given by

$$\begin{aligned}
 m \left(\frac{\partial u}{\partial t} - v \frac{\partial \phi}{\partial t} \right) &= \frac{\partial T}{\partial s} - w \sin \phi - \frac{1}{2} \rho d C_{dt} \pi u_r |u_r| + EI \frac{\partial \phi}{\partial s} \frac{\partial^2 \phi}{\partial s^2} \quad (7.1) \\
 m \left(\frac{\partial v}{\partial t} + u \frac{\partial \phi}{\partial t} \right) + m_a \frac{\partial v_r}{\partial t} &= T \frac{\partial \phi}{\partial s} - w \cos \phi - \frac{1}{2} \rho d C_{dn} v_r |v_r| - EI \frac{\partial^3 \phi}{\partial s^3} \\
 \frac{\partial \phi}{\partial t} &= \frac{\partial v}{\partial s} + u \frac{\partial \phi}{\partial s} \\
 \frac{\partial u}{\partial s} &= v \frac{\partial \phi}{\partial s}
 \end{aligned}$$

where T denotes the effective tension, u_r and v_r are relative velocities defined by:

$$\begin{aligned}
 u_r &= u - J \cos \phi \\
 v_r &= v + J \sin \phi
 \end{aligned} \quad (7.2)$$

Vehicle Equations

The governing equations for planar motion of the vehicle, as derived by Moxnes [46], are given as follows:

$$(M + A_{11})\frac{\partial U}{\partial t} - (MV + A_{11}V_r)\frac{\partial \Phi}{\partial t} = (B - W)\sin \Phi + H_x + R_x + T_x + S_x \quad (7.3)$$

$$(M + A_{22})\frac{\partial V}{\partial t} + (MU + A_{22}U_r)\frac{\partial \Phi}{\partial t} = (B - W)\cos \Phi + H_y + R_y + T_y + S_y \quad (7.4)$$

$$(I_{zz} + A_{66})\frac{\partial^2 \Phi}{\partial t^2} = x_b B \cos \Phi - y_b B \sin \Phi - C_{d\Phi} \frac{\partial \Phi}{\partial t} \left| \frac{\partial \Phi}{\partial t} \right| + R_\Phi + x_c(T_y + S_y) - y_c(T_x + S_x). \quad (7.5)$$

The left-hand-side of (7.3)-(7.5) are the inertial forces. The surge velocity is U , the heave velocity is V , and the pitch angle is Φ . M is the vehicle mass and I_{zz} the moment of inertia about the z-axis. A_{11} , A_{22} , and A_{66} are the added masses for surge and heave and the added moment of inertia for pitch, respectively. Coupling terms involving added mass and added moments of inertia have been ignored. The relative velocities U_r and V_r are defined as:

$$U_r = U - J \cos \Phi \quad (7.6)$$

$$V_r = V + J \sin \Phi.$$

On the right-hand-side of the equations of motion are the forces acting on the vehicle. These include gravitational forces and moments due to the vehicle's weight W , buoyancy B , and location of the center of buoyancy (x_b, y_b) . The forces and moments due to the thrusters are given by R_x , R_y , and R_Φ . The hydrodynamic drag forces in (7.3) and (7.4) are given by H_x and H_y . Expressions for these are described in the next paragraph. The hydrodynamic drag moment in (7.5) is assumed to be proportional to the square of the angular velocity. The proportionality constant $C_{d\Phi}$ can be estimated from experimental data or approximated using strip theory [48]. The remaining forces in the equations of

motion, T_x , T_y , S_x , and S_y , are the forces associated with the tension and bending of the tether. They are defined by the following expressions:

$$\begin{aligned} T_x &= T[\cos \phi_o \cos \Phi + \sin \phi_o \sin \Phi] \\ T_y &= T[\sin \phi_o \cos \Phi - \cos \phi_o \sin \Phi] \\ S_x &= -EI \frac{\partial^2 \phi_o}{\partial s^2} [\cos \phi_o \sin \Phi - \sin \phi_o \cos \Phi] \\ S_y &= -EI \frac{\partial^2 \phi_o}{\partial s^2} [\cos \phi_o \cos \Phi + \sin \phi_o \sin \Phi] \end{aligned} \quad (7.7)$$

The variable ϕ_o denotes the value of the tether angle at the connection point between the tether and the vehicle. These forces produce moments whenever the tether connection point (x_c, y_c) is located away from the center of gravity.

The dependence of drag on the relative orientation of the vehicle to the flow can differ greatly, depending on the characteristic shape of the vehicle. The hydrodynamics involved can become quite complicated and are beyond the scope of this study. Often the angular dependence of drag, for a particular vehicle, is determined experimentally and the calculated drag coefficients are used in a *look-up table* within the simulation routine [28]. Here we adopt two alternative empirical relations for obtaining rough estimates of the hydrodynamic forces H_x and H_y . These models are based on experimental data collected at the MIT Ocean Engineering Testing Facility [24]. The first model is used for *bluff-shaped* bodies, where separation effects are important. It is given by:

$$\begin{aligned} H_x &= -\frac{1}{2} \rho A_p U_r \\ H_y &= -\frac{1}{2} \rho A_p V_r \end{aligned} \quad (7.8)$$

where A_p is the projected area and is equal to:

$$A_p = C_{dx} A_x |U_r| + C_{dy} A_y |V_r| \quad (7.9)$$

where C_{dx} and C_{dy} are the drag coefficients in the vehicle's x and y -directions, respectively.

A_x and A_y are the cross-sectional areas of the vehicle with outward normals parallel to the x and y -axes of the vehicle. The relative velocities U_r and V_r are defined in (7.6).

For simulations involving a *streamlined* body, it is more precise to use the following model for the hydrodynamic drag.

$$\begin{aligned} H_x &= -\frac{1}{2}\rho A_x C_{dx} U_r |U_r| \\ H_y &= -\frac{1}{2}\rho A_y C_{dy} V_r |V_r| \end{aligned} \quad (7.10)$$

Coupling Relations and Boundary Conditions

We require that the velocity of the tether at its endpoint, defined as (u_o, v_o) , be equal to the velocity of the vehicle at the connection point (x_c, y_c) . This gives the following pair of expressions:

$$\begin{aligned} u_o &= [\cos \Phi \cos \phi_o + \sin \Phi \sin \phi_o] U_c + [\cos \Phi \sin \phi_o - \sin \Phi \cos \phi_o] V_c \\ v_o &= [\sin \Phi \cos \phi_o - \cos \Phi \sin \phi_o] U_c + [\sin \Phi \sin \phi_o + \cos \Phi \cos \phi_o] V_c \end{aligned} \quad (7.11)$$

where the vehicle velocities at (x_c, y_c) are:

$$\begin{aligned} U_c &= U - \frac{\partial \Phi}{\partial t} y_c \\ V_c &= V + \frac{\partial \Phi}{\partial t} x_c \end{aligned}$$

The tether is assumed to be connected to both the ROV and the operator platform by pinned joints. Therefore, there are no moments at either end. If we define the ROV connection point to be located at $s = 0$ on the tether and the point where the tether meets the operator platform at $s = L$ (where L is the tether length), then we can write the following boundary conditions:

$$\frac{\partial \phi}{\partial s} = 0 \quad \text{at } s = 0, L \quad (7.12)$$

In addition, the tether velocities at $s = L$ must be prescribed.

7.2.2 Numerical Results

In this section we present the results of two simulations involving different vehicle maneuvers. In both simulations, the vehicle and tether are neutrally buoyant. For the vehicle, we also assume that its center of buoyancy coincides with its center of gravity. Thus, the gravitational terms in the equations of motion for the tether and vehicle are set equal to zero. We assume that the tether attaches to the ROV at the vehicle's center of gravity, and there is no moment due to the thrusters. This allows us to replace (7.5) with the solution $\Phi = \text{constant}$. The end of the tether that attaches to the operator is assumed to be stationary.

For each maneuver, a different vehicle was used (see table 7.1). The first simulation uses a vehicle with a bluff-shaped body and incorporates the hydrodynamic model described by (7.8)-(7.9). The second simulation involves a streamlined vehicle and, thus, incorporates the alternate drag model given by (7.10).

	Vehicle No. 1	Vehicle No. 2
Mass	360 kg	360 kg
C_{Dx}	1.0	0.2
C_{Dy}	1.0	1.4
A_x	0.6 m^2	0.2 m^2
A_y	0.6 m^2	1.2 m^2

Table 7.1: Characteristics of vehicle.

The characteristics of the tether used in the simulations are presented in table 7.2.

Length	100. m
Diameter	0.0114 m
C_t	0.015
C_n	2.0
E	200. GPa

Table 7.2: Characteristics of tether.

The tether and vehicle equations are approximated using a second-order, centered finite-difference scheme [1]. The coupled system of equations is solved iteratively using the

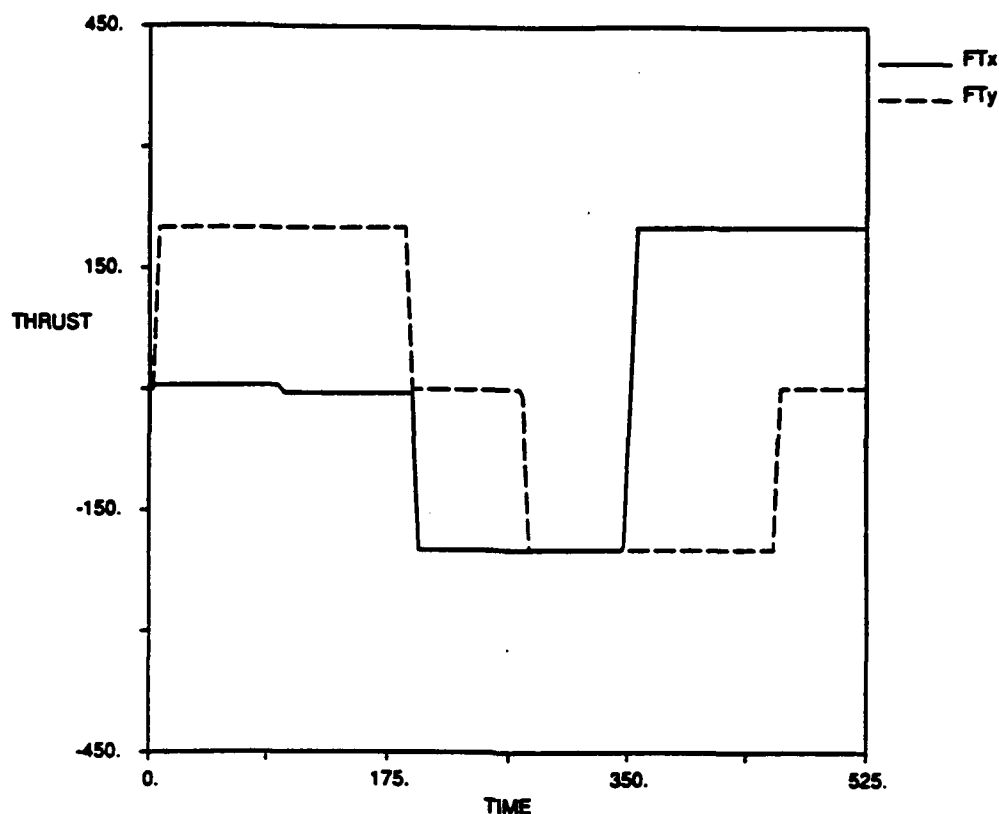


Figure 7.3: Applied thruster forces for simulation involving bluff-shaped body.

Newton-Raphson technique [55]. Further details on the simulation technique are supplied by Moxnes [46].

For both simulations, the tether was approximated with 100 nodes, and a time step of 0.025 seconds was used. This provided results in roughly three times real time on a SiliconGraphics IRIS 4D. The sizes of the time step and node spacing are conservative and were chosen to obtain smooth graphical renditions.

The first simulation consisted of applying the thrusters in such a way as to maneuver a bluff-body vehicle in an orbit about the operator platform. There is no current present so the hydrodynamic forces arise strictly from the motion of the tether and vehicle. The prescribed thrust is shown by the time records in figure 7.3.

The results of the simulation are given in figure 7.4. The initial position of the tether is given by the dashed line and marked by $t = 0$ s. As the simulation proceeds, a considerable amount of curvature develops in the tether due to the hydrodynamic drag. If we examine

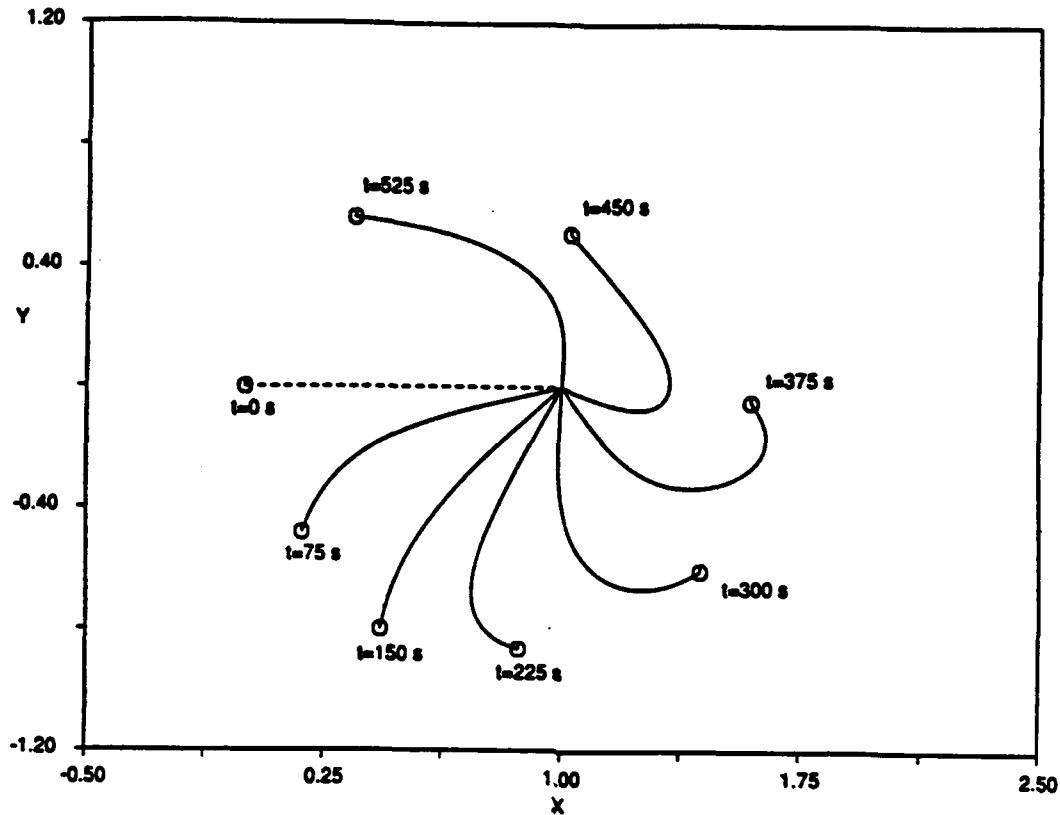


Figure 7.4: Numerical results: Displacement of vehicle and tether for applied loads given in figure 7.3.

the tension at the two end points of the tether and at the midpoint (at $s = 0, 50, 100$ meters), we see that the tension varies rapidly and at times approaches zero (figure 7.5. The steep changes in tension are a characteristic of low-tension systems, as demonstrated in previous chapters. The sudden decrease in tension followed by the gradual stiffening is a function of the thruster action and the shape of the tether. It is within the low-tension regions, that bending stiffness is required for numerical stability and physical accuracy.

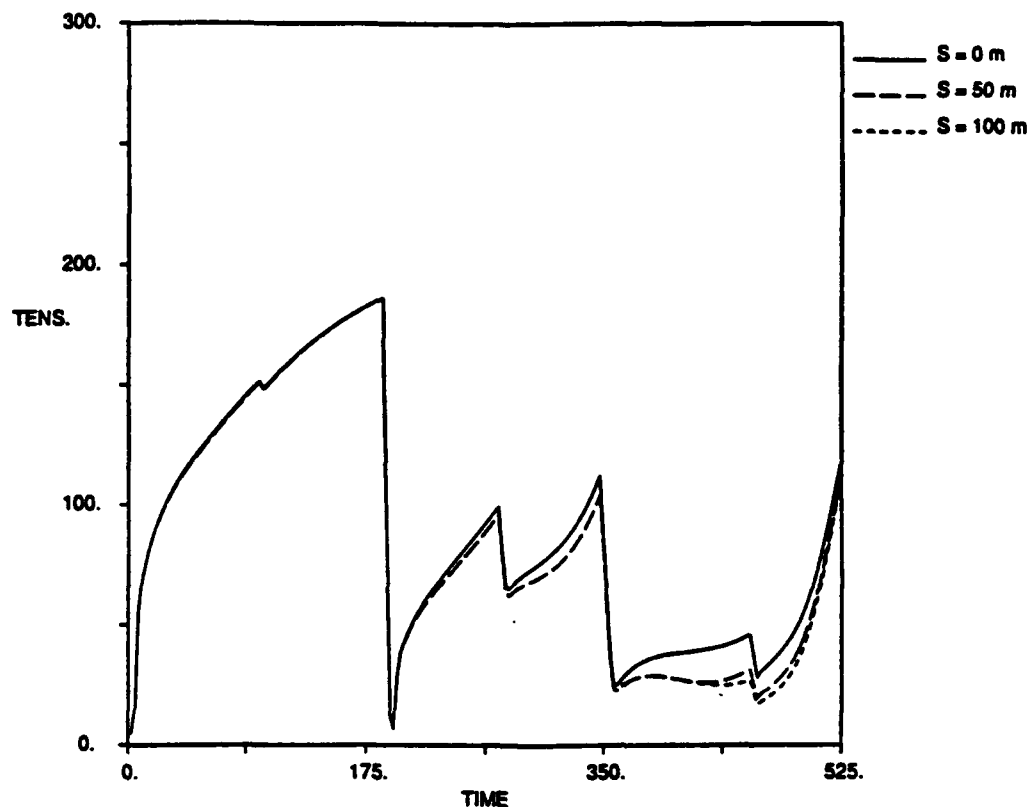


Figure 7.5: Numerical results: Tension at three locations along tether for applied loads given in figure 7.3.

The second simulation involves a streamlined vehicle system directed into a 1 knot current. Initially, the tether is parallel to the current and pulled taut by a constant in-line thrust. Side thrust was then applied as shown in Figure 7.6. The tether configuration is shown in figure 7.7, with $t = 0$ s denoting the initial condition. As readily seen (figure 7.8), the tether tension does not change appreciably during the simulation and as a result only a small degree of curvature develops in the tether. The reason is that for streamlined bodies, the in-line and transverse drag forces are effectively decoupled. Therefore, because the vehicle's heading is maintained, the in-line drag forces and tension remain roughly constant. This simulation shows that the same principles used to model low-tension systems are applicable over a wide range of tension magnitudes.

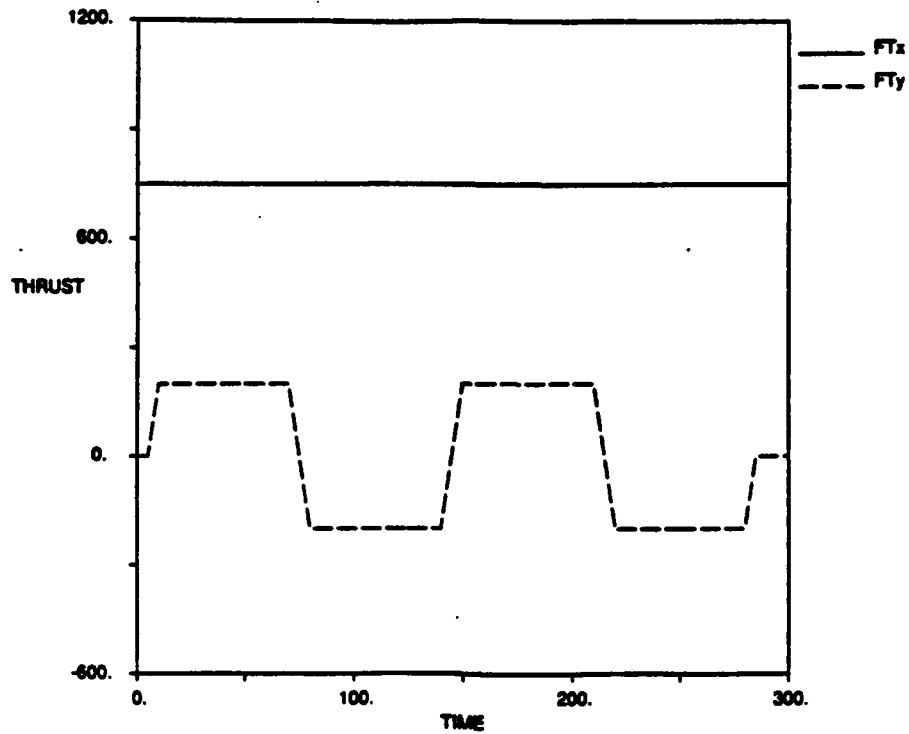


Figure 7.6: Applied thruster forces for simulation involving streamlined body.

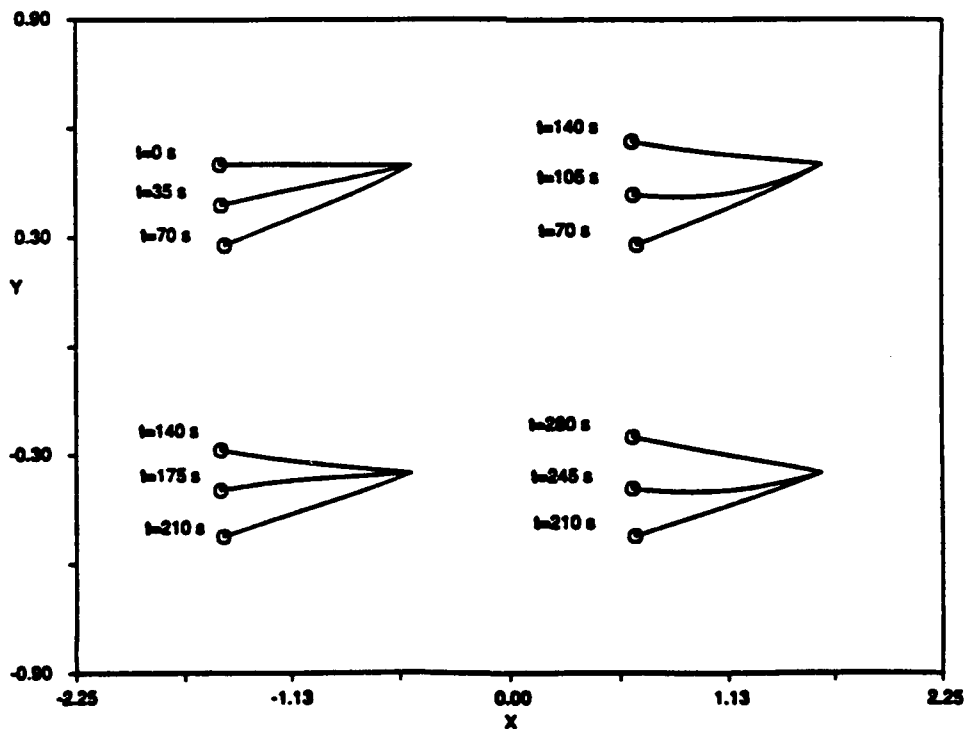


Figure 7.7: Numerical results: Displacement of vehicle and tether for applied loads given in figure 7.6.

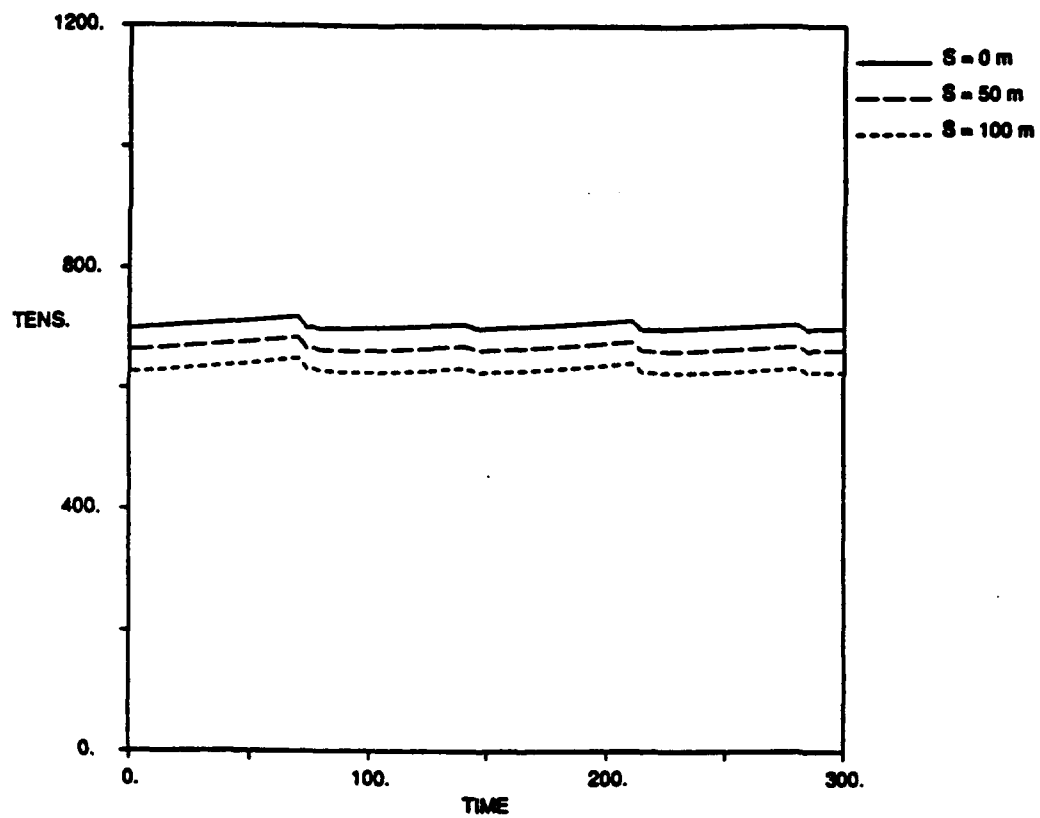


Figure 7.8: Numerical results: Tension at three locations along tether for applied loads given in figure 7.6.

Chapter 8

Conclusions and Recommendations

Herein we have formulated the three-dimensional nonlinear equations of motion for a submerged cable. The derivation of the equations can be viewed as a general formulation in that all forces and moments are equated for a incremental cable segment. In the final form of the equations, the effects of rotational inertia and torsion are neglected, under the assumption that the contribution of these forces is small compared to other affects. However, the cable bending stiffness must be retained in situations in which the cable tension approaches zero, as the cable equations are singular for zero tension if flexural stiffness is neglected. From a physical standpoint, bending stiffness provides the necessary mechanism by which energy is transferred across a point of zero tension.

The numerical techniques presented have been shown to provide an effective means for analyzing the nonlinear dynamics of low-tension cables and chains. Accuracy of the algorithms has been demonstrated through comparisons with known analytic solutions, as well as experimental data. Of particular note is the capability of modeling the highly nonlinear behavior of a collapsing chain.

The mechanisms for building tension and velocities were investigated for low-tension cables by considering the limiting case of a cable, initially at rest with zero tension, subjected to an impulsive load at one end. It was shown that the impulse equations accurately describe

the initial development of tension and velocity. It was found that the impulsive tension distribution depends entirely on the local curvature of the cable, and is independent of the geometric torsion. In addition, the tangential and normal velocities, expressed in terms of the principle coordinate directions, also depend exclusively on the curvature, while the binormal velocity remains constant.

Large rotational velocities were found to develop near regions of sharp transitions in curvature. In cases where the curvature is discontinuous, a physically impossible discontinuity occurs in the normal velocity. Introducing the cables bending stiffness ensures smooth behavior of the solution, however, boundary layers are found to develop. These boundary layers are sustained in time, demonstrating the intrinsic physical importance of the mechanism for low-tension cables.

The transition from high tension behavior to low tension behavior was investigated by considering the nonlinear dynamics of a hanging chain, driven harmonically at the top near resonance. Solutions were obtained using asymptotic, numerical, and experimental means. Asymptotic solutions predict that for a fixed excitation amplitude, frequency regions characterized by stable 2-D or 3-D response exist. In addition, a frequency region was identified within which all steady-state solutions were determined to be unstable. The width of this region was shown to increase monotonically with excitation level.

Numerical and experimental results were in close agreement with the asymptotic solutions for stable motions, with respect to both the nature and the amplitude of the response. Within the frequency range predicted by the asymptotic solution to provide unstable solutions, it was found that the response is characterized by irregular beating.

For further increasing excitation amplitudes, the chain was found to lose tension over a region near the free boundary for a short duration of time, after which the chain swings back and intersects itself. Collapse of the chain at moderate excitation amplitudes was also found to occur when the excitation frequency lies within the unstable frequency range and damping is removed after starting transients decay to zero. The chain's collapse can be also predicted by employing the asymptotic solution to determine the threshold response amplitude above which the oscillatory tension exceeds in amplitude the static tension.

Numerical and experimental results were found to be in good agreement up to the point

of collapse. By incorporating bending stiffness in the numerical model it was possible to simulate the chain response through the entire period of zero tension and subsequent collapse. Bending stiffness, although physically relevant only to wires, eliminates singularities in the cable equations, when the tension becomes zero, both in the governing equations and, especially, in the compatibility relations. When the value of the bending stiffness is properly selected (to be sufficiently small), it serves primarily to smooth out the configuration, hence ensuring stability of the solution, while affecting little the response.

Numerical results reveal large impulse-like tension peaks, characteristic of low tension cables, which cause steep gradients in velocity and angle. The transition from low to high tension regions is clearly demonstrated, with low tension effects being confined to the lower portion of the chain. Beyond the low tension region the response is regular and the chain behaves like a taut cable.

The impulse-like tension peaks exhibited in the hanging chain problem are characterized by a broad-band frequency content. As such, the possibility does exist for exciting elastic waves, providing sufficient energy exists near the fundamental frequency of elastic waves. However, because the chain eventually collapses for large amplitude motions, the energy content of the tension peaks is limited to a finite frequency region. Therefore, elastic waves only develop for moderately low values of elastic stiffness. In situations where elastic waves do develop, the waves are found to be stationary, resembling the linear solution for free-fixed end conditions.

Future work is required to more completely understand the effects of elasticity. This is an important topic considering the highly elastic character of synthetic cables. In particular, the complicated interaction between transverse and elastic modes is not well understood. The numerical techniques described herein could prove very useful for further investigation of elastic behavior.

Bibliography

- [1] C.M. Ablow and S. Schechter. Numerical simulation of undersea cable dynamics. *Ocean Engng.*, 10(6):443-457, 1983.
- [2] M. Abramowitz and I. Stegun. *Handbook of Mathematical Functions*. Dover Publications, 1970.
- [3] D.A. Barrie and M. Le May. Development of a real time roV simulator. In *Proceedings ROV '87 Conference*, San Diego, 1987.
- [4] C.M. Bender and S.A. Orszag. *Advanced Mathematical Methods for Scientists and Engineers*. McGraw-Hill, 1978.
- [5] P. Berge, Y. Pomeau, and C. Vidal. *Order Within Chaos: Towards a Deterministic Approach to Turbulence*. John Wiley and Sons, 1984.
- [6] A. Blik. *Dynamic Analysis of Single Span Cables*. PhD thesis, Massachusetts Institute of Technology, Cambridge, Massachusetts, 1984.
- [7] J.J. Burgess. *Natural Modes and Impulsive Motions of a Horizontal Shallow Sag Cable*. PhD thesis, Massachusetts Institute of Technology, Cambridge, Massachusetts, 1985.
- [8] J.J. Burgess. Modeling of undersea cable installation with a finite difference method. *First International of Offshore and Polar Engng Conference*, 2:222-227, 1991.
- [9] J.J. Burgess and M.S. Triantafyllou. The elastic frequencies of cables. *Journal of Sound and Vibration*, 120(1):153-165, 1988.

- [10] G.F. Carrier and C.E. Pearson. *Partial Differential Equations: Theory and Technique*. Academic Press, 1988.
- [11] M.J. Casarella and M. Parsons. A survey of investigations on the configuration and motion of cable systems under hydrodynamic loading. *Marine Technology Society Journal*, 4(4):27-44, 1970.
- [12] R. Chiou. *Nonlinear Hydrodynamic Response of Curved Singly-Connected Cables*. PhD thesis, Oregon State University, Corvallis, Oregon, 1989.
- [13] Y. Choo and M.J. Casarella. A survey of analytical methods for dynamic simulation of cable-body systems. *Journal of Hydronautics*, 7(4):137-144, 1973.
- [14] G. Dahlquist and A. Bjorck. *Numerical Methods*. Prentice-Hall, 1974.
- [15] T.N. Delmer, T.C. Stephens, and J.M. Coe. Numerical simulation of towed cables. *Ocean Engineering*, 10(2):119-132, 1983.
- [16] T.N. Delmer, T.C. Stephens, and J.A. Tremills. Numerical simulation of cable-towed acoustic arrays. *Ocean Engineering*, 15(6):511-548, 1988.
- [17] A.P. Dowling. The dynamics of towed flexible cylinders: Part 1. Neutrally buoyant elements. *Journal of Fluid Mechanics*, 187:507-532, 1988.
- [18] J.E. Goeller and P.A. Laura. Analytic and experimental study of the dynamic response of cable systems. *Offshore Technology Conference*, OTC 1156, 1970.
- [19] T.R. Goodman and J.P. Breslin. Statics and dynamics of anchoring cables in waves. *Journal of Hydronautics*, 10(4):113-120, 1976.
- [20] P. Hagedorn and B. Schafer. On non-linear free vibrations of an elastic cable. *International Journal of Non-Linear Mechanics*, 15:333-340, 1980.
- [21] F.B. Hildebrand. *Advanced Calculus for Applications*. Prentice-Hall, Inc., second edition, 1976.
- [22] C.T. Howell. Numerical analysis of 2-D nonlinear cable equations with applications to low tension problems. *International Journal of Offshore and Polar Engng.*, 2(2), 1992.

- [23] C.T. Howell. Investigation of large amplitude nonlinear dynamics of hanging chains. *Second International of Offshore and Polar Engng Conference*, 2, 1992 (In Press).
- [24] C.T. Howell, S. Moxnes, J. Anderson, M.A. Grosenbaugh, and M.S. Triantafyllou. Maneuvering underwater vehicles employing low-tension tethers. *Second International of Offshore and Polar Engng Conference*, 2, 1992 (In Press).
- [25] H.M. Irvine. *Cable Structures*. MIT Press, 1981.
- [26] H.M. Irvine and T.K. Caughey. The linear theory of free vibrations of a suspended cable. *Proceedings of the Royal Society of London*, A341:299-315, 1974.
- [27] D.W. Jordan and P. Smith. *Nonlinear Ordinary Differential Equations*. Clarendon Press, 1987.
- [28] S. Kalske and K. Happonen. Motion simulation of subsea vehicles. *First International of Offshore and Polar Engng Conference*, 2:74-84, 1991.
- [29] J.W. Kamman and R.L. Huston. Modeling of submerged cable dynamics. *Computers and Structures*, 20(1-3):623-629, 1985.
- [30] R.M. Kennedy. Transverse motion response of a cable-towed system: Part 1. Theory. *US Journal of Underwater Acoustics*, 30:97-108, 1980.
- [31] R.M. Kennedy and E.S. Strahan. A linear theory of transverse cable dynamics at low frequency. *Naval Underwater Systems Center (NUSC) Technical Report*, Rep. 6463, 1981.
- [32] J.J. Ketchmen and Y.K. Lou. Application of the finite element method to towed cable dynamics. *Proceedings Oceans 75 Conference*, 1:98-107, 1975.
- [33] P. Kohler, W. Maag, and R. Wehrli. Dynamics of a system of two satellites connected by a deployable and extensible tether of finite mass. *Analytic and Computational Mathematics*, 1, 1978.
- [34] H. Lamb. *Dynamics*. Cambridge University Press, 1914.

- [35] L.D. Landau and E.M. Lifshitz. *Theory of Elasticity*. Pergamon Press, 1959.
- [36] J.W. Leonard. Nonlinear dynamics of cables with low initial tension. *Journal of Engineering Mechanics (ASCE)*, 98(2):293-309, 1972.
- [37] J.W. Leonard and J.H. Nath. Comparison of finite element and lumped parameter methods for oceanic cables. *Engineering Structures*, 3:153-166, 1981.
- [38] D.J. Lewis, J.M. Lipscombe, and P.G. Thomasson. The simulation of remotely operated vehicles. In *Proceedings ROV '84 Conference*, San Diego, 1984.
- [39] M.J. Lighthill. Note on the swimming of slender fish. *Journal of Fluid Mechanics*, 9:305-317, 1960.
- [40] A. E. H. Love. *A Treatise on the Mathematical Theory of Elasticity*. Dover Publications, 1927.
- [41] J.J. McCoy. Effects of bending stiffness in tow and salvage cables. *Journal of Hydro-nautics*, 6(2):77-82, 1972.
- [42] J. Miles. Resonant, nonplaner motion of a stretched string. *Journal of Acoustical Society of America*, 75(5):1505-1510, 1984.
- [43] J.H. Milgram, M.S. Triantafyllou, F. Frimm, and G. Anagnostou. Seekeeping and extreme tensions in offshore towing. *Transactions of the Society of Naval Architects and Marine Engineers*, 96:35-72, 1988.
- [44] F. Milinazzo, M. Wilkie, and S.A. Latchman. An efficient algorithm for simulating the dynamics of towed cable systems. *Ocean Engineering*, 14(6):513-526, 1987.
- [45] A.R. Mitchell and D.F. Griffiths. *The Finite Difference Method in Partial Differential Equations*. John Wiley and Sons, 1980.
- [46] S. Moxnes. Development of a simulation model for underwater vehicles tethered by low-tension cables. Master's thesis, Massachusetts Institute of Technology, Cambridge, Massachusetts, 1991..

- [47] A.H. Nayfeh. *Nonlinear Oscillations*. John Wiley and Sons, 1979.
- [48] J.N. Newman. *Marine Hydrodynamics*. MIT Press, 1977.
- [49] C.R. Ortloff and J. Ives. On the dynamic motion of a thin flexible cylinder in a viscous stream. *Journal of Fluid Mechanics*, 38:713-720, 1969.
- [50] M.P. Paidoussis. Dynamics of flexible slender cylinders in axial flow: Part 1. Theory. *Journal of Fluid Mechanics*, 26(4):717-736, 1966.
- [51] M.P. Paidoussis. Stability of towed, totally submerged flexible cylinders. *Journal of Fluid Mechanics*, 34(2):273-297, 1968.
- [52] M.P. Paidoussis. Dynamics of cylindrical structures subjected to axial flow. *Journal of Sound and Vibration*, 29(3):365-385, 1973.
- [53] V. Papazoglou, S. Mavrakos, and S. Triantafyllou. Scaling and model testing of cables in water. *Journal of Sound and Vibration*, 140(1):103-115, 1990.
- [54] N.C. Perkins. Planar and non-planar response of a suspended cable driven by small support oscillations. *First International of Offshore and Polar Engng Conference*, 2:210-215, 1991.
- [55] W.H. Press, B.P. Flannery, S.A. Teukolsky, and W.T. Vetterling. *Numerical Recipes*. Cambridge University Press, 1988.
- [56] S.S. Rao. *Mechanical Vibrations*. Addison Wesley, 1986.
- [57] G. Rega, F. Vestroni, and F. Benedettini. Parametric analysis of large amplitude free vibrations of a suspended cable. *Journal of Solids and Structures*, 20(2):95-105, 1984.
- [58] J.H. Rhors. *Trans. Camb. Phil. Soc.*, 9:379-398, 1851.
- [59] E.J. Routh. *The Advanced Part of a Treatise on the Dynamics of a System of Rigid Bodies*. Dover Publications, sixth edition, 1955.
- [60] J.V. Sanders. A three-dimensional dynamic analysis of a towed system. *Ocean Engineering*, 9(5):483-499, 1982.

- [61] T. Sarpkaya and M. Isaacson. *Mechanics of Wave Forces on Offshore Structures*. Van Nostrand Reinhold, 1981.
- [62] J.W. Schram and S.P. Reyle. A three-dimensional dynamic analysis of a towed cable. *Journal of Hydraulics*, 2(4):213-220, 1968.
- [63] H. Shin. *Nonlinear Cable Dynamics*. PhD thesis, Massachusetts Institute of Technology, Cambridge, Massachusetts, 1987.
- [64] H. Shin. Analysis of extreme tensions in a snapping cable. *First International of Offshore and Polar Engng Conference*, 2:216-221, 1991.
- [65] C.P. Sparks. The influence of tension pressure and weight on pipe and riser deformations and stresses. *Journal of Energy Resources Technology*, 106:46-54, 1984.
- [66] S. Timoshenko. *Theory of Elasticity*. McGraw-Hill, 1934.
- [67] M.S. Triantafyllou. The dynamics of taut inclined cables. *Quarterly Journal of Mechanics and Applied Mathematics*, 37(3):421-440, 1984.
- [68] M.S. Triantafyllou. Dynamics of cables, towing cables, and mooring systems. *The Shock and Vibration Digest*, 23(7):3-8, 1991.
- [69] M.S. Triantafyllou and Grinfogel. Natural frequencies and modes of inclined cables. *Journal of Structural Engineering*, 112(1):139-148, 1986.
- [70] M.S. Triantafyllou and F.S. Hover. Cable dynamics of tethered underwater vehicles. *MIT Sea Grant College Program*, Report 90-4, 1990.
- [71] M.S. Triantafyllou and C.T. Howell. Nonlinear impulsive motions of low tension cables. *Journal of Engineering Mechanics (ASCE)*, 118(4):807-830, 1992.
- [72] M.S. Triantafyllou and C.T. Howell. Stable and unstable nonlinear response of hanging chains: Theory and experiment. *Proceedings of the Royal Society of London*, Submitted, 1992.
- [73] M.S. Triantafyllou and C.T. Howell. Nonlinear unstable response of hanging chains. *Journal of Sound and Vibration*, 160(1), 1993 (In press).

- [74] M.S. Triantafyllou and G.S. Triantafyllou. The paradox of the hanging string: An explanation using singular perturbations. *The Journal of Sound and Vibration*, 148(2):343-351, 1991.
- [75] W. Tsai, K.P. Yue, and M.K. Yip. Resonantly excited regular and chaotic motions in a rectangular wave tank. *Journal of Fluid Mechanics*, 216:343-380, 1990.
- [76] A. Watzky. Non-linear three-dimensional large-amplitude damped free vibration of a stiff elastic stretched string. *Journal of Sound and Vibration*, 153(1):125-142, 1992.
- [77] R.L. Webster. Nonlinear static and dynamic response of underwater cable structures using the finite element method. *Offshore Technology Conference*, OTC 2332, 1975.

DOCUMENT LIBRARY

March 11, 1991

Distribution List for Technical Report Exchange

Attn: Stella Sanchez-Wade
Documents Section
Scripps Institution of Oceanography
Library, Mail Code C-075C
La Jolla, CA 92093

Hancock Library of Biology &
Oceanography
Alan Hancock Laboratory
University of Southern California
University Park
Los Angeles, CA 90089-0371

Gifts & Exchanges
Library
Bedford Institute of Oceanography
P.O. Box 1006
Dartmouth, NS, B2Y 4A2, CANADA

Office of the International
Ice Patrol
c/o Coast Guard R & D Center
Avery Point
Groton, CT 06340

NOAA/EDIS Miami Library Center
4301 Rickenbacker Causeway
Miami, FL 33149

Library
Skidaway Institute of Oceanography
P.O. Box 13687
Savannah, GA 31416

Institute of Geophysics
University of Hawaii
Library Room 252
2525 Correa Road
Honolulu, HI 96822

Marine Resources Information Center
Building E38-320
MIT
Cambridge, MA 02139

Library
Lamont-Doherty Geological
Observatory
Columbia University
Palisades, NY 10964

Library
Serials Department
Oregon State University
Corvallis, OR 97331

Pell Marine Science Library
University of Rhode Island
Narragansett Bay Campus
Narragansett, RI 02882

Working Collection
Texas A&M University
Dept. of Oceanography
College Station, TX 77843

Library
Virginia Institute of Marine Science
Gloucester Point, VA 23062

Fisheries-Oceanography Library
151 Oceanography Teaching Bldg.
University of Washington
Seattle, WA 98195

Library
R.S.M.A.S.
University of Miami
4600 Rickenbacker Causeway
Miami, FL 33149

Maury Oceanographic Library
Naval Oceanographic Office
Stennis Space Center
NSTL, MS 39522-5001

Marine Sciences Collection
Mayaguez Campus Library
University of Puerto Rico
Mayaguez, Puerto Rico 00708

Library
Institute of Oceanographic Sciences
Deacon Laboratory
Wormley, Godalming
Surrey GU8 5UB
UNITED KINGDOM

The Librarian
CSIRO Marine Laboratories
G.P.O. Box 1538
Hobart, Tasmania
AUSTRALIA 7001

Library
Proudman Oceanographic Laboratory
Bidston Observatory
Birkenhead
Merseyside L43 7 RA
UNITED KINGDOM

REPORT DOCUMENTATION PAGE	1. REPORT NO. WHOI-92-30	2.	3. Recipient's Accession No.
4. Title and Subtitle Investigation of the Dynamics of Low-Tension Cables			5. Report Date June 1992
			6.
7. Author(s) Christopher Todd Howell			8. Performing Organization Rept. No. WHOI 92-30
9. Performing Organization Name and Address The Woods Hole Oceanographic Institution Woods Hole, Massachusetts 02543			10. Project/Task/Work Unit No.
			11. Contract(C) or Grant(G) No. (C) (G)
12. Sponsoring Organization Name and Address Funding was provided by the Office of Naval Research through the Massachusetts Institute of Technology			13. Type of Report & Period Covered Ph.D. Thesis
			14.
15. Supplementary Notes This thesis should be cited as: Christopher Todd Howell, 1992. Investigation of the Dynamics of Low-Tension Cables. Ph.D. Thesis. MIT/WHOI, WHOI-92-30.			
16. Abstract (Limit: 200 words) Low-tension cable problems are particularly complex as linear solutions are unobtainable in most cases, due to the lack of a meaningful static configuration. By contrast, the dynamics of taut cables are only weakly nonlinear. First, the three-dimensional nonlinear equations of motion and compatibility relations are formulated for a cable with bending stiffness. Forces in bending are included to provide the necessary physical mechanism for energy transfer across isolated points of zero tension and to ensure a smooth cable configuration. The mechanisms for low-tension response to excitation are explored by considering the limiting case of a cable with zero initial tension, subject to an impulsive force at one end. The three-dimensional equations show the development of impulsive tension. The intensity of the tension and the velocity components depend exclusively on the initial curvature and are independent of the geometric torsion. In addition, singularities are found to develop at points of curvature discontinuity. Incorporating the cable's bending stiffness removes these singularities by ensuring smooth curvature. However, sustained boundary layers are found to develop, demonstrating the importance of the underlying physical mechanism. The transition from taut to low-tension behavior is examined through an analysis of the dynamics of a hanging chain, driven by planar harmonic excitation at the top. For moderately large excitation amplitudes, asymptotic results demonstrate the existence of distinct regions of stable two-dimensional and stable three-dimensional response, as a function of frequency, as well as a distinct region in which all steady state solutions are found to be unstable. Numerical solutions of the fully nonlinear equations are in close agreement with the asymptotic results. Numerical results for even larger excitation amplitudes show that large impulse-like tension forces develop which cause the chain to lose tension over a region adjacent to its freely hanging end, and then collapse. The transition from low to high tension regions is clearly demonstrated, with low tension effects being confined to the lower portion of the chain. Experimental studies were conducted using a chain, 3/8 inches in diameter and 5.8 feet in length, which confirm qualitatively and quantitatively the theoretical and numerical predictions.			
17. Document Analysis a. Descriptors 1. low-tension 2. cables 3. bending stiffness b. Identifiers/Open-Ended Terms c. COSATI Field/Group			
18. Availability Statement Approved for publication; distribution unlimited.		19. Security Class (This Report) UNCLASSIFIED	21. No. of Pages 153
		20. Security Class (This Page)	22. Price